# Mathematical models for cell triggered tissue regeneration and wound formation

**Shimi Chettiparambil Mohanan**

Vom Fachbereich Mathematik der
Rheinland-Pfälzischen Technischen Universität
Kaiserslautern-Landau

zur Verleihung des akademischen Grades
Doktor der Naturwissenschaften (Doctor rerum naturalium, Dr. rer. nat.)
genehmigte Dissertation

**Gutachterinnen:**

Prof. Dr. Christina Surulescu, RPTU Kaiserslautern-Landau
Prof. Raluca Eftimie, Ph.D., Université de Franche-Comté, France

**Datum der Disputation:** 14. Februar 2025

RPTU Rheinland-Pfälzische Technische Universität Kaiserslautern Landau

**DE-386**

## Abstract

This thesis explores the mathematical modelling of tissue dynamics, focusing on processes such as tissue regeneration and degradation, influenced by cell migration and proliferation.

The first chapter examines meniscus cartilage regeneration. Utilising kinetic transport equations, we apply an upscaling technique to the lower-scale dynamics of stem cells and chondrocytes, deriving a macroscopic system of reaction-diffusion-(taxis) equations (RD(T)Es) coupled with an ordinary differential equation (ODE) for hyaluron. Analysis of pattern formation in a simplified version of this system highlights the critical role of the taxis coefficient. Numerical simulations complement this analysis, demonstrating pattern formation and system stability for varying taxis coefficient values.

The second chapter investigates wound formation and spread in Buruli ulcer, caused by bacteria named Mycobacterium ulcerans. Starting from kinetic transport equations (KTEs) and using parabolic scaling, we derive a macroscopic reaction-diffusion-taxis equation for bacteria, incorporating multiple taxis. An RDTE-RDE-ODE system is developed to model interactions among bacteria, the toxin mycolactone, normal tissue, and necrotic matter. We provide an analysis proving the existence of classical solution. Numerical simulations explore five scenarios with different taxis sensitivity parameters and initial conditions, revealing distinct dynamics for each solution component.

The final chapter incorporates microscopic-level bacterial dynamics through a random jump approach, resulting in a RDTE for bacteria. We analyse an RDTE-RDE-ODE system modelling bacteria, toxin, normal tissue, and necrotic matter, demonstrating solution existence in classical sense. Simulations offer deeper insights into the underlying biological processes. We conclude with a numerical simulation that highlights the differences in dynamics between the system derived from the random jump approach and the model based on kinetic transport equations.

In sum, this thesis contributes to developing and analysing multiscale mathematical models that enhance our understanding of tissue dynamics, with possible applications to tissue regeneration and wound formation.

# Zusammenfassung

Diese Dissertation untersucht die mathematische Modellierung von Gewebedynamiken, mit Fokus auf Prozesse wie Geweberegeneration und -abbau, beeinflusst durch Zellmigration und -proliferation.
Das erste Kapitel betrachtet die Regeneration von Meniskusknorpel. Unter Verwendung von Transportgleichungen wenden wir eine Upscaling-Technik auf die Dynamiken von Stammzellen und Chondrozyten auf niedrigerer Skala an und leiten ein makroskopisches System von Reaktions-Diffusions-(Taxis)-Gleichungen (RD(T)Gs) gekoppelt mit einer gewöhnlichen Differentialgleichung (ODE) für Hyaluron ab. Die Analyse der Musterbildung in einer vereinfachten Version dieses Systems hebt die entscheidende Rolle der taktischen Sensitivität hervor. Numerische Simulationen ergänzen diese Analyse, indem sie Musterbildung und Systemstabilität für verschiedene Werte des Taxis-Koeffizienten demonstrieren.
Das zweite Kapitel untersucht die Wundbildung und Ausbreitung im Kontext des Buruli-Ulkus, verursacht durch das Bakterium Mycobacterium ulcerans. Ausgehend von kinetischen Transportgleichungen (KTG) leiten wir mittels parabolischer Skalierung eine makroskopische RDT-Gleichung für Bakterien ab, die mehrfache Taxis berücksichtigt. Ein RDTG-RDG-ODE-System wird entwickelt, um die Wechselwirkungen zwischen Bakterien, dem Toxin Mykolakton, normalem Gewebe und nekrotischem Material zu modellieren. Die durchgeführte Analyse beweist die Existenz von Lösungen in klassischem Sinne. Numerische Simulationen untersuchen fünf Szenarien mit unterschiedlichen Taxis-Sensitivitätsparametern und Anfangsbedingungen und zeigen distinkte Dynamiken für jede Lösungskomponente.
Das letzte Kapitel integriert mikroskopische bakterielle Dynamiken durch einen Random-Jump-Ansatz, was zu einer Reaktions-Diffusions-Taxis-Gleichung für Bakterien führt. Wir analysieren ein RDTG-RDG-ODE-System, das Bakterien, Toxin, normales Gewebe und nekrotisches Material modelliert, und zeigen die Existenz von Lösungen in klassichem Sinne. Simulationen bieten tiefere Einblicke in die zugrundeliegenden biologischen Prozesse. Wir schließen mit einer numerischen Simulation, die die Unterschiede in der Dynamik beider makroskopischer Systeme (aus Kapitel 2 und aus Kapitel 3) aufzeigt.
Zusammenfassend trägt diese Dissertation zur Entwicklung und Analyse mehrskaliger mathematischer Modelle bei, die das Verständnis der Gewebedynamiken verbessern, mit möglichen Anwendungen auf Geweberegeneration und Wundbildung.

# Acknowledgement

First of all, I extend my deepest thanks to Prof. Dr. Christina Surulescu, who was a steadfast support throughout my entire PhD journey. Our many discussions—both mathematical and personal—were invaluable to my research and personal growth. Thank you so much for your trust in me.

I am thankful to the Deutscher Akademischer Austauschdienst (DAAD) for their financial support for my doctoral studies.

I would also like to thank Kirsten Höffler, who was always there as a pillar of support throughout my PhD. Thank you for helping me from the moment I arrived in Germany all the way to my thesis submission. I will always cherish our conversations. Thank you for being such a good listener, and for offering help, care, and empathy during my ups and downs.

I would like to express my sincere gratitude to you, Nishith and Maria, as well as to all my past group members and the members of Felix Klein, for your invaluable support. Jeremia, I am particularly thankful for your encouraging pep talks. Pawan, I am deeply appreciative of your unwavering support since the very beginning of my PhD journey.

I would like to thank my mother Shajeela, and my father Mohanan for the unwavering support. Thank you my friends Nachiket, Amalu, and Deepa, for being there for me and supporting me through this journey.

Last but not least, my wholehearted thanks go to my husband, Vineeth. Without you, this journey would not have been possible. You were always there to lift me up and motivate me. You encouraged me to pursue a PhD, knowing it was a dream of mine. Thank you for being my rock and my greatest support.

# Contents

# List of Figures

Chapter 1

# Introduction

Mathematical modelling has revolutionised biomedical research, offering a unique lens through which to investigate the complexities of human physiology and pathology. In the field of tissue regeneration, mathematical models play a crucial role in understanding the underlying mechanisms of tissue repair and guiding the development of regenerative therapies. Similarly, in the study of infectious diseases with wound formation, mathematical models provide insights into disease transmission, pathogenesis, and intervention strategies. In this work, we explore the use of mathematical modelling in two key areas: meniscus tissue regeneration and tissue degradation due to the pathogenesis of Buruli ulcer. We discuss the challenges and opportunities in modelling tissue regeneration and disease progression.

## 1.1 Biological Background

### 1.1.1 Tissue regeneration

Tissue regeneration is a field of significant importance, particularly in the context of the meniscus, an essential structure for leg movement. It is susceptible to injuries and cannot heal on its own in most cases. One of the most common knee injuries is a torn meniscus. Meniscal tears, similar to many other musculoskeletal diseases, mainly occur in sports-related activities (32%), and non-sports-related activities (38%) [27]. A torn meniscus causes pain, swelling and stiffness and sometimes a block to knee motion and trouble extending the knee fully. Usually icing and taking rest make the pain go away and give time for the torn to heal on its own. In severe cases, this may lead to surgery. Clinical studies indicate that partial and total meniscectomies lead to the prevalence of premature osteoarthritis in knee joints [31, 81].

Recent efforts have focused on meniscal regeneration using tissue-engineered scaffolds that mimic meniscus structure and composition. We address research which includes experiments with nonwoven scaffolds in a perfusion chamber, facilitating in vitro studies on chondrocytes and stem cells. Thereby, a scaffold containing stem cells and hyaluron is inserted into the meniscus. Such studies should help identifying key stimuli for cell prolif-

eration, migration, and differentiation. Our focus on the cellular mechanisms and scaffold interactions under varying environmental parameters can offer insights into effective tissue regeneration strategies.

### 1.1.2 Buruli ulcer wound formation

Buruli ulcer (BU) is caused by Mycobacterium ulcerans. This bacterium is a member of the family of bacteria causing tuberculosis and leprosy. It is a neglected tropical or subtropical disease [42] characterised by destructive skin lesions and tissue damage. Delay of treatment results require prolonged periods in the hospital [10] and long-term disability [2]. It often affects geographical regions with limited healthcare resources, posing significant challenges for diagnosis, treatment, and control while demonstrating higher incidence rates in children compared to adults [15].

The infection of M. ulcerans was first described in 1948 in Australia [1], but it took its name as BU in Uganda because the cases they described were first detected in Buruli city, near Lake Kyoga. Buruli Ulcer is the third most common illness after tuberculosis and leprosy, but it was ignored until 1998. After 1998, WHO started to address this disease and conduct research on tools to diagnose, treat and prevent BU [102]. All forms of Buruli ulcer respond to antibiotic treatment [34], but if the lesion is very large, it heals very slowly and needs surgery. When the untreated swellings evolve into necrotic skin ulcers with deeply undermined edges, scarring and contractual deformities are evoked, and in the end, bones can also be affected. Thus, amputations and severe disabilities can occur as a result.

Advanced stages of BU require surgery, however, the true extent of the lesions cannot be assessed by commonly available medical techniques and this often leads to post-surgery recurrences [71]. Therefore, mathematical models are called upon to help make predictions about the spread of bacteria and necrotic matter and hence guide the resection. To get a mathematical model, it is important to understand the structure and the pathogenesis of the illness in the organism. Observations have been made by investigating the pathogenesis of BU. Models are set up making use of these observations.

Mathematical modelling of the spread of M. ulcerans bacteria is not so much developed and so far there has been no reasonable space-time mathematical model. Ordinary differential equation (ODE) disease spread models have been studied [72, 104]. However, the spread of bacteria within the wound is crucial and has to be studied.

## 1.2 Mathematical modelling

This thesis focuses on modelling processes related to tissue regeneration and wound formation, where various cell types interact dynamically with their environment. We develop macroscopic systems coupling ODEs and reaction-diffusion-transport equations (RDTEs) in order to capture the cell and tissue behaviour. Existing literature offers a diverse range

of models for macroscopic systems (e.g., [17, 54]). Works such as [93, 94, 106, 107] analyse these models, emphasising the influence of heterogeneous tissue on cell behaviour.

Our approach utilises two different methods to develop models:

1. A multi-scale methodology, breaking down the problem into three levels:
   **Microscopic level:** This level focuses on the interactions between individual cells and their immediate environment.
   **Mesoscopic level:** This level addresses cell density distributions, considering independent variables like time, position, and velocity. Mesoscopic models employ kinetic transport equations(KTEs) to describe changes in cell densities due to cell reorientation. At the mesoscopic level, we include the tactic behaviour of cells along with growth terms.
   **Macroscopic level:** Through upscaling and moment closure procedures, we derive equations from the mesoscopic level via macroscopic reaction-diffusion-transport equations (RDTEs). Here we integrate influences such as taxis (including diffusion, chemotaxis, and haptotaxis), growth limitation due to cell overcrowding (volume filling), and source terms (proliferation, decay, and phenotypic switching).

2. Additionally, we employ a random jump approach to model cell movement for the Buruli ulcer problem. This method introduced in [91] and used in several different contexts [44, 45], see [46] for a review, converts the biological domain (tissue space) into a lattice, allowing us to simulate the ability of living organisms to respond to environmental cues. The jump direction is determined by stimuli at the current position and neighbouring points. Using transition probabilities and microscopic velocities, we derive a master equation, which is used to deduce macroscopic RDTEs.

### 1.2.1 Tissue regeneration

Existing mathematical models for tissue regeneration, such as those in [7, 13, 19, 20, 37, 40, 87], address biochemical or mechanical influences on cell populations. This thesis develops a novel multiscale model that incorporates the crucial role of chemical cues in cell movement. The employed multiscale approach has been applied in various models for tissue regeneration, particularly in the context of glioma invasion in brain tissue (e.g., [23, 25, 26, 32, 33, 55, 77, 105]).

### 1.2.2 Buruli ulcer wound formation

While ODE models showing the spread of Buruli ulcer among people have been used to study Buruli ulcer control at the population level (e.g., [30, 69, 72]), there is a lack of RDTE models that depict the disease's progression within an individual. This gap is addressed in this thesis. We present two novel RDTE models specifically designed to analyse the spread of Buruli ulcer inside the human body. In particular, we employ the multiscale modelling using transport equations and the random jump approach (as e.g. in [22, 78, 91]) to model the dynamics of cell movement within these models. These approaches allow us to accurately simulate the spatial spread of the ulcer and the interaction of cells

with the disease environment. These models provide valuable insights that complement existing population-level models for Buruli ulcer control.

## 1.3 Outline

Our thesis is comprised of the following chapters:

- Chapter 2 Multiscale model for tissue regeneration in meniscal scaffolds
  This chapter utilises a multiscale mathematical model to explore cell dynamics during meniscus regeneration. The model incorporates three scales: microscopic (focusing on transmembrane entity interactions with hyaluron in the extracellular space), mesoscopic (analysing cell density distributions based on time, position, and velocity), and macroscopic (considering overall stem cell and chondrocyte populations along with hyaluron concentration). A "toy model" is employed to study pattern formation through numerical simulations, revealing how a key parameter's critical value influences these patterns. This multiscale approach provides a comprehensive understanding of cell behaviour and its impact on regeneration, paving the way for future refinements with more realistic biological details and parameters.

- Chapter 3 Multiscale model for Buruli ulcer wound
  Using kinetic transport equations, this chapter presents a mathematical model based on the multiscale method. Based on mesoscale bacteria, we developed a macroscopic mathematical model for bacteria, mycolactone, normal tissue, and necrotic matter. The mathematical analysis of the model is presented in Section 3. This section prove the existence of a global classical solution. The results of the numerical simulation are included in section 4.

- Chapter 4 Mathematical modelling of Buruli ulcer wound using random jump approach
  A mathematical model based on random jumps of particles between the sites of a lattice is constructed. The mathematical analysis of the model can be found in Section 3, where we prove the existence of a global classical solution. The numerical simulation is discussed in Section 4.

- Conclusion
  We include a summary of all the results obtained along with outlook.

Chapter 2

# Multiscale model for tissue regeneration in meniscal scaffolds

## 2.1 Introduction

Regeneration of tissue is a vital process in all living organisms, essential to maintaining and restoring health. Researchers have been studying tissue regeneration for years, with the aim of enhancing medical treatments. As a result of the development of therapy methods that prioritise repairing and regenerating tissues over surgical removal [11, 43, 74, 82, 96, 103, 108], mathematical modelling has become increasingly important in understanding regeneration processes. It is now possible to investigate and predict the behaviour of interconnected systems with the help of mathematical models, which provide powerful tools for exploring the complex mechanisms of biological processes. In the context of tissue regeneration, such models can provide critical insights into processes like wound healing, bone and cartilage regeneration.

Various works have reviewed mathematical modelling of tissue regeneration, including [18, 100]. There is an increasing interest in meniscus tissue engineering, however, there is a lack of mathematical models that can effectively describe the dynamics of the processes involved. Essential aspects of these models include the degradation of engineered fibres, the migration, differentiation of stem cells and dedifferentiation of chondrocytes into stem cells within the scaffold, and the production of tissue by chondrocytes.

This chapter is based on the works [21, 41]. In [41] we developed a model showing the cell dynamics of stem cells, chondrocytes, hyaluron, ECM and differentiation medium. There we considered the fact that a variety of stimuli such as mechanical stress [4, 12, 35, 48, 49, 58, 70, 80, 85], scaffold topography [38] and chemical cues from the extracellular matrix [36, 63, 66] can influence the process of differentiation and dedifferentiation. Here, in section 2.2 a macroscopic model is developed that accounts for stem cells, chondrocytes, hyaluron dynamics from descriptions on a lower scale. The method follows closely that in [23–25]. In Section 2.3 a stability analysis of patterns and bifurcations is performed for a

simplified version of the PDE-ODE system obtained in Section 2.2. Section 2.4 shows 1D and 2D numerical simulations of the simplified model for various scenarios.

## 2.2 Mathematical modelling

In this section, we derive a new mathematical model for the major biological processes that characterise cell colonisation in a scaffold for meniscus regeneration. We use a multiscale model approach for modelling the meniscus tissue regeneration using the kinetic theory of active particles, see e.g. [16].

### 2.2.1 Microscopic level

We begin with the microscopic level of single cells and associated receptor binding dynamics. We consider the binding of stem cell receptors to the chemoattractant (hyaluron). This is done using an ODE for its mass action kinetics as in [51].

Let $y$ denote the amount of stem cell receptors occupied with hyaluron (of density $h$ and reference density $H$). Simple receptor binding kinetics then takes the form

$$(R_0 - y) + \frac{h}{H} \underset{k^-}{\overset{k^+}{\rightleftharpoons}} y,$$

where $R_0$ represents the total amount of bound receptors on a stem cell membrane; we assume $R_0$ to be constant. Then we obtain the following ODE from the above mass action kinetics:

$$\dot{y} = k^+ \frac{h}{H}(R_0 - y) - k^- y, \tag{2.2.1}$$

where $k^+$ and $k^-$ denote attachment and detachment rate of stem cell to hyaluron.

Rescaling $y/R_0 \rightsquigarrow y \in (0,1)$ further simplifies the notation. Since receptor binding is very fast compared to the overall dynamics of cell migration and proliferation, we assume it to quickly reach the equilibrium and only deal with the steady state of the above equation:

$$y^* = \frac{k^+ \frac{h}{H}}{k^+ \frac{h}{H} + k^-}.$$

We denote by $z := y^* - y$ the (very small) deviation of $y$ from $y^*$ and proceed as in [23–25, 32, 33] to obtain from (2.2.1)

$$\dot{z} = -zB(h) + \frac{k^-}{(B(h))^2} v \cdot \nabla_x B(h) := G(z,h),$$

with $B(h) := k^+ \frac{h}{H} + k^-$.

### 2.2.2 Mesoscopic level

On this level the dynamics of cell density distributions of stem cells and chondrocytes are described using kinetic transport equations(KTEs). Let the cell density function $p_1(t, x, v, z)$ represent the concentration of stem cells at time $t > 0$, located at position $x \in \mathbb{R}^n$, with velocity $v$ within $V_1 = s_1\mathbb{S}^{n-1}$, and exhibiting a deviation $z \in Z = (y^* - 1, y^*)$ from the equilibrium state of receptor binding. Likewise, $p_2(t, x, v)$ represents the density of chondrocytes with velocity $v \in V_2 = s_2\mathbb{S}^{n-1}$. The positive constants $s_1$ and $s_2$ denote the speeds of stem cells and chondrocytes, respectively. In the KTE describing the cell dynamics of stem cells, we also include proliferation, death term, differentiation of the stem cells into chondrocytes, and the dedifferentiation of chondrocytes into stem cells. The KTE is given as follows:

$$\begin{aligned}\partial_t p_1 + \nabla_x \cdot (v p_1) + \partial_z (G(z,h) p_1) =& \mathcal{L}_1[\lambda_1(z)]p_1 - \alpha_1 p_1 + \alpha_2 p_2 \\ &+ \beta p_1 (1 - \frac{c_1}{C_1^*} - \frac{c_2}{C_2^*}),\end{aligned}$$

where $C_j^*$ denotes the carrying capacity of the cell population $j$ $(j = 1, 2)$, $\beta > 0$ is the constant growth rate of stem cells, and $\alpha_1,\ \alpha_2 > 0$ are constants that represent the rates of differentiation of stem cells into chondrocytes and dedifferentiation of the latter, respectively. Here we assume that the cell source term is determined solely by macroscopic factors in the extracellular space, rather than by cell direction or scaffold fibre orientation. Moreover, $\mathcal{L}_1[\lambda_1]$ is the turning operator which characterises the reorientation of stem cells and is defined as:

$$\mathcal{L}_1[\lambda_1(z)]p_1(t, x, v, z) := -\lambda_1(z)p_1(t, x, v, z) + \lambda_1(z) \int_{V_1} K_1(x, v)p_1(t, x, v', z)dv', \quad (2.2.2)$$

with $\lambda_1(z) = \lambda_{10} - \lambda_{11} z \geqslant 0$ is the turning rate as in [23, 24, 32, 33], that depends on the microscopic variable $z$. We take $\lambda_{10}, \lambda_{11}$ as constants.

In the KTE describing the cell dynamics of chondrocytes, we consider the differentiation of stem cells into chondrocytes and the dedifferentiation of chondrocytes into stem cells and is given as follows

$$\partial_t p_2 + \nabla_x \cdot (v p_2) = \mathcal{L}_2[\lambda_2]p_2 + \alpha_1 p_1 - \alpha_2 p_2, \quad (2.2.3)$$

where the turning operator $\mathcal{L}_2[\lambda_2]$, with constant $\lambda_2 > 0$ is defined as

$$\mathcal{L}_2[\lambda_2]p_2(t, x, v) := -\lambda_2 p_2(t, x, v) + \lambda_2 \int_{V_2} K_2(x, v)p_2(t, x, v')dv'. \quad (2.2.4)$$

For the turning kernel we take into account (as in [23, 24, 32, 33, 77]) the anisotropy of the scaffold fibres and choose $K_j(x, v) := q(x, \hat{v})/\omega_j$ $(j = 1, 2)$, where $\hat{v} = \frac{v}{|v|}$ and $q(x, \theta)$ with $\theta \in \mathbb{S}^{n-1}$ is the orientational distribution of the scaffold fibres, normalised by $\omega_j = s_j^{n-1}$. Thus the turning operators in (2.2.2), (2.2.4) take the form

$$\mathcal{L}_j[\lambda_j]p_j := \lambda_j \left( \frac{q(x, \hat{v})}{\omega_j} \int_{V_j} p_j dv - p_j(v) \right) \qquad (j = 1, 2).$$

We denote by $c_1(t,x) := \iint_{V_1 \times Z} p_1(t,x,v,z)d(v,z)$ and $c_2(t,x) := \int_{V_2} p_2(t,x,v)dv$ the macroscopic densities of stem cells and chondrocytes, respectively.

We assume the tissue to be undirected, hence $q(x,\theta) = q(x,-\theta)$ for all $x$ in $\mathbb{R}^n$ and $\theta \in \mathbb{S}^{n-1}$. We introduce the notations

$$\mathbb{E}_q(x) = \int_{\mathbb{S}^{n-1}} \theta q(x,\theta)d\theta \qquad \text{(observe that for undirected tissue } \mathbb{E}_q = 0)$$
$$\mathbb{V}_q(x) = \int_{\mathbb{S}^{n-1}} (\theta - \mathbb{E}_q) \otimes (\theta - \mathbb{E}_q) q(x,\theta)d\theta.$$

Let us introduce the following moments of $p_1$ with respect to the 'activity' variable $z$ and velocity $v$:

$$m(t,x,v) := \int_Z p_1(t,x,v,z)dz, \quad m^z(t,x,v) := \int_Z z p_1(t,x,v,z)dz,$$
$$M^z(t,x) := \int_{V_1} m^z(t,x,v)dv.$$

Due to the fact that $z$ is very small, we will neglect moments of $p_1$ w.r.t. $z$ for higher orders. This will ensure the subsequent informal moment closure. The high dimensionality of this mesoscopic scale system would require expensive numerical simulations. Hence in the next section, a parabolic upscaling is done in order to obtain a macroscopic system.

### 2.2.3 Upscaling and macroscopic level

In this section we deduce a system of macroscopic equations by performing a parabolic scaling of the time and space variables: $t \rightsquigarrow \varepsilon^2 t$ and $x \rightsquigarrow \varepsilon x$ in the mesoscopic equations. An effective macroscopic system is also more conducive for assessing the relevant behaviour of stem cells and chondrocytes in interaction with hyaluron. Moreover, proliferation, growth, decay, differentiation of stem cells into chondrocytes, and dedifferentiation of chondrocytes occur over a significantly longer timescale compared to cell migration. Therefore we rescale these terms by a small factor $\varepsilon^2$. Applying this to (2.2.2), (2.2.3) leads to

$$\varepsilon^2 \partial_t p_1 + \varepsilon \nabla_x \cdot (v p_1) + \partial_z \left( \left( -zB(h) + \varepsilon \frac{k^-}{(B(h))^2} v \cdot \nabla_x B(h) \right) p_1 \right)$$
$$= \mathcal{L}_1[\lambda_1(z)]p_1 + \varepsilon^2 \left( -\alpha_1 p_1 + \alpha_2 p_2 + \beta p_1 (1 - \frac{c_1}{C_1^*} - \frac{c_2}{C_2^*}) \right) \quad (2.2.5)$$
$$\varepsilon^2 \partial_t p_2 + \varepsilon \nabla_x \cdot (v p_2) = \mathcal{L}_2[\lambda_2]p_2 + \varepsilon^2 \left( \alpha_1 p_1 - \alpha_2 p_2 \right). \quad (2.2.6)$$

We assume $p_1$ to be compactly supported in the phase space $\mathbb{R}^n \times V_1 \times Z$. Integrating (2.2.5) w.r.t. $z$ gives

$$\varepsilon^2 \partial_t m + \varepsilon \nabla_x \cdot (vm) = -\lambda_{10} \left( m - \frac{q}{\omega_1} c_1 \right) + \lambda_{11} \left( m^z - \frac{q}{\omega_1} M^z \right)$$
$$+ \varepsilon^2 \left( -\alpha_1 m + \alpha_2 p_2 + \beta m (1 - \frac{c_1}{C_1^*} - \frac{c_2}{C_2^*}) \right). \quad (2.2.7)$$

Now multiply (2.2.5) by $z$ and integrate w.r.t. $z$ to get

$$\varepsilon^2\partial_t m^z + \varepsilon\nabla_x\cdot(vm^z) + m^z B(h) - \varepsilon\frac{k^-}{(B(h))^2}v\cdot\nabla_x B(h)m = -\lambda_{10}\left(m^z - \frac{q}{\omega_1}M^z\right)$$
$$-\varepsilon^2\alpha_1 m^z + \varepsilon^2\alpha_2 p_2(y^* - \frac{1}{2}) + \varepsilon^2\beta m^z\left(1 - \frac{c_1}{C_1^*} - \frac{c_2}{C_2^*}\right). \qquad (2.2.8)$$

We perform Hilbert expansions of the $p_1$, $p_2$ and of $c_2$-moments :

$$m = \sum_{j=0}^{\infty}\varepsilon^j m_j, \qquad m^z = \sum_{j=0}^{\infty}\varepsilon^j m_j^z, \qquad c_1 = \sum_{j=0}^{\infty}\varepsilon^j c_{1j},$$
$$M^z = \sum_{j=0}^{\infty}\varepsilon^j M_j^z, \qquad p_2 = \sum_{j=0}^{\infty}\varepsilon^j p_{2j}, \qquad c_2 = \sum_{j=0}^{\infty}\varepsilon^j c_{2j}.$$

Equating powers of $\varepsilon$ in (2.2.6), (2.2.7), (2.2.8) we get

$\varepsilon^0$:

$$0 = \lambda_2(\frac{q}{\omega_2}c_{20} - p_{20}) \qquad (2.2.9)$$
$$0 = -\lambda_{10}\left(m_0 - \frac{q}{\omega_1}c_{10}\right) + \lambda_{11}\left(m_0^z - \frac{q}{\omega_1}M_0^z\right) \qquad (2.2.10)$$
$$m_0^z B(h) = -\lambda_{10}\left(m_0^z - \frac{q}{\omega_1}M_0^z\right) \qquad (2.2.11)$$

$\varepsilon^1$:

$$\nabla_x\cdot(vp_{20}) = \lambda_2\left(\frac{q}{\omega_2}c_{21} - p_{21}\right)$$
$$\nabla_x\cdot(vm_0) = -\lambda_{10}\left(m_1 - \frac{q}{\omega_1}c_{11}\right) + \lambda_{11}\left(m_1^z - \frac{q}{\omega_1}M_1^z\right) \qquad (2.2.12)$$
$$\nabla_x\cdot(vm_0^z) + m_1^z B(h) - \frac{k^-}{(B(h))^2}v\cdot\nabla_x B(h)m_0 = -\lambda_{10}\left(m_1^z - \frac{q}{\omega_1}M_1^z\right) \qquad (2.2.13)$$

$\varepsilon^2$ (from (2.2.6), (2.2.7)):

$$\partial_t p_{20} + \nabla_x\cdot(vp_{21}) = \lambda_2\left(\frac{q}{\omega_2}c_{22} - p_{22}\right) + \alpha_1 p_{10} - \alpha_2 p_{20}$$
$$\partial_t m_0 + \nabla_x\cdot(vm_1) = -\lambda_{10}\left(m_2 - \frac{q}{\omega_1}c_{12}\right) + \lambda_{11}\left(m_2^z - \frac{q}{\omega_1}M_2^z\right) - \alpha_1 m_0$$
$$+ \alpha_2 p_{20} + \beta m_0\left(1 - \frac{c_{10}}{C_1^*} - \frac{c_{20}}{C_2^*}\right).$$

Integrate (2.2.11) w.r.t. $v$ to obtain $M_0^z = 0$. Substitute this in (2.2.11) to follow $m_0^z = 0$. From (2.2.10) and (2.2.9) follows

$$m_0 = \frac{q}{\omega_1}c_{10}, \qquad p_{20} = \frac{q}{\omega_2}c_{20}. \qquad (2.2.14)$$

Integrating (2.2.13) w.r.t. $v$ and using $\mathbb{E}_q = 0$ leads to $M_1^z = 0$. Then from (2.2.13) we obtain

$$m_1^z = \frac{k^-}{B(h)^2(B(h)+\lambda_{10})} v \cdot \nabla_x B(h) \frac{q}{\omega_1} c_{10}. \tag{2.2.15}$$

Now apply the operator $\mathcal{L}_1[\lambda_{10}]$ to $m_1(t,x,v) = \int_Z p_{11}(t,x,v,z)dz$:

$$\begin{aligned}\mathcal{L}_1[\lambda_{10}]m_1 &= \lambda_{10}\left(\frac{q}{\omega_1}c_{11} - m_1\right)\\ &= \nabla_x \cdot (vm_0) - \lambda_{11} m_1^z \qquad \text{(due to (2.2.12))}.\end{aligned}$$

This is a compact Hilbert-Schmidt operator on the weighted space $L^2_{\frac{q}{\omega_1}}(V_1) := \{w \in L^2(V_1) \ : \ \int_{V_1} w^2 \frac{dv}{\frac{q}{\omega_1}} < \infty\}$ has kernel $\left\langle \frac{q}{\omega_1} \right\rangle := \text{span}(\frac{q}{\omega_1})$, thus its pseudo-inverse can be determined on $\left\langle \frac{q}{\omega_1} \right\rangle^\perp$. We obtain (for more details refer e.g., to [32, 75]):

$$m_1 = -\frac{1}{\lambda_{10}} \left(\nabla_x \cdot (vm_0) - \lambda_{11} m_1^z\right), \quad \text{thus} \quad c_{11} = 0. \tag{2.2.16}$$

Analogously,

$$p_{21} = -\frac{1}{\lambda_2} \left(\nabla_x \cdot (vp_{20})\right), \quad \text{thus} \quad c_{21} = 0. \tag{2.2.17}$$

Now integrate the $\varepsilon^2$-equations w.r.t. $v$ to obtain

$$\partial_t c_{10} + \nabla_x \cdot \int_{V_1} v m_1 \, dv = -\alpha_1 c_{10} + \alpha_2 \frac{\omega_1}{\omega_2} c_{20} + \beta c_{10}\left(1 - \frac{c_{10}}{C_1^*} - \frac{c_{20}}{C_2^*}\right) \tag{2.2.18}$$

$$\partial_t c_{20} + \nabla_x \cdot \int_{V_2} v p_{21} \, dv = \alpha_1 \frac{\omega_2}{\omega_1} c_{10} - \alpha_2 c_{20}. \tag{2.2.19}$$

In virtue of (2.2.16) we evaluate

$$\begin{aligned}\nabla_x \cdot \int_{V_1} v m_1 &= -\nabla\nabla : (\mathbb{D}_1 c_{10}) + \nabla \cdot \left(\frac{k^- \lambda_{11}}{B(h)^2(B(h)+\lambda_{10})} \mathbb{D}_1 \nabla B(h) c_{10}\right)\\ \nabla_x \cdot \int_{V_2} v p_{21} &= -\nabla\nabla : (\mathbb{D}_2 c_{20}),\end{aligned}$$

with

$$\mathbb{D}_1(x) = \frac{1}{\lambda_{10}} \int_{V_1} v \otimes v \frac{q(x,\hat{v})}{\omega_1} dv = \frac{s_1^2}{\lambda_{10}} \int_{\mathbb{S}^{n-1}} \theta \otimes \theta q(x,\theta), \tag{2.2.20}$$

$$\mathbb{D}_2(x) = \frac{1}{\lambda_2} \int_{V_2} v \otimes v \frac{q(x,\hat{v})}{\omega_2} dv = \frac{\lambda_{10}}{\lambda_2} \left(\frac{s_2}{s_1}\right)^2 \mathbb{D}_1(x). \tag{2.2.21}$$

Plugging these into (2.2.18), (2.2.19) and neglecting higher order terms in the Hilbert expansions of $c_1$ and $c_2$ (see also (2.2.16), (2.2.17)) we obtain the macroscopic RDTEs

$$\partial_t c_1 - \nabla\nabla : (\mathbb{D}_1 c_1) + \nabla \cdot \left( \frac{k^- \lambda_{11}}{B(h)^2 (B(h) + \lambda_{10})} \mathbb{D}_1 \nabla B(h) c_1 \right) = -\alpha_1 c_1 + \alpha_2 \frac{\omega_1}{\omega_2} c_2 + \beta c_1 \left( 1 - \frac{c_1}{C_1^*} - \frac{c_2}{C_2^*} \right) \tag{2.2.22}$$

$$\partial_t c_2 - \nabla\nabla : (\mathbb{D}_2 c_2) = \alpha_1 \frac{\omega_2}{\omega_1} c_1 - \alpha_2 c_2. \tag{2.2.23}$$

Thereby, $\nabla\nabla : (\mathbb{D}c) = \nabla \cdot (\nabla \cdot \mathbb{D}c + \mathbb{D}\nabla c)$ represents myopic diffusion.

We supplement the above RDTEs with the dynamics hyaluron concentration $h$:

$$\partial_t h = \gamma_2 \frac{c_2}{C_2^* + c_2} - \gamma_1 h c_2 \tag{2.2.24}$$

with the source terms on the right hand side characterising production, and uptake of $h$ due to $c_2$.

We supplement system (2.2.22)-(2.2.24) with no-flux boundary conditions (see [23, 25, 83] for deduction of similar boundary conditions)

$$\left( \mathbb{D}_1 \nabla c_1 + \left( \nabla \cdot \mathbb{D}_1 - \frac{k^- \lambda_{11}}{B(h)^2 (B(h) + \lambda_{10})} \mathbb{D}_1 \nabla B(h) \right) c_1 \right) \cdot \nu = 0 \quad \text{on} \quad \partial\Omega \tag{2.2.25}$$

$$(\nabla \cdot \mathbb{D}_2 c_2 + \mathbb{D}_2 \nabla c_2) \cdot \nu = 0 \quad \text{on} \quad \partial\Omega, \tag{2.2.26}$$

where $\Omega$ is a bounded domain in $\mathbb{R}^n$ with sufficiently regular boundary $\partial\Omega$.

## 2.3 Linear stability and bifurcations

In this section, we will study the pattern formation in a simplified version of the mathematical model derived in section 2.2. This study demonstrates that the taxis sensitivity parameter plays an important role in determining the stability of the steady state. When it is sufficiently high, Hopf bifurcations can occur, which lead to spatial and temporal patterns. Our analysis focuses on the steady-state behaviour of the system, utilising a model that incorporates linear diffusion and constant taxis. We consider the following simplified macroscopic model for the dynamics of stem cells, chondrocytes, and hyaluron:

$$\begin{aligned}
\partial_t c_1 &= a_1 \Delta c_1 - \nabla \cdot (b c_1 \nabla h) - \alpha c_1 + \delta c_2 + \beta c_1 (1 - \frac{c_1}{K_{c_1}} - \frac{c_2}{K_{c_1}}), && \text{in } (0,T) \times \Omega, \\
\partial_t c_2 &= a_2 \Delta c_2 + \alpha c_1 - \delta c_2, && \text{in } (0,T) \times \Omega, \\
\partial_t h &= -\gamma_1 h c_2 + \gamma_2 \frac{c_2}{K_{c_1} + c_2}, && \text{in } (0,T) \times \Omega, \\
\partial_\nu c_1 &= \partial_\nu c_2 = \partial_\nu h = 0, && \text{on } (0,T) \times \partial\Omega, \\
c_1(0) &= c_1^0,\ c_2(0) = c_2^0,\ h(0) = h_0 && \text{in } \Omega,
\end{aligned} \tag{2.3.1}$$

where $a_1,\ a_2,\ \alpha,\ \beta,\ \gamma,\ \delta,\ b > 0$ are all positive constants and $\Omega \subset \mathbb{R}^n$ $(n = 2, 3)$ is a bounded domain with sufficiently regular boundary, while $\nu$ represents the outer unit normal on $\partial\Omega$.

The approach to investigate the formation of patterns around the steady state is based on the linear stability analysis of the system (2.3.1). The analysis is similar to that in [61, 67, 68]. There is only one non-trivial steady state for the model system in the absence of motility terms:

$$\left(K_{c_1}\frac{\delta}{\delta+\alpha}, K_{c_1}\frac{\alpha}{\delta+\alpha}, \frac{\gamma_2(\delta+\alpha)}{\gamma_1 K_{c_1}(\delta+2\alpha)}\right) \tag{2.3.2}$$

which can be rewritten as:

$$\left(c_1^*, \frac{\alpha}{\delta}c_1^*, \frac{\gamma_2}{\gamma_1(K_{c_1}+\frac{\alpha}{\delta}c_1^*)}\right) \tag{2.3.3}$$

where $c_1^* = K_{c_1}\dfrac{\delta}{\delta+\alpha}$. We will now discuss the stability of the steady state (2.3.3).

**Theorem 2.3.1.** *The steady state (2.3.3) of the model system (2.3.1) without motility terms is always locally asymptotically stable.*

*Proof.* At any equilibrium solution $(c_1, c_2, h)$, the Jacobian matrix of system (2.3.1) without motility terms is

$$J(c_1,c_2,h) = \begin{pmatrix} -\alpha-\beta\dfrac{c_1}{K_{c_1}}+\beta(1-\dfrac{c_1}{K_{c_1}}-\dfrac{c_2}{K_{c_1}}) & -\beta\dfrac{c_1}{K_{c_1}}+\delta & 0 \\ \alpha & -\delta & 0 \\ 0 & -\gamma_1 h+\dfrac{\gamma_2 K_{c_1}}{(K_{c_1}+c_2)^2} & -c_2\gamma_1 \end{pmatrix}. \tag{2.3.4}$$

Therefore by using (2.3.4) the Jacobian of (2.3.1) at $\left(c_1^*, \frac{\alpha}{\delta}c_1^*, \frac{\gamma_2}{\gamma_1(K_{c_1}+\frac{\alpha}{\delta}c_1^*)}\right)$ is given by

$$J(c_1^*, \tfrac{\alpha}{\delta}c_1^*, \tfrac{\gamma_2}{\gamma_1(K_{c_1}+\frac{\alpha}{\delta}c_1^*)}) := J^* = \begin{pmatrix} -\beta\dfrac{c_1^*}{K_{c_1}}-\alpha & -\beta\dfrac{c_1^*}{K_{c_1}}+\delta & 0 \\ \alpha & -\delta & 0 \\ 0 & -\dfrac{\gamma_2\frac{\alpha}{\delta}c_1^*}{(K_{c_1}+\frac{\alpha}{\delta}c_1^*)^2} & -\gamma_1\dfrac{\alpha}{\delta}c_1^* \end{pmatrix}. \tag{2.3.5}$$

The characteristic equation of $J^*$ is given by:

$$\lambda^3 + A_1\lambda^2 + A_2\lambda + A_3 = 0, \tag{2.3.6}$$

where

$$A_1 = \beta\frac{c_1^*}{K_{c_1}} + \gamma_1\frac{\alpha}{\delta}c_1^* + \alpha + \delta,$$
$$A_2 = \beta\delta\frac{c_1^*}{K_{c_1}} + \beta\alpha\frac{c_1^*}{K_{c_1}} + \alpha\gamma_1 c_1^* + \frac{\alpha\beta\gamma_1}{\delta}\frac{c_1^{*2}}{K_{c_1}} + \frac{\gamma_1\alpha^2}{\delta}{c_1}^*,$$
$$A_3 = \frac{\alpha^2\beta\gamma_1}{\delta}\frac{c_1^{*2}}{K_{c_1}} + \alpha\beta\gamma_1\frac{c_1^{*2}}{K_{c_1}}.$$

Based on the positive values of the parameters, it can be concluded that $A_i > 0,\ i = 1, 2, 3$ and the following has been verified:

$$\begin{aligned}
A_1A_2 - A_3 &= \big(\beta\frac{c_1^*}{K_{c_1}} + \gamma_1\frac{\alpha}{\delta}c_1^* + \alpha + \delta\big)\big(\beta\delta\frac{c_1^*}{K_{c_1}} + \beta\alpha\frac{c_1^*}{K_{c_1}} + \alpha\gamma_1 c_1^* + \frac{\alpha\beta\gamma_1}{\delta}\frac{c_1^{*2}}{K_{c_1}} + \frac{\gamma_1\alpha^2}{\delta}{c_1}^*\big) \\
&\quad - \big(\frac{\alpha^2\beta\gamma_1}{\delta}\frac{c_1^{*2}}{K_{c_1}} + \alpha\beta\gamma_1\frac{c_1^{*2}}{K_{c_1}}\big) \\
&= \big(\gamma_1\frac{\alpha}{\delta}c_1^* + \alpha + \delta\big)\big(\beta\delta\frac{c_1^*}{K_{c_1}} + \beta\alpha\frac{c_1^*}{K_{c_1}} + \alpha\gamma_1 c_1^* + \frac{\alpha\beta\gamma_1}{\delta}\frac{c_1^{*2}}{K_{c_1}} + \frac{\gamma_1\alpha^2}{\delta}{c_1}^*\big) \\
&\quad + \beta\frac{c_1^*}{K_{c_1}}\big(\beta\delta\frac{c_1^*}{K_{c_1}} + \beta\alpha\frac{c_1^*}{K_{c_1}} + \frac{\alpha\beta\gamma_1}{\delta}\frac{c_1^{*2}}{K_{c_1}}\big) \\
&> 0.
\end{aligned}$$

Thus, we can apply the Routh-Hurwitz criterion to conclude that $Re(\lambda_i) < 0,\ i = 1, 2, 3$. Therefore, the steady state is always asymptotically stable in the absence of motility terms. □

We will now turn our attention to the model system with motility terms. In order to perform stability analysis, we linearise (2.3.1) at the steady state (2.3.3) to obtain the following Jacobian matrix:

$$J_j = \begin{pmatrix} -\beta\frac{c_1^*}{K_{c_1}} - \alpha - a_1k_j & -\beta\frac{c_1^*}{K_{c_1}} + \delta & bc_1^*k_j \\ \alpha & -\delta - a_2k_j & 0 \\ 0 & -\frac{\gamma_2\frac{\alpha}{\delta}c_1^*}{(K_{c_1} + \frac{\alpha}{\delta}c_1^*)^2} & -\gamma_1\frac{\alpha}{\delta}c_1^* \end{pmatrix}, \tag{2.3.7}$$

where $\{k_j\}_{j=0}^{\infty}$ denotes the set of eigenvalues of the Laplace operator $-\Delta$ with homogeneous Neumann boundary conditions in a smooth domain $\Omega$. The characteristic polynomial for (2.3.7) is

$$\lambda^3 + (A_j)^{(2)}\lambda^2 + (A_j)^{(1)}\lambda + (A_j)^{(0)} = 0,$$

where

$$(A_j)^{(2)} = \beta\frac{c_1^*}{K_{c_1}} + \gamma_1\frac{\alpha}{\delta}c_1^* + \alpha + \delta + (a_1+a_2)k_j$$

$$(A_j)^{(1)} = a_1a_2{k_j}^2 + (a_1\delta + a_2\alpha + a_2\beta\frac{c_1^*}{K_{c_1}} + \alpha\gamma_1\frac{a_1+a_2}{\delta}c_1^*)k_j + \beta\delta\frac{c_1^*}{K_{c_1}} + \alpha\beta\frac{c_1^*}{K_{c_1}} + \alpha\gamma_1c_1^* + \frac{\alpha^2\gamma_1}{\delta}c_1^* + \frac{\alpha\beta\gamma_1}{\delta}\frac{(c_1^*)^2}{K_{c_1}}$$

$$(A_j)^{(0)} = \frac{a_1a_2\alpha\gamma_1}{\delta}c_1^*{k_j}^2 + \left(\frac{\alpha^2b\gamma_2}{\delta}\frac{(c_1^*)^2}{(K_{c_1}+\frac{\alpha}{\delta}c_1^*)^2} + a_1\alpha\gamma_1c_1^* + \frac{a_2\alpha\beta\gamma_1}{\delta}\frac{(c_1^*)^2}{K_{c_1}} + \frac{a_2\gamma_1\alpha^2}{\delta}c_1^*\right)k_j + \frac{\alpha^2\beta\gamma_1}{\delta}\frac{c_1^{*2}}{K_{c_1}} + \alpha\beta\gamma_1\frac{c_1^{*2}}{K_{c_1}}.$$

A stable steady state requires negative real parts for the eigenvalues of matrix $J_j$ for all $j \geqslant 0$. Using Routh Hurwitz's stability criterion, this corresponds to:

$$(A_j)^{(2)} > 0, \quad (A_j)^{(1)} > 0, \quad (A_j)^{(0)} > 0, \quad \text{and} \tag{2.3.8}$$

$$T(b,j) := (A_j)^{(2)}(A_j)^{(1)} - (A_j)^{(0)} = B_1{k_j}^3 + B_2{k_j}^2 + B_3k_j + B_4 - \frac{\alpha^2b\gamma_2}{\delta}\frac{(c_1^*)^2}{(K_{c_1}+\frac{\alpha}{\delta}c_1^*)^2}k_j > 0, \tag{2.3.9}$$

for all $j \geqslant 0$, with $B_1,\ B_2,\ B_3,\ B_4 \geqslant 0$, due to the positivity of coefficients and non-negativity of eigenvalues. For $k_j = 0$, we have proved in Theorem 2.3.1 that the steady state was stable.

**Remark 2.3.1.** *It can be observed that for $b = 0$ the steady state (2.3.3) satisfies the stability condition.*

It can be easily seen that (2.3.8) is always satisfied, and for $b = 0$, (2.3.9) is

$$(A_j)^{(2)}(A_j)^{(1)} - (A_j)^{(0)} = B_1{k_j}^3 + B_2{k_j}^2 + B_3k_j + B_4 > 0.$$

This indicates that diffusivity alone does not affect the local stability of the steady state, and only taxis towards the hyaluron gradient can cause instability. We can now determine the $b$-dependent stability condition for the steady state (and for $k_j \neq 0$). Consider

$$\psi(k_j) := \frac{B_1{k_j}^3 + B_2{k_j}^2 + B_3k_j + B_4}{\frac{\alpha^2\gamma_2}{\delta}\frac{(c_1^*)^2}{(K_{c_1}+\frac{\alpha}{\delta}c_1^*)^2}k_j} = \frac{\psi_1(k_j)}{\psi_2k_j},$$

where we denoted

$$\psi_1(\zeta) := B_1\zeta^3 + B_2\zeta^2 + B_3\zeta + B_4$$
$$\psi_2 := \frac{\alpha^2\gamma_2}{\delta}\frac{(c_1^*)^2}{(K_{c_1}+\frac{\alpha}{\delta}c_1^*)^2}.$$

Since $\psi_2$ and the coefficients of $\psi_1$¸ are all positive for all $j \geqslant 0$ we have

$$\lim_{x\to 0+} \psi(x) = \lim_{x\to\infty} \psi(x) = \infty \tag{2.3.10}$$

and notice that $\psi$ is a strictly convex function. Hence there exist $b_c$ such that

$$b_c := \min_{j\in\mathbb{N}^+} \frac{\psi_1(k_j)}{\psi_2 k_j}. \tag{2.3.11}$$

When $b < b_c$ , the steady state is stable. If

$$\psi(k_j) \neq \psi(k_m) \quad \text{for } j \neq m, \tag{2.3.12}$$

then the minimum is attained for a single $j = j_0$. This proves the following result.

**Proposition 1.** *The steady state(2.3.3) is locally asymptotically stable if $b < b_c$ defined in (2.3.11).*

Since condition (2.3.8) is always satisfied, the stability of the steady state is determined by condition (2.3.9). When $b < b_c$, then the condition (2.3.9) is satisfied, hence ensuring the stability of the steady state. The following theorem shows the existence of a Hopf bifurcation.

**Theorem 2.3.2.** *For $b = b_c$, if (2.3.12) holds, then a Hopf bifurcation occurs.*

To show the occurrence of a Hopf bifurcation we use [68], [98], and [5]. When (2.3.12) is satisfied we have

$$\begin{aligned} &(i)\ {A_j}^{(2)} = -trace(J_j) > 0,\ {A_j}^{(1)} > 0,\ {A_j}^{(0)}(b) = -det(J_j) > 0 \text{ for all } j \geqslant 0 \text{ and } b > 0;\\ &(ii)\ {A_j}^{(2)}{A_j}^{(1)} = {A_j}^{(0)}(b_c) \text{ for some } j = j_0. \end{aligned} \tag{2.3.13}$$

That means the characteristic polynomial of $J_{j_0}$ has a real negative root $\lambda_1^0 = -{A_{j_0}}^{(2)}$ and a pair of purely imaginary roots $\lambda_2^0,\ \lambda_3^0 = \pm i\sqrt{A_{j_0}^1} = \pm i\omega_0$. Let $\lambda_1(b)$ and $\lambda_{2,3}(b) = \sigma(b) \pm i\omega(b)$ be the eigenvalues of the Jacobian matrix $J_j$ in the neighbourhood of the bifurcation threshold value $b_c$ such that $\lambda_1$, $\sigma$, and $\omega$ are smooth functions of $b$ satisfying $\lambda_1(b_c) = \lambda_1^0$ and $\sigma(b_c) = 0$ and $\omega(b_c) = \omega_0$ . Then we have

$$\begin{aligned} -{A_j}^{(2)} &= 2\sigma(b) + \lambda_1(b)\\ {A_j}^{(1)} &= \sigma(b)^2 + \omega(b)^2 + 2\sigma(b)\lambda_1(b)\\ -{A_j}^{(0)} &= (\sigma(b)^2 + \omega(b)^2)\lambda_1(b). \end{aligned} \tag{2.3.14}$$

From the third equation in (2.3.14), we get $\lambda_1(b) < 0$. On differentiating each equation in (2.3.14) with respect to $b$ we obtain

$$\begin{aligned} &2\sigma'(b) + \lambda_1'(b) = 0\\ &2\sigma(b)\sigma'(b) + 2\omega(b)\omega'(b) + 2\sigma'(b)\lambda_1(b) + 2\sigma(b)\lambda_1'(b) = 0\\ &(\sigma(b)^2 + \omega(b)^2)\lambda_1'(b) + 2\sigma(b)\sigma'(b)\lambda_1(b) + 2\omega(b)\omega'(b)\lambda_1(b) = -\psi_2. \end{aligned} \tag{2.3.15}$$

Therefore, we have $\sigma'(b) = \frac{-\lambda_1'(b)}{2}$ and substituting $\sigma(b_c) = 0$ in the second and third equations of (2.3.15) we get

$$2\omega(b_c)\omega'(b_c) + 2\sigma'(b_c)\lambda_1(b_c) = 0 \quad \text{and} \quad \omega(b_c)^2\lambda_1'(b_c) + 2\omega(b_c)\omega'(b_c)\lambda_1(b_c) = -\psi_2.$$

Hence by solving the system we obtain

$$\lambda_1'(b_c) = -\frac{\psi_2}{\omega(b_c)^2 + \lambda_1(b_c)^2} < 0 \quad \text{hence} \quad \sigma'(b_c) > 0. \tag{2.3.16}$$

Therefore, the transversality condition for a Hopf bifurcation is satisfied at $b = b_c$.

## 2.4 Numerical simulations and patterns

To demonstrate the pattern-based behaviour of the model, we perform numerical simulations. We simulate the simplified model for different values of $b$.

### 2.4.1 1D simulations

We use Matlab's `pdepe` to solve system (2.3.1) in one dimension. We fix a specific set of positive parameters as given below.

$$a_1 = 0.015; \quad a_2 = 0.007; \quad \delta = 0.6; \quad \beta = 0.05; \quad \alpha = 0.15; \quad \gamma_1 = 0.1; \quad \gamma_2 = 0.3.$$

Using the specified set of parameters, we determine the critical value $b_c$ to be 3.34. Stability analysis indicates that bifurcation occurs when $b$ exceeds $b_c$. This critical value serves as a threshold, beyond which the system undergoes a qualitative change in behaviour.

To investigate the system's response to different initial conditions, we examine two primary scenarios: one where $b$ is greater than $b_c$ and another where $b$ is less than $b_c$. We perturb the steady state described by (2.3.3) and summarise our findings through four distinct simulation scenarios:

**Scenario 1:** $x \in [0, 1]$, perturbed initial amount of chondrocytes:

$$c_1(x, 0) = c_1^*,\ c_2(x, 0) = c_2^* + 0.1\exp(-(x - .5)^2/0.2),\ h(x, 0) = h^*,\ b = 3.7\ (b = 1.8).$$

**Scenario 2:** $x \in [0, 1]$, perturbed initial amount of stem cells:

$$c_1(x, 0) = c_1^* + 0.1\exp(-(x - .5)^2/0.2),\ c_2(x, 0) = c_2^*,\ h(x, 0) = h^*,\ b = 3.7\ (b = 1.8).$$

**Scenario 3:** $x \in [0, 1]$, perturbed initial amount of hyaluron:

$$c_1(x, 0) = c_1^*,\ c_2(x, 0) = c_2^*,\ h(x, 0) = h^* + 0.1\exp(-(x - .5)^2/0.2),\ b = 3.7\ (b = 1.8).$$

**Scenario 4:** $x \in [0, 10]$, perturbed initial amounts of stem cells and hyaluron:

$$c_1(x, 0) = c_1^* + .01\cos(4\pi(x - 5)/10),\ c_2(x, 0) = c_2^*,\ h(x, 0) = h^* + .01\cos(4\pi(x - 5)/10),$$
$$b = 3.7\ (b = 1.8).$$

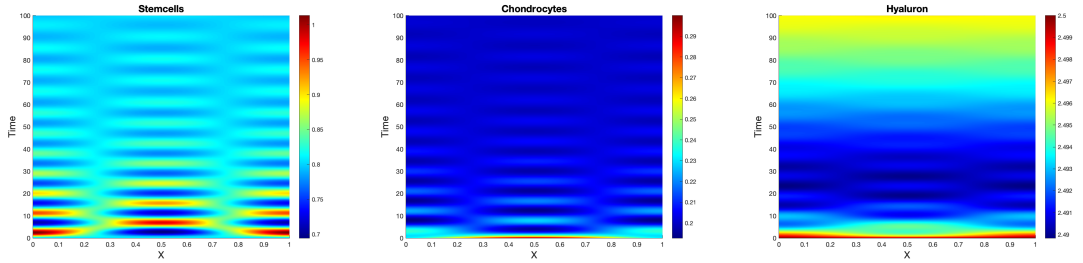


(a) Stem cells for $b = 3.7$ (b) Chondrocytes for $b = 3.7$ (c) Hyaluron for $b = 3.7$

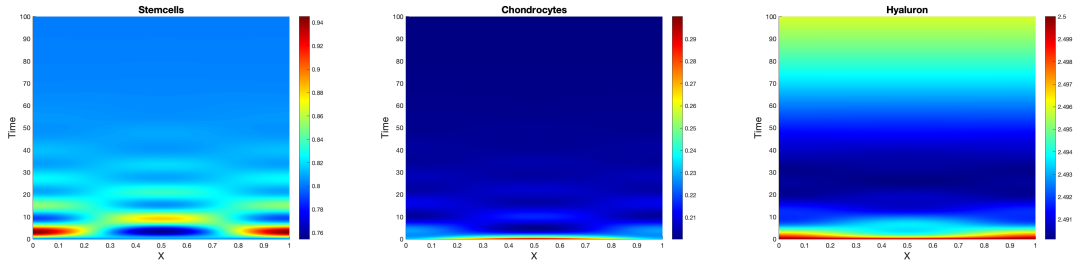


(d) Stem cells for $b = 1.8$ (e) Chondrocytes for $b = 1.8$ (f) Hyaluron for $b = 1.8$

Figure 2.1: Stem cells, chondrocyte, and hyaluron density for Scenario 1. Upper row: $b > b_c$, lower row $b < b_c$.

These scenarios allow us to analyse the system's dynamics and understand the conditions under which pattern formation emerges.

Figure 2.1 presents the simulated patterns for Scenario 1. The upper row of plots shows the case where the tactic sensitivity coefficient $b$ exceeds the critical bifurcation value $b_c$, while the lower row illustrates the scenario where $b$ is below $b_c$. As expected, when $b > b_c$, all three solution components display oscillatory behaviour, with stem cells and chondrocytes exhibiting particularly pronounced oscillations, indicative of motility. Due to diffusion and dispersion across the domain of simulation, these oscillations gradually decrease at a slow rate. Conversely, when $b < b_c$, the initial perturbation of the system's steady state quickly subsides, aligning with the results described in Proposition 1.

A variation in the overall behaviour of the system is observed when the same initial perturbation of steady states is applied to different solution components. Figures 2.2 and 2.3, corresponding to Scenarios 2 and 3, respectively, exemplify this. In Scenario 2, featuring a perturbation of stem cell density, Figure 2.2 exhibits behaviour similar to that of Figure 2.1, albeit with quicker stabilisation at lower densities. On the other hand, Scenario 3 introduces a perturbation of hyaluron, which serve as the tactic signal. This leads to substantially weaker oscillations, even when $b > b_c$, which dampens rapidly. Moreover, higher densities of stem cells, chondrocytes, and hyaluron are achieved, indicating a more favourable outcome for tissue regeneration.

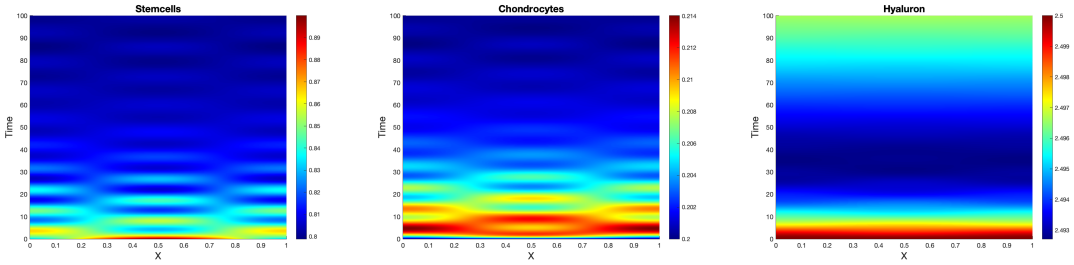


(a) Stem cells for $b = 3.7$ (b) Chondrocytes for $b = 3.7$ (c) Hyaluron for $b = 3.7$

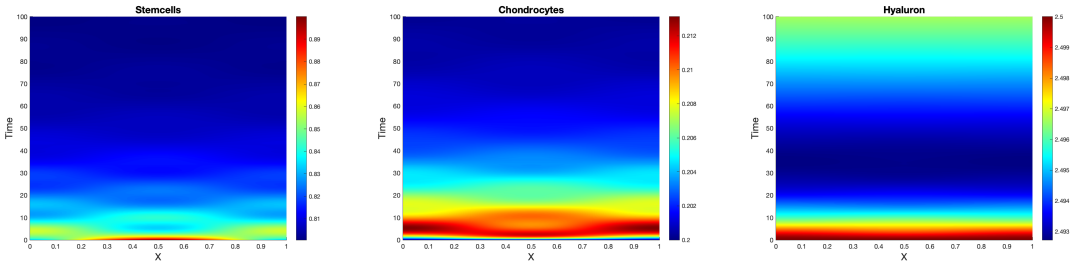


(d) Stem cells for $b = 1.8$ (e) Chondrocytes for $b = 1.8$ (f) Hyaluron for $b = 1.8$

Figure 2.2: Stem cell, chondrocyte, and hyaluron density for Scenario 2. Upper row: $b > b_c$, lower row $b < b_c$.

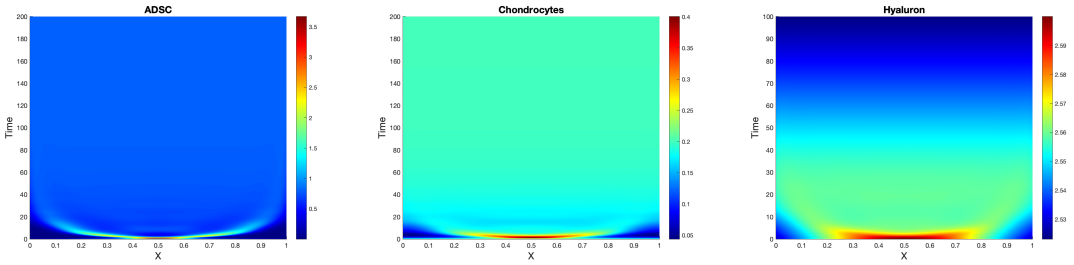


(a) Stem cells for $b = 3.7$ (b) Chondrocytes for $b = 3.7$ (c) Hyaluron for $b = 3.7$

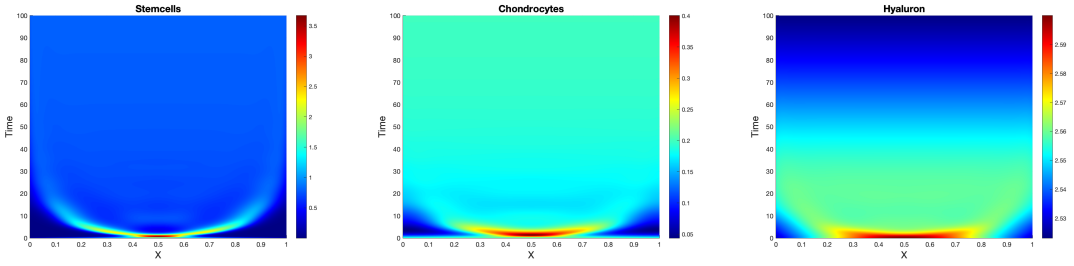


(d) Stem cells for $b = 1.8$ (e) Chondrocytes for $b = 1.8$ (f) Hyaluron for $b = 1.8$

Figure 2.3: Stem cell, chondrocyte, and hyaluron density for Scenario 3. Upper row:$b > b_c$, lower row $b < b_c$.

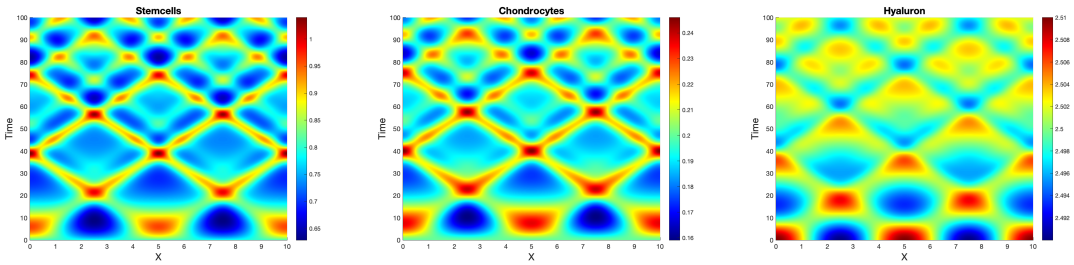


(a) Stem cells for $b = 3.7$ (b) Chondrocytes for $b = 3.7$ (c) Hyaluron for $b = 3.7$

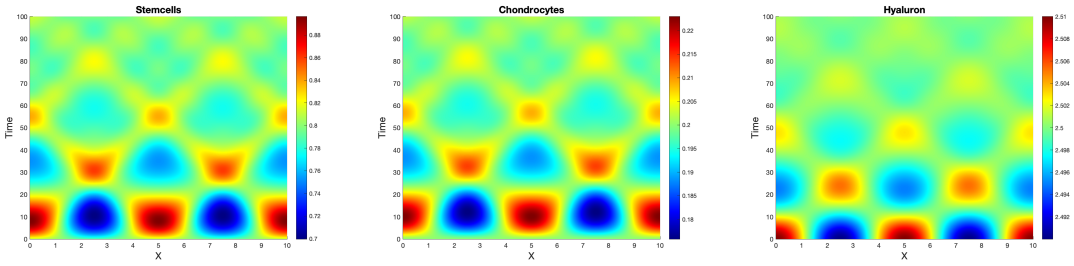


(d) Stem cells for $b = 1.8$ (e) Chondrocytes for $b = 1.8$ (f) Hyaluron for $b = 1.8$

Figure 2.4: Stem cell, chondrocyte, and hyaluron density for Scenario 4. Upper row: $b > b_c$, lower row $b < b_c$.

Scenario 4 considers periodic perturbations to the stem cells and hyaluron steady states and expands the simulation domain by tenfold. The simulation results are depicted in Figure 2.4. Interestingly, the periodic patterns observed bear some resemblance to the cosine-based perturbations used but occur only when the domain size is sufficiently large.

These periodic patterns are a consequence of stem cells responding to gradients of $h$, primarily governed by chondrocytes' dynamics. The alternation between regions of high and low cell densities in the solution components is a direct outcome of this process. Notably, when the tactic sensitivity $b$ is sufficiently small ($b < b_c$), the system stabilises more rapidly, resulting in lower densities of both cell phenotypes and hyaluron overall.

### 2.4.2 2D simulations

The 2D discretisation of the model is done using the finite difference method (FDM). A standard central difference scheme is used to discretise the diffusion parts of the equations for stem cells and chondrocytes, while the taxis term in the stem cell equation was handled by a first-order upwind scheme. For the time derivatives an implicit-explicit (IMEX) [9] scheme is used, thereby treating the diffusion parts implicitly and discretising the taxis and source terms with an explicit Euler method.

The initial conditions considered in this case are

$$\begin{aligned} c_1(x,0) &= c_1^* + 10^{-6}\exp(-((x-5)^2+(y-5)^2)/.2), \\ c_2(x,0) &= c_2^* + 10^{-9}\exp(-((x-5)^2+(y-5)^2)/.2),\ h(x,0) = 1 + 10^{-6}U, \end{aligned} \tag{2.4.1}$$

where $U$ represents a uniform distribution within $(0,1)$. Figure 2.5 shows their plots.

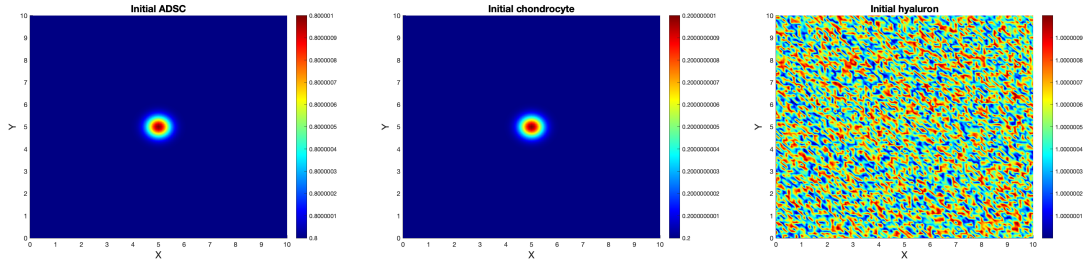


(a) Stem cell (b) Chondrocytes (c) Hyaluron

Figure 2.5: Initial conditions (2.4.1) for Stem cell, chondrocyte, and hyaluron density.

Figure 2.6 presents the 2D simulation outcomes for system (2.3.1) under the initial conditions specified in (2.4.1). The densities of stem cells, chondrocytes, and hyaluron are depicted at 7, 14, and 21 days. In this scenario, the tactic sensitivity parameter $b$ is set to 3.7, surpassing the threshold obtained in Section 2.3 as the Hopf bifurcation value.

The simulation reveals that cells quickly diffuse from their initial positions. Stem cells exhibit enhanced motility due to taxis towards gradients of the signal $h$, with chondrocytes following suit as they arise solely from stem cell differentiation. This dynamic is further explored in Figure 2.7, which displays the evolution of $c_1$, $c_2$, and $h$ for a lower tactic sensitivity parameter, $b = 1.8 < b_c$. The higher tactic sensitivity of stem cells appears to result in slightly higher cell densities, as in the 1D case.

To investigate the effect of initial hyaluron (and hence of tissue) distribution we considered the following initial condition

$$\begin{aligned} c_1(x,0) &= c_1^* + 10^{-6}\exp(-((x-5)^2+(y-5)^2)/.2), \\ c_2(x,0) &= c_2^* + 10^{-9}\exp(-((x-5)^2+(y-5)^2)/.2),\ h(x,0) = 1 + 10^{-6}U\cos(4\pi(x-5)/10). \end{aligned} \tag{2.4.2}$$

This is depicted in the following figure 2.8

The simulation results shown in Figure 2.9 offer further insights into the dynamics of cells within the context of our study. These outcomes highlight a more pronounced manifestation of the previously discussed behaviour: cells dispersing from their initial concentration, with stem cells showing a strong tendency to follow the hyaluron signal, subsequently inducing chondrocyte migration. This phenomenon results in increased cell and hyaluron

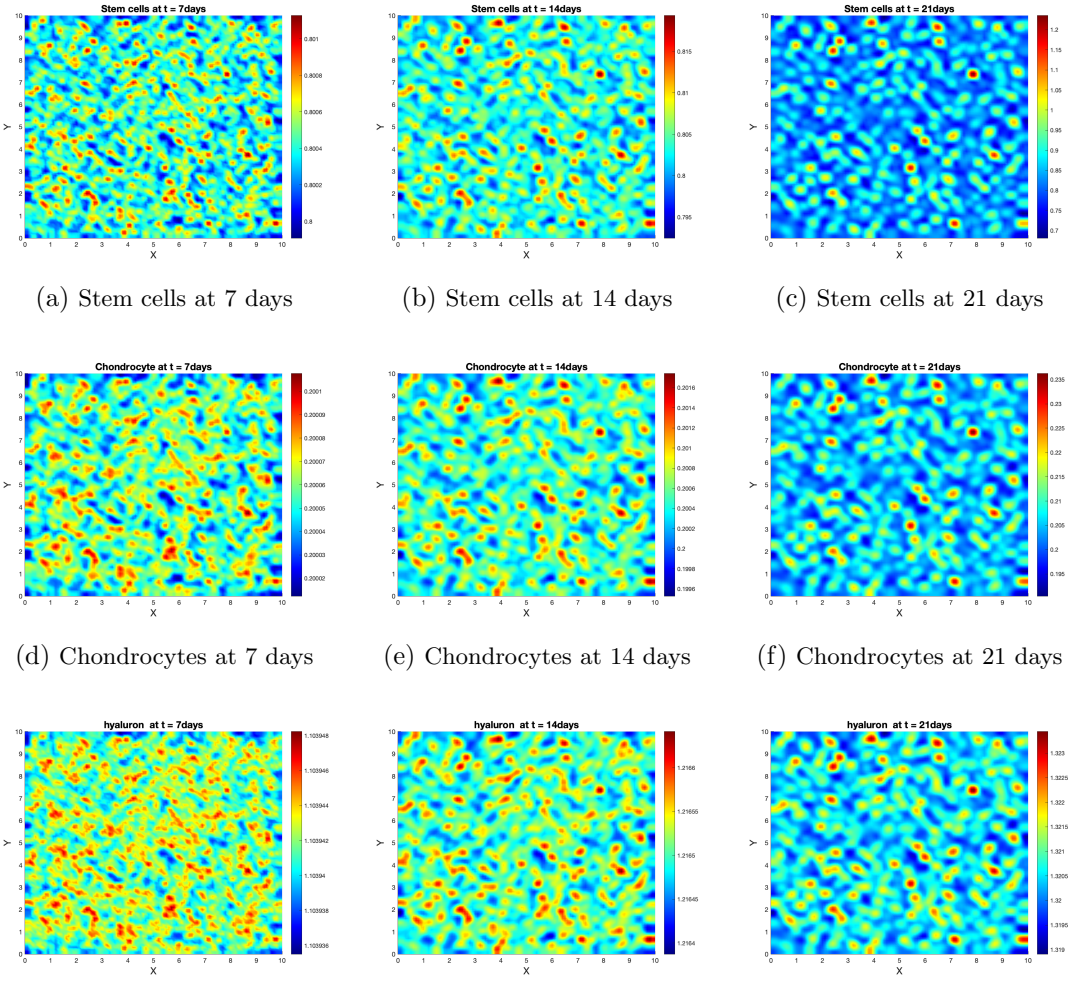


(a) Stem cells at 7 days (b) Stem cells at 14 days (c) Stem cells at 21 days

(d) Chondrocytes at 7 days (e) Chondrocytes at 14 days (f) Chondrocytes at 21 days

(g) Hyaluron at 7 days (h) Hyaluron at 14 days (i) Hyaluron at 21 days

Figure 2.6: Stem cell, chondrocyte, and hyaluron density at 7, 14, and 21 days, initial conditions (2.4.1), $b > b_c$ (here $b = 3.7$)

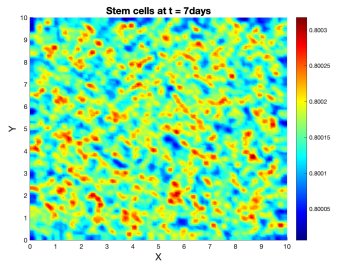


(a) Stem cells at 7 days

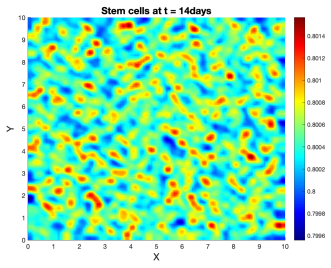


(b) Stem cells at 14 days

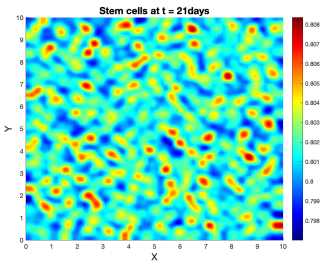


(c) Stem cells at 21 days

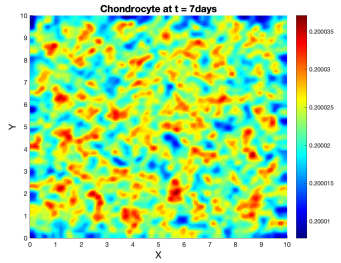


(d) Chondrocytes at 7 days

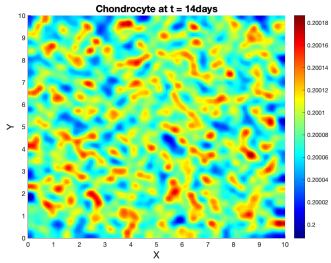


(e) Chondrocytes at 14 days

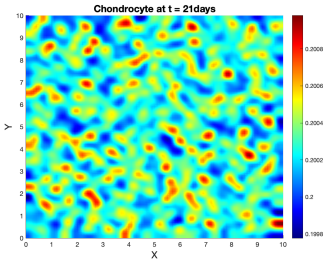


(f) Chondrocytes at 21 days

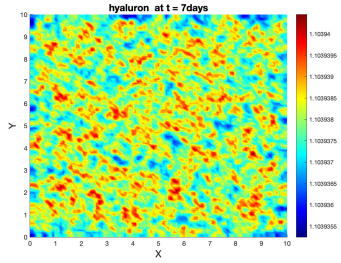


(g) Hyaluron at 7 days

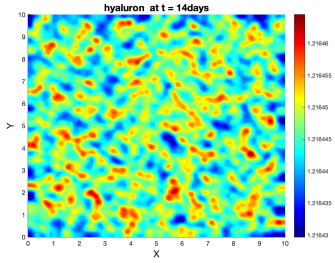


(h) Hyaluron at 14 days

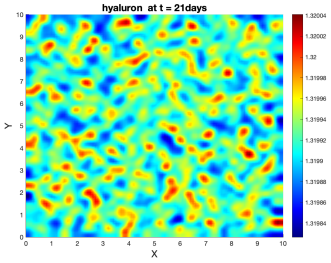


(i) Hyaluron at 21 days

Figure 2.7: Stem cell, chondrocyte, and hyaluron at 7, 14, and 21 days, initial conditions (2.4.1), $b < b_c$ (here $b = 1.8$)

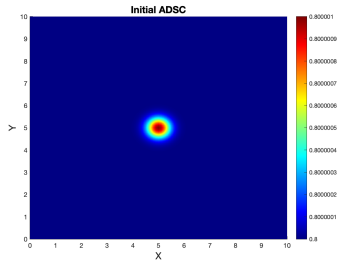


(a) Stem cells

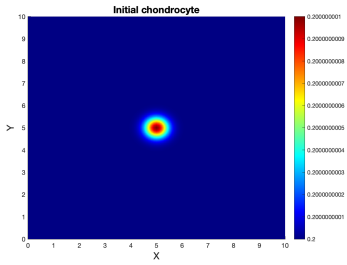


(b) Chondrocytes

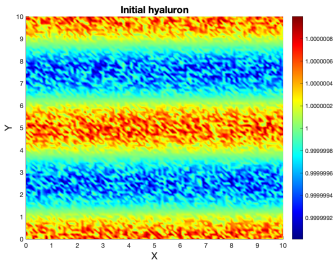


(c) Hyaluron

Figure 2.8: Initial conditions (2.4.2) for Stem cell, chondrocyte, and hyaluron.

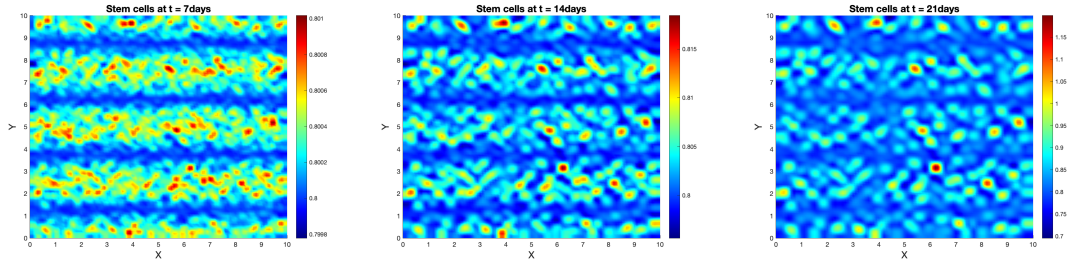


(a) Stem cells at 7 days (b) Stem cells at 14 days (c) Stem cells at 21 days

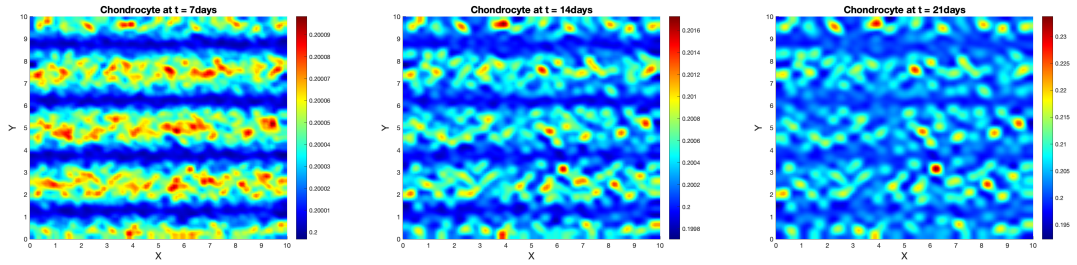


(d) Chondrocytes at 7 days (e) Chondrocytes at 14 days (f) Chondrocytes at 21 days

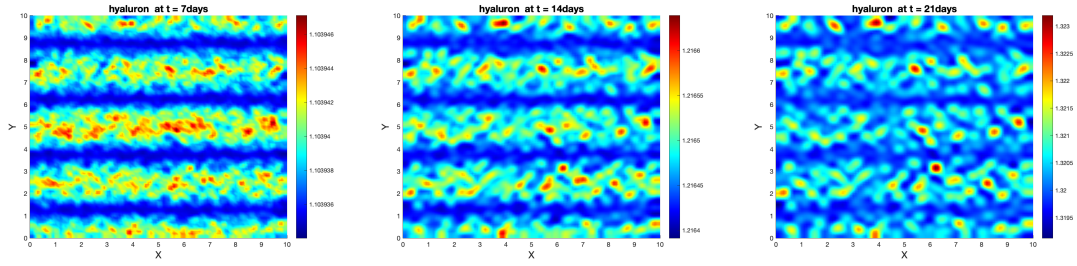


(g) Hyaluron at 7 days (h) Hyaluron at 14 days (i) Hyaluron at 21 days

Figure 2.9: Stem cell, chondrocyte, and hyaluron density at 7, 14, and 21 days, initial conditions (2.4.2), $b > b_c$ (here $b = 3.7$)

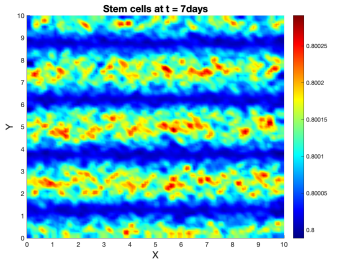


(a) Stem cells at 7 days

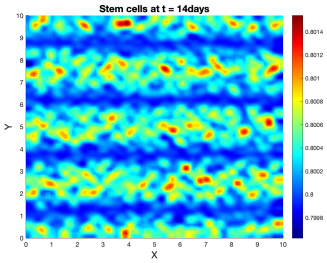


(b) Stem cells at 14 days

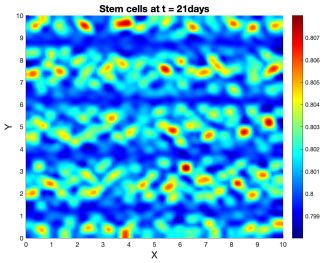


(c) Stem cells at 21 days

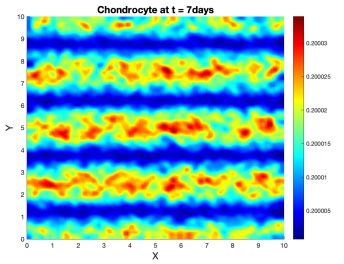


(d) Chondrocytes at 7 days

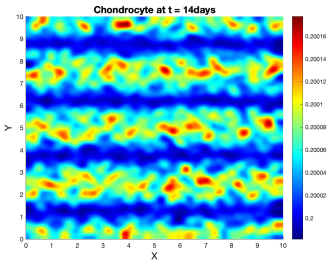


(e) Chondrocytes at 14 days

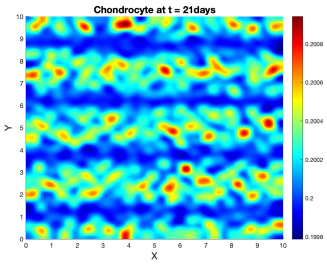


(f) Chondrocytes at 21 days

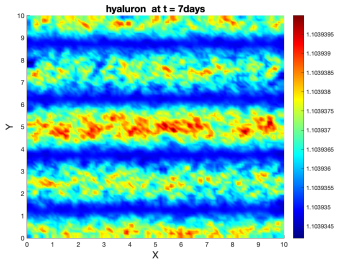


(g) Hyaluron at 7 days

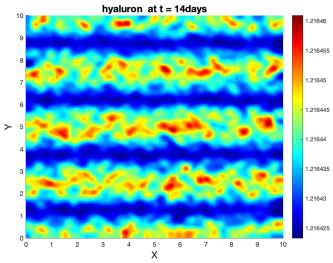


(h) Hyaluron at 14 days

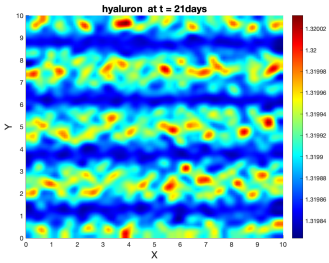


(i) Hyaluron at 21 days

Figure 2.10: Stem cell, chondrocyte, and hyaluron density at 7, 14, and 21 days, initial conditions (2.4.2), $b < b_c$ (here $b = 1.8$)

densities along the 'stripes' generated by the cosine function in (2.4.2).

As a result of these findings, it is evident that the initial structural configuration of the hyaluron plays a key role in regeneration. Specifically, they highlight the pivotal role that properly designed scaffolds, which facilitate cell migration, can play in influencing both the quantity and quality of newly generated tissue. The scaffolds are capable of supporting stem cell seeding and promoting sustained differentiation into chondrocytes, thereby enhancing the efficacy of tissue regeneration strategies.

Until now we studied the application of mathematical models to understand and facilitate tissue regeneration processes, particularly focusing on the dynamics of tissue repair within the meniscus. In the next chapter, we turn our attention to another critical aspect of tissue biology: the process of wound formation. Specifically, we will delve into a common scenario of wound development, using the example of Buruli ulcer as a representative case study.

Chapter 3

# Multiscale model for Buruli ulcer wound

## 3.1 Introduction

The development of mathematical models to visualise the processes involved in the formation of wounds is as important as tissue regeneration in the field of medicine. In order to formulate an effective treatment plan, it is very important to understand how a wound spreads or how bacteria migrate in nearby tissues. This chapter represents a critical juncture in our investigation, as we pivot from the realm of tissue regeneration to that of wound formation, with a specific focus on the Buruli ulcer as a paradigm. By leveraging mathematical modelling techniques, we aim to gain a deeper understanding of the underlying mechanisms driving wound development, including the migration and proliferation of pathogenic bacteria, the production and migration of toxins such as mycolactone, and the subsequent necrosis of surrounding tissue.

Buruli ulcer presents a typical scenario characterised by tissue degradation, where imaging methods often face limitations in determining the extent of bacterial spread over time. Mathematical models have emerged as valuable tools in such scenarios, aiding in predicting bacterial spread when traditional imaging techniques fall short. Similar to their applications in understanding cancer cell migration in heterogeneous environments, mathematical models hold promise for predicting the spread of Buruli ulcer within infected human bodies, potentially enabling better disease control.

The pathogenesis of Buruli ulcer involves the infiltration of Mycobacterium ulcerans through insect bites into subcutaneous tissue. Although the exact mode of transmission is unclear [50], there is strong evidence that BU does not transfer from person to person. Instead, it might be due to bites by some water-living insects [6, 97]. The bacteria then proliferate, producing a toxin called mycolactone [84]. The toxin spreads from the initial site of infection, penetrating the surrounding areas and diffusing further, resulting in the necrosis of affected tissue [99]. This creates an environment conducive to the continued proliferation of the pathogen [97]. The bacteria invades regions with high concentrations of normal [73] and necrotic tissue, where they further proliferate and produce more toxin, facilitating the sustained spread of lesions.

To characterise the spread of Buruli ulcer lesions within the body, we employ an approach based on KTEs. The utilisation of KTEs for modelling Buruli ulcer represents a pioneering endeavour, as previous applications of KTEs have predominantly focused on biological phenomena such as cell migration and tumour invasion. The studies conducted in [23], [47], [51], [55], [93] offer valuable insights into multiscale modelling approaches, which are inherently connected to the innovative use of KTEs in our research. By drawing upon these works and applying mathematical techniques, we aim to advance our understanding of Buruli ulcer pathogenesis and contribute to the development of more effective strategies for disease management. Our methodology is based on constructing a multi-scale model that initially considers mesoscale interactions among pathogens, necrotic tissue, and normal tissue. By analysing these interactions and taking parabolic limits, we derive a macroscopic system of RDTEs and ODEs. These equations describe the dynamics of the densities of bacteria, normal tissue, necrotic tissue, and mycolactone, thus providing a comprehensive framework for modelling disease progression.

In the first section of this chapter, we build a mathematical model using the kinetic transport equations. This model carefully considers all relevant biological factors discussed earlier, aiming to provide a comprehensive understanding of the disease's progression. Moving forward, we conduct a detailed mathematical analysis to establish the existence of a global classical solution. To illustrate the model predictions and to get insight, we then employ numerical simulations.

## 3.2 Mathematical modelling

### 3.2.1 Mesoscale

Using kinetic transport equations that describe the velocity jump process, we begin by modelling the mesoscale behaviour of bacteria. To develop a macroscopic equation for bacteria we start with the mesoscopic level rather than the microscopic level, similar to the the deduction of the macroscopic equation for chondrocytes in Chapter 2. At the mesoscopic level, our model delves into the interactions between bacterial cells and their surrounding environment, including necrotic matter, normal tissue and neighbouring bacterial cells. These interactions influence various aspects of bacterial behaviour, such as their movement and growth rates. Specifically, we focus on how these interactions affect bacterial invasion and proliferation, as well as their potential consequences on necrotisation of normal tissue.

We consider $u(t, x, \vartheta)$ as the mesoscopic cell density function of bacteria. The time and the space variables are denoted by $t > 0$ and $x \in \mathbb{R}^d$. The velocity is defined as $\vartheta \in \Theta = s\mathbb{S}^{d-1}$ over the unit sphere. The (average) speed of the bacteria, $s > 0$ is thereby assumed to be constant. Therefore, we are only concerned with the direction of the cell velocity. We consider the following kinetic transport equation for bacteria

$$\partial_t u + \nabla_x \cdot (\vartheta u) = \mathcal{L}_u[\eta]u + \mu_u(U, V, N)u, \tag{3.2.1}$$

where the turning operator, $\mathcal{L}_u[\eta]u$ describes the reorientation of the bacteria. Since bacteria are attracted by normal tissue and necrotic matter, we propose the following

turning operator:

$$\mathcal{L}_u[\eta]u = -\eta(x,\vartheta,V,N)u(t,x,\vartheta) + \int_\Theta \frac{1}{|\Theta|}\eta(x,\vartheta',V,N)u(\vartheta')d\vartheta',$$

where for the turning kernel which describes the reorientation of cells we take the uniform density function over the unit sphere. The turning rate $\eta$ is chosen in the form (see [24],[56] for similar approaches in different contexts)

$$\eta(x,\vartheta,V,N) = \eta_0(x)e^{-a(V,N)(\frac{\gamma_1}{K_N}D_tN + \frac{\gamma_2}{K_V}D_tV)},$$

where $\eta_0(x)$ is the turning rate in the absence of external cues, $K_V, K_N > 0$ are the carrying capacities of $V$ and $N$, respectively. The coefficient functions $\frac{\gamma_1}{K_N}a(V,N)$ and $\frac{\gamma_2}{K_V}a(V,N)$ are related to interactions between bacteria and normal tissue as well as necrotic matter, respectively. The constants $\gamma_1, \gamma_2 > 0$ account for the change in the turning rate per unit of change in $dy^*/dN$ and $dy^*/dV$, respectively. $y^*$, which corresponds to the equilibrium of bacteria receptor binding dynamics to $N$ and $V$, is given as follows:

$$y^* = \frac{\frac{N}{K_N} + \frac{V}{K_V}}{\frac{N}{K_N} + \frac{V}{K_V} + 1}.$$

Then we have

$$\frac{dy^*}{dN} = \frac{\frac{1}{K_N}}{(1 + \frac{N}{K_N} + \frac{V}{K_V})^2}$$

$$\frac{dy^*}{dV} = \frac{\frac{1}{K_V}}{(1 + \frac{N}{K_N} + \frac{V}{K_V})^2}.$$

The function $a(V,N)$ is chosen as

$$a(V,N) := \frac{1}{(1 + \frac{N}{K_N} + \frac{V}{K_V})^2}.$$

To make this description, we use some results of the studies [24, 76]. The turning rate $\eta$ also depends on the pathwise gradients of necrotic and normal cells

$$\begin{aligned} D_tN &= \partial_tN + \vartheta \cdot \nabla N \\ D_tV &= \partial_tV + \vartheta \cdot \nabla V. \end{aligned}$$

In the equation (3.2.1), $\mu_u(U,V,N)u$ represents the proliferation term of bacteria. It also depends on the macroscopic cell densities of bacteria $U$, necrotic matter $N$, and normal tissue $V$.

### 3.2.2 Macroscopic scale

Equation (3.2.1) above involves higher dimensions, is formulated on a mesoscopic scale, and has to be coupled with the dynamics of $N$ and $V$, which are macroscopic. The numerical solution of such a system would be challenging, not to speak about boundary conditions.

Hence we aim to deduce an effective macroscopic equation for bacteria density. This is done by rescaling the time and space variables by $t \to \epsilon^2 t$ and $x \to \epsilon x$ where $\epsilon$ is a small dimensionless parameter. A diffusion-dominated equation is thus derived, which allows for a more accurate representation of bacterial movement than merely heuristic settings done directly on the macroscale. Since proliferation is much slower than migration we rescale the source term also by $\epsilon^2$. Hence (3.2.1) becomes

$$\epsilon^2 \partial_t u + \epsilon \nabla_x \cdot (\vartheta u) = \mathcal{L}_u[\eta]u + \epsilon^2 \mu_u(U, V, N)u. \tag{3.2.2}$$

$\eta$ after rescaling is given as follows:

$$\eta(x, \vartheta, V, N) = \eta_0(x) exp\left(-a(V,N)(\epsilon^2 \frac{\gamma_1}{K_N}\partial_t N + \epsilon \frac{\gamma_1}{K_N}\vartheta \cdot \nabla N + \epsilon^2 \frac{\gamma_2}{K_V}\partial_t V + \epsilon \frac{\gamma_2}{K_V}\vartheta \cdot \nabla V)\right).$$

We define the following moment with respect to $\vartheta$:

$$U(t,x) = \int_\Theta u(t,x,\vartheta)d\vartheta.$$

Accordingly, we will use Hilbert expansions for moments:

$$u(t,x,\vartheta) = \sum_{k=0} \epsilon^k u_k, \quad U(t,x) = \sum_{k=0} \epsilon^k U_k,$$

and the Taylor expansions for functions in (3.2.2) are

$$\begin{aligned}
\mu_u(U,V,N) &= \mu_u(U_0,V,N) + \partial_U \mu_u(U_0,V,N)(U-U_0) + O|U-U_0|^2 \\
\eta(x,\vartheta,V,N) &= \eta_0(x)\Big[1 - \epsilon a(V,N)(\frac{\gamma_1}{K_N}\vartheta\cdot\nabla N + \frac{\gamma_2}{K_V}\vartheta\cdot\nabla V) \\
&\quad + \epsilon^2\Big( - a(V,N)(\frac{\gamma_1}{K_N}\partial_t N + \frac{\gamma_2}{K_V}\partial_t V) + \frac{a(V,N)^2}{2}\big((\frac{\gamma_1}{K_N}\vartheta\cdot\nabla N)^2 \\
&\quad + (\frac{\gamma_2}{K_V}\vartheta\cdot\nabla V)^2 + 2\frac{\gamma_1}{K_N}\frac{\gamma_2}{K_V}(\vartheta\cdot\nabla N)(\vartheta\cdot\nabla V)\big)\Big) + O(\epsilon^3)\Big].
\end{aligned} \tag{3.2.3}$$

By equating powers of $\epsilon$ in equation (3.2.2), we obtain

$\epsilon^0$ :

$$0 = -\eta_0 u_0 + \frac{1}{|\Theta|}\int_\Theta \eta_0(x)u_0(\vartheta')d\vartheta' = \eta_0(\frac{1}{|\Theta|}U_0 - u_0), \tag{3.2.4}$$

where $\frac{1}{|\Theta|} = \frac{s^{1-d}}{|\mathbb{S}^{d-1}|}$.

$\epsilon^1$ :

$$\nabla_x \cdot (\vartheta u_0) = \eta_0(x)\Big[\frac{1}{|\Theta|}U_1(t,x) - u_1(t,x,\vartheta) + a(V,N)\big(\frac{\gamma_1}{K_N}\vartheta\cdot\nabla N + \frac{\gamma_2}{K_V}\vartheta\cdot\nabla V\big)u_0$$

$$- \frac{1}{|\Theta|}\, a(V,N) \int_\Theta u_0(\vartheta')\vartheta' d\vartheta' \cdot \big(\frac{\gamma_1}{K_N}\nabla N + \frac{\gamma_2}{K_V}\nabla V\big)\Big] \tag{3.2.5}$$

$\epsilon^2$ :

$$\begin{aligned}
\partial_t u_0 + \nabla_x \cdot (\vartheta u_1) =& \eta_0(x)\Big[\Big(a(V,N)\big(\frac{\gamma_1}{K_N}\partial_t N + \frac{\gamma_2}{K_V}\partial_t V\big) - \frac{a(V,N)^2}{2}\big(\big(\frac{\gamma_1}{K_N}\vartheta\cdot\nabla N\big)^2 \\
&+ \big(\frac{\gamma_2}{K_V}\vartheta\cdot\nabla V\big)^2 + 2\frac{\gamma_1}{K_N}\frac{\gamma_2}{K_V}(\vartheta\cdot\nabla N)(\vartheta\cdot\nabla V)\big)\Big)u_0 \\
&+ a(V,N)\big(\frac{\gamma_1}{K_N}\vartheta\cdot\nabla N + \frac{\gamma_2}{K_V}\vartheta\cdot\nabla V\big)u_1 - u_2\Big] \\
&+ \frac{1}{|\Theta|}\eta_0(x)\Big[U_2 - a(V,N)\int_\Theta \vartheta' u_1(\vartheta')d\vartheta'\cdot\big(\frac{\gamma_1}{K_N}\nabla N + \frac{\gamma_2}{K_V}\nabla V\big) \\
&- a(V,N)\big(\frac{\gamma_1}{K_N}\partial_t N + \frac{\gamma_2}{K_V}\partial_t V\big)U_0 \; + \frac{a(V,N)^2}{2}\int_\Theta\Big(\big(\frac{\gamma_1}{K_N}\vartheta'\cdot\nabla N\big)^2 \\
&+ \big(\frac{\gamma_2}{K_V}\vartheta'\cdot\nabla V\big)^2 + 2\frac{\gamma_1}{K_N}\frac{\gamma_2}{K_V}(\vartheta'\cdot\nabla N)(\vartheta'\cdot\nabla V)\Big)u_0(\vartheta')d\vartheta'\Big] \\
&+ \mu_u(U_0,V,N)u_0.
\end{aligned} \tag{3.2.6}$$

By using (3.2.4), we have

$$u_0 = \frac{1}{|\Theta|}U_0, \tag{3.2.7}$$

which means $u_0$ depends on the constant speed $s$.
Now let us consider equation (3.2.5). Using (3.2.7) we get

$$\nabla_x\cdot(\vartheta u_0) = \eta_0(x)\Big[\frac{1}{|\Theta|}U_1(t,x) - u_1(t,x,\vartheta) + a(V,N)\big(\frac{\gamma_1}{K_N}\vartheta\cdot\nabla N + \frac{\gamma_2}{K_V}\vartheta\cdot\nabla V\big)u_0\Big] \tag{3.2.8}$$

and therefore, as e.g. in [32, 77] we have the compact Hilbert-Schmidt operator

$$\begin{aligned}
\mathcal{L}_u[\eta_0(x)]u_1 &= -\eta_0(x)u_1 + \frac{1}{|\Theta|}\eta_0(x)U_1 \\
&= \nabla_x\cdot(\vartheta u_0) - a(V,N)\big(\frac{\gamma_1}{K_N}\vartheta\cdot\nabla N + \frac{\gamma_2}{K_V}\vartheta\cdot\nabla V\big)u_0
\end{aligned}$$

defined on $L^2$ space. We can therefore calculate its pseudo-inverse to get an expression for $u_1$ :

$$u_1 = -\frac{1}{\eta_0(x)}\nabla_x\cdot(\vartheta u_0) + a(V,N)\big(\frac{\gamma_1}{K_N}\vartheta\cdot\nabla N + \frac{\gamma_2}{K_V}\vartheta\cdot\nabla V\big)u_0 \tag{3.2.9}$$

Again by using (3.2.9) in (3.2.8), we get

$$U_1 = 0. \tag{3.2.10}$$

Integrating (3.2.6) with respect to $\vartheta$, we get the macroscopic equation for bacteria as:

$$\partial_t U_0 + \int_\Theta \nabla_x \cdot (\vartheta u_1) d\vartheta = \mu_u(U_0, V, N) U_0. \tag{3.2.11}$$

To compute the integral on left-hand side, by using (3.2.9) we have

$$\begin{aligned}
\int_\Theta \nabla_x \cdot (\vartheta u_1) d\vartheta &= \int_\Theta \nabla_x \cdot \left[ \vartheta \Big( -\frac{1}{\eta_0(x)} \nabla_x \cdot (\vartheta u_0) + a(V,N)(\frac{\gamma_1}{K_N} \vartheta \cdot \nabla N + \frac{\gamma_2}{K_V} \vartheta \cdot \nabla V) u_0 \Big) \right] d\vartheta \\
&= \nabla_x \cdot \big[ \int_\Theta -\frac{1}{\eta_0(x)} \vartheta \otimes \vartheta \nabla_x (\frac{1}{|\Theta|} U_0) d\vartheta \big] \\
&\quad + \nabla_x \cdot \big[ \frac{a(V,N)}{|\Theta|} \int_\Theta \vartheta \otimes \vartheta d\vartheta (\frac{\gamma_1}{K_N} \nabla N + \frac{\gamma_2}{K_V} \nabla V) U_0 \big] \\
&= -\nabla \cdot (\mathbb{D}_u \nabla U_0) + \nabla \cdot \big( \chi_a(V,N) (\frac{\gamma_1}{K_N} \nabla N + \frac{\gamma_2}{K_V} \nabla V) U_0 \big)
\end{aligned} \tag{3.2.12}$$

where $\mathbb{D}_u := \frac{s^2}{d\eta_0(x)} \mathbb{I}_d$, $\chi_a(V,N) := \frac{s^2 a(V,N)}{d} \mathbb{I}_d = a(V,N)\eta_0(x)\mathbb{D}_u$.

Therefore, the macroscopic equation for bacteria is obtained as

$$\partial_t U_0 - \nabla \cdot (\mathbb{D}_u(x) \nabla U_0) + \nabla \cdot (\chi_a(V,N)(\frac{\gamma_1}{K_N} \nabla N + \frac{\gamma_2}{K_V} \nabla V) U_0) = \mu_u(U_0, V, N) U_0. \tag{3.2.13}$$

Here, we take the growth rate as

$$\mu_u(U_0, V, N) = \alpha_u \frac{N}{K_N + N} \left( 1 - \frac{U_0}{K_U} - \frac{V}{K_V} - \frac{N}{K_N} \right),$$

where $\alpha_u > 0$ is the proliferation rate of bacteria and $K_U > 0$ is the carrying capacity for the bacteria. We consider a logistic growth slowed down by the competition for space between bacteria, normal tissue, and necrotic matter. There is also a growth enhancement factor that depends on necrotic matter for bacteria dynamics as mentioned in [79].

This macroscopic equation for bacteria dynamics is coupled with macroscopic equations describing the dynamics of mycolactone, normal tissue and necrotic matter. Hence we get the following system :

$$\begin{aligned}
\partial_t U &= \nabla \cdot (\mathbb{D}_u(x) \nabla U) - \nabla \cdot \big( \chi_a(V,N)(\frac{\gamma_1}{K_N} \nabla N + \frac{\gamma_2}{K_V} \nabla V) U \big) \\
&\quad + \alpha_u \frac{N}{K_N + N} U \left( 1 - \frac{U}{K_U} - \frac{V}{K_V} - \frac{N}{K_N} \right), \qquad t > 0,\ x \in \Omega, \\
\partial_t M &= D_m \Delta M + \delta \frac{U}{K_U + U} - \lambda M, \qquad t > 0,\ x \in \Omega, \\
\partial_t V &= -\beta_1 V \frac{M}{K_M}, \qquad t > 0,\ x \in \Omega, \\
\partial_t N &= \beta_2 \frac{V}{K_V} \frac{M}{K_M} - \gamma N, \qquad t > 0,\ x \in \Omega,
\end{aligned} \tag{3.2.14}$$

where $D_m,\ \delta,\ K_M,\ \lambda,\ \beta_1,\ \beta_2,\ \gamma$ are positive constants.

The evolution of mycolactone is governed by the second equation in the system (3.2.14), where diffusion serves as the primary mechanism driving its spread. Bacteria release mycolactone, which diffuses into wounds and surrounding tissues, causing necrosis. Over time, mycolactone degrades, altering its concentration profile.

The third equation in (3.2.14) describes the dynamics of normal tissue, capturing its necrotisation by the action of mycolactone on it. The fourth equation focuses on necrotic tissue, featuring its natural decay and the ongoing necrotisation of adjacent healthy tissue.

The boundary conditions on $(0,T)\times\partial\Omega$ are of no-flux type

$$\left(\mathbb{D}_u(x)\nabla U+\chi_a(V,N)(\frac{\gamma_1}{K_N}\nabla N+\frac{\gamma_2}{K_V}\nabla V)U\right)\cdot\nu=0,\quad \nabla M\cdot\nu=0 \tag{3.2.15}$$

and for the initial conditions we take

$$U(0,x)=u_0,\ V(0,x)=v_0,\ N(0,x)=n_0,\ M(0,x)=m_0,\ x\in\Omega. \tag{3.2.16}$$

## 3.3 Mathematical analysis

#### 3.3.0.1 Nondimensionalisation

Before performing the analysis, we nondimensionalise our system (3.2.14). Therefore, we take

$$\tilde{u}=\frac{U}{K_U},\ \tilde{v}=\frac{V}{K_V},\ \tilde{n}=\frac{N}{K_N},\ \tilde{m}=\frac{M}{K_M},\ \tilde{x}=x\sqrt{\frac{\alpha_u}{D_m}},\ \tilde{t}=t\alpha_u, \tag{3.3.1}$$

where $K_M$ is the maximum possible level of mycolactone. By using the transformations in (3.3.1), our system (3.2.14) becomes

$$\begin{aligned}
\tilde{u}_{\tilde{t}} &= \nabla\cdot\left(\tilde{\mathbb{D}_u}\nabla\tilde{u}\right)-\nabla\cdot\left(\tilde{a}(\tilde{v},\tilde{n})\tilde{\mathbb{D}_u}\tilde{\gamma_1}\tilde{u}\nabla\tilde{n}\right)-\nabla\cdot\left(\tilde{a}(\tilde{v},\tilde{n})\tilde{\mathbb{D}_u}\tilde{\gamma_2}\tilde{u}\nabla\tilde{v}\right)\\
&\quad+\frac{\tilde{n}}{1+\tilde{n}}\tilde{u}\,(1-\tilde{u}-\tilde{v}-\tilde{n})\\
\tilde{m}_{\tilde{t}} &= \Delta\tilde{m}+\frac{\tilde{\delta}\tilde{u}}{1+\tilde{u}}-\tilde{\lambda}\tilde{m}\\
\tilde{v}_{\tilde{t}} &= -\tilde{\beta}_1\tilde{m}\tilde{v}\\
\tilde{n}_{\tilde{t}} &= \tilde{\beta}_2\tilde{m}\tilde{v}-\tilde{\gamma}\tilde{n},
\end{aligned} \tag{3.3.2}$$

where

$$\widetilde{\mathbb{D}_u}=\frac{\mathbb{D}_u}{D_m},\qquad \tilde{\gamma_1}=\gamma_1\eta_0,\qquad \tilde{\gamma_2}=\gamma_2\eta_0,\qquad \tilde{\delta}=\frac{\delta}{K_M\alpha_u},\qquad \tilde{\beta}_1=\frac{\beta_1}{\alpha_u},$$
$$\tilde{\beta}_2=\frac{\beta_2}{K_N\alpha_u},\qquad \tilde{\lambda}=\frac{\lambda}{\alpha_u}\qquad \tilde{\gamma}=\frac{\gamma}{\alpha_u},\qquad \tilde{a}(\tilde{v},\tilde{n})=\frac{1}{(1+\tilde{n}+\tilde{v})^2}$$

To simplify the notation we omit all tildes in system (3.3.2) and continue with this system along with the initial conditions (3.2.16) and boundary conditions (3.2.15).

**Assumption: (A1)** Let $\mathbb{D}_u(x) \in \left(C^{2,\rho}(\Omega) \cap C(\bar{\Omega})\right)^{d\times d}$, where $\rho \in (0,1)$ and observe that there exists $\Lambda > 0$ such that for any $\xi \in \mathbb{R}^d$ and $x \in \Omega$;

$$\xi^t \mathbb{D}_u(x)\xi \geqslant \Lambda|\xi|^2$$

is satisfied.

### 3.3.1 Local existence of a solution

The following result establishes the local existence of solutions to (3.3.2). The proof is similar to that of in [95].

**Lemma 3.3.1.** *Let $\Omega \subset \mathbb{R}^d$ $(d \geqslant 1)$ be a bounded domain with a smooth boundary. Suppose that $u_0 \in W^{1,\infty}(\Omega)$, $m_0$, $n_0$, $v_0 \in W^{2,\infty}(\Omega)$ satisfying compatibility conditions on boundary and are non negative. Let **(A1)** be satisfied. Then there exists a quadruple of non-negative functions $(u,m,v,n) \in C^0([0,T_{\max}) \times \bar{\Omega}) \cap C^{2,1}((0,T_{\max}) \times \Omega)$ which solve system (3.3.2) classically in $(0,T_{\max}) \times \Omega$. Moreover, we have the following dichotomy*

$$\begin{aligned} &\text{either } T_{max} = \infty \text{ or} \\ &\limsup_{t \nearrow T_{\max}} (||u(t)||_{L^\infty(\Omega)} + ||m(t)||_{W^{1,\infty}(\Omega)} + ||v(t)||_{W^{1,\infty}(\Omega)} + ||n(t)||_{W^{1,\infty}(\Omega)}) = \infty. \end{aligned} \tag{3.3.3}$$

*Proof.* We define the following closed, bounded, and convex set

$$Q := \{\bar{u} \in L^\infty((0,T) \times \Omega) : 0 \leqslant \bar{u} \leqslant ||u_0||_{L^\infty(\Omega)} + 1 \text{ a.e in } \Omega \times (0,T)\}$$

with $T > 0$ small, to be fixed below. We consider a fixed point problem with the operator $F$ defined on $Q$ such that $F(\bar{u}) = u$, where $u$ is the first component of the solution $(u,m,v,n)$ to the following system for $x \in \Omega,\ t \in (0,T)$:

$$\begin{aligned} u_t &= \nabla \cdot (\mathbb{D}_u \nabla u) - \nabla \cdot (a(v,n)\mathbb{D}_u \gamma_1 u \nabla n) - \nabla \cdot (a(v,n)\mathbb{D}_u \gamma_2 u \nabla v) \\ &\quad + \frac{n}{1+n} u\,(1-u-v-n) \\ \partial_t m &= \Delta m + \delta \frac{\tilde{u}}{1+\tilde{u}} - \lambda m \\ \partial_t v &= -\beta_1 v m \\ \partial_t n &= \beta_2 v m - \gamma n \\ \left(\mathbb{D}_u \nabla u - a(v,n)\mathbb{D}_u u(\gamma_1 \nabla n + \gamma_2 \nabla v)\right) \cdot \vartheta &= 0, \quad \nabla m \cdot \vartheta = 0 \quad x \in \partial\Omega,\ t > 0 \\ u(0,x) = u_0(x),\ m(0,x) &= m_0(x),\ v(0,x) = v_0(x),\ n(0,x) = n_0(x), \quad x \in \Omega. \end{aligned} \tag{3.3.4}$$

For any $q > \frac{d+2}{2}$, by using Theorem A.1 in [39], there exists a solution $m(t,x)$ such that

$$||\nabla m||_{L^q((0,T)\times\Omega)} \leqslant \tilde{c_1}, \tag{3.3.5}$$

where $\tilde{c_1}$ is a positive constant which depends on $||u_0||_{L^\infty(\Omega)}, ||m_0||_{W^{1,\infty}(\Omega)}, ||n_0||_{W^{1,\infty}(\Omega)}$ and $||v_0||_{W^{1,\infty}(\Omega)}$. The following constants $\tilde{c_2}, c_3, c_4, c_5, ..$ also depend on the above values.

By solving the ODE for $v$ we get

$$v(t,x) = v_0(x) \exp\left(-\beta_1 \int_0^t m(s,x)ds\right), \qquad t \in (0,T),\ x \in \Omega. \tag{3.3.6}$$

From (3.3.5) and (3.3.6), we get

$$||\nabla v||_{L^q((0,T)\times\Omega)} \leqslant \tilde{c_2}. \tag{3.3.7}$$

Using the variation of constants formula on the fourth equation of system (3.3.2) , we obtain the following representation:

$$n(t,x) = e^{-\gamma t} n_0(x) + \beta_2 \int_0^t m(s,x)v(s,x)e^{-\gamma(t-s)}ds, \qquad t \in (0,T),\ x \in \Omega. \tag{3.3.8}$$

Using the previous estimates (3.3.5) and (3.3.7) we have

$$||\nabla n||_{L^q((0,T)\times\Omega)} \leqslant c_3. \tag{3.3.9}$$

Hence, we can rewrite the first equation in system (3.3.2) as

$$\partial_t u = \nabla \cdot (\mathbb{D}_u(x)\nabla u - g(t,x)u) + \frac{n}{n+1} u\,(1 - \tilde{u} - v - n)$$

where $||g||_{L^q((0,T)\times\Omega)} \leqslant c_4$. Using the parabolic theory(Thm V.2.1 and V.1.1 from [57]), $||u||_{L^\infty((0,T)\times\Omega)} \leqslant c_5$ and we get $c_6$ such that $||u||_{C^{\beta,\frac{\beta}{2}}((0,T)\times\Omega)} \leqslant c_6$ for some $\beta > 0$. Hence $||u||_{L^\infty((0,T)\times\Omega)} \leqslant ||u_0||_{L^\infty(\Omega)} + c_7 T^{\frac{\beta}{2}}$ for some $T < 1$ such that $c_7 T^{\frac{\beta}{2}} < 1$.

Now, consider the fixed point problem $F(\bar{u}) = u$. By using the above, we have $F(Q) \subset Q$. Since $F$ is continuous and $\overline{F(Q)}$ is a compact subset in $L^\infty((0,T)\times\Omega)$, by applying Schauders's fixed point theorem we have that there exists at least one fixed point $u \in Q$. Hence by parabolic regularity theory $(u,v,n,m)$ is obtained as the classical solution of system (3.3.2) in $C^0([0,T)\times\bar{\Omega}) \cap C^{2,1}((0,T)\times\Omega)$.

Define

$$A := ||u(0)||_{L^\infty(\Omega)} + ||m(0)||_{W^{1,\infty}(\Omega)} + ||v(0)||_{W^{1,\infty}(\Omega)} + ||n(0)||_{W^{1,\infty}(\Omega)}. \tag{3.3.10}$$

and let
$T_{max} = \sup\{T \in (0,\infty] \ :$ there exists a solution in $C^0([0,T_{max})\times\bar{\Omega})) \cap C^{2,1}((0,T_{\max})\times\Omega)\}$, be the maximum existence time. Let $T_{max} < \infty$ and

$$\limsup_{t \nearrow T_{\max}} (||u(t)||_{L^\infty(\Omega)} + ||m(t)||_{W^{1,\infty}(\Omega)} + ||v(t)||_{W^{1,\infty}(\Omega)} + ||n(t)||_{W^{1,\infty}(\Omega)}) < \infty.$$

Hence there exists $A' > 0$ such that

$$||u(t)||_{L^\infty(\Omega)} + ||m(t)||_{W^{1,\infty}(\Omega)} + ||v(t)||_{W^{1,\infty}(\Omega)} + ||n(t)||_{W^{1,\infty}(\Omega)} < A' \quad \text{for all } t < T_{max}.$$

Next we choose $T_1$ sufficiently small such that the above procedure works in $[0, T_1]$ after replacing $A$ (defined in (3.3.10)) by $A'$. Define $T_2 = T_{max} - \frac{T_1}{2}$. As $T_1$ depends only on $A'$, we may choose $u(T_2, .), m(T_2, .), v(T_2, .), n(T_2, .)$ as new initial values. Hence by the above procedure, we obtain a solution in $[T_2, T_{max} + \frac{T_1}{2}]$. This contradicts the maximality of $T_{max}$. Hence (3.3.3) holds. By applying the maximum principle in [86], we get the non-negativity of $u$. Using Theorem A.3 in [59]) to the PDE of $m$ in (3.3.2) we get the non-negativity of $m$. By using the non-negativity of $m$, the assumption on $v_0$, and from (3.3.6) the non-negativity of $v$ is obtained. By using the positivity of $\gamma$, assumption on $n_0$, (3.3.8) and by the non-negativity of $m$ and $v$ we get the nonnegativity of $n$.

□

### 3.3.2 Boundedness of the solution components

To prove the global existence of solutions we will begin by proving the boundedness of functions $u$, $m$, $v$, and $n$ satisfying (3.3.2), (3.2.16), and (3.2.15). We follow the proof in [55].

**Remark 3.3.1.** *The boundedness of the solution components is independent of the local existence of the solution. However, for convenience, the same maximal time $T_{max}$ from the local existence proof is often used in the boundedness proof. This allows for consistency in the analysis while treating the existence and boundedness as separate properties.*

**Lemma 3.3.2.** *There exists $C_m > 0$ such that*

$$\begin{aligned} ||m||_{L^\infty([0,T_{\max})\times\Omega)} &\leqslant ||m_0||_{L^\infty(\Omega)} + \frac{\delta}{\lambda} \\ ||\nabla m||_{L^\infty([0,T_{\max})\times\Omega)} &\leqslant C_m(||\nabla m_0||_{L^\infty(\Omega)} + 1), \end{aligned}$$

*Proof.* Let $pm^{p-1}$ be a test function for the $m$-equation of system (3.3.2) for $p > 1$. Integrating over $\Omega$, we have for any $\epsilon \in (0, 1)$

$$\begin{aligned} \frac{d}{dt}\int_\Omega m^p &= -p(p-1)\int_\Omega m^{p-2}|\nabla m|^2 + p\delta\int_\Omega m^{p-1}\frac{u}{1+u} - \lambda p\int_\Omega m^p \\ &= -\frac{4(p-1)}{p}\int_\Omega |\nabla m^{p/2}|^2 + p\delta\int_\Omega m^{p-1}\frac{u}{1+u} - \lambda p\int_\Omega m^p \\ &\leqslant -\frac{4(p-1)}{p}\int_\Omega |\nabla m^{p/2}|^2 + p\delta\int_\Omega |m|^{p-1} - \epsilon\lambda p\int_\Omega m^p. \end{aligned}$$

For some $A > 0$ and $\psi \in (0, 1)$, we have

$$\begin{aligned} p\delta\int_\Omega |m|^{p-1} &= p\delta\int_{\{x\in\Omega\,:\,|m(x)|\leqslant A\}} |m|^{p-1} + p\delta\int_{\{x\in\Omega\,:\,|m(x)|>A\}} |m|^{p-1} \\ &\leqslant p\delta A^{p-1}|\Omega| + p\delta\psi\int_\Omega |m|^{p-1}. \end{aligned}$$

If we choose $A := \frac{\delta(1-\psi)^{\frac{1}{p-1}}}{\lambda(1-\epsilon)}$, then we get

$$\frac{d}{dt}\int_\Omega m^p + \epsilon\lambda p\int_\Omega m^p \leqslant \frac{p\delta^p|\Omega|}{(1-\epsilon)^{p-1}\lambda^{p-1}}. \tag{3.3.11}$$

Multiplying both sides of (3.3.11) with $e^{\epsilon\lambda pt}$ and integrating both sides from 0 to $t$ for any $t \in [0, T_{\max})$, we obtain

$$\int_\Omega m^p \leqslant \int_\Omega m_0^p + \frac{\delta^p |\Omega|}{\epsilon\lambda^p (1-\epsilon)^{p-1}}.$$

Additionally,

$$\begin{aligned}
||m(t)||_{L^\infty(\Omega)} &= \lim_{p\to\infty} \left( \int_\Omega m^p(t) \right)^{\frac{1}{p}} \\
&\leqslant \lim_{p\to\infty} \left( \int_\Omega m_0^p + \frac{\delta^p |\Omega|}{\epsilon\lambda^p (1-\epsilon)^{p-1}} \right)^{\frac{1}{p}} \\
&\leqslant ||m_0||_{L^\infty(\Omega)} + \lim_{p\to\infty} \frac{\delta |\Omega|^{\frac{1}{p}}}{\lambda \epsilon^{\frac{1}{p}} (1-\epsilon)^{\frac{p-1}{p}}}. \\
&\leqslant ||m_0||_{L^\infty(\Omega)} + \frac{\delta}{\lambda}.
\end{aligned}$$

Because of the arbitrariness of $\epsilon \in (0,1)$, we get the desired result. By using the second equation of system (3.3.2), we have for all $t \in (0, T_{\max})$

$$m(t) = e^{t\Delta} m_0 + \int_0^t e^{(t-s)\Delta} \big( \delta \frac{u}{1+u} - \lambda m \big) ds,$$

where $e^{t\Delta}$ denotes the Neumann heat semigroup. By using the above estimate along with Lemma 1.3 (ii) and 1.3 (iii) from [101], we obtain for all $t \in (0, T_{max})$

$$\begin{aligned}
||\nabla m(t)||_{L^\infty(\Omega)} &\leqslant ||\nabla e^{t\Delta} m_0||_{L^\infty(\Omega)} + \int_0^t ||\nabla e^{(t-s)\Delta} \big( \frac{\delta u}{1+u} - \lambda m \big)||_{L^\infty(\Omega)} ds \\
&\leqslant k_1 e^{-\lambda_1 t} ||\nabla m_0||_{L^\infty(\Omega)} + k_2 \int_0^t e^{-\lambda_1 (t-s)} (1 + (t-s)^{\frac{-1}{2}}) || \frac{\delta u}{1+u} - \lambda m ||_{L^\infty(\Omega)} ds \\
&\leqslant k_1 e^{-\lambda_1 t} ||\nabla m_0||_{L^\infty(\Omega)} + k_2 \int_0^t e^{-\lambda_1 (t-s)} (1 + (t-s)^{\frac{-1}{2}}) (\delta + \lambda ||m||_{L^\infty(\Omega)}) ds \\
&\leqslant C_m (||\nabla m_0||_{L^\infty(\Omega)} + 1),
\end{aligned}$$

where $\lambda_1 > 0$ denotes the first non-zero eigenvalue of $-\Delta$ in $\Omega \subset \mathbb{R}^d$ under Neumann boundary conditions.

□

**Remark 3.3.2.** *By using* (3.3.6)*, non negativity of* $m$*, the assumption on* $v_0$ *and Lemma 3.3.1, we can conclude that there exist constants* $C_1, c_1 > 0$ *such that* $||v||_{L^\infty([0,T_{\max})\times\Omega)} \leqslant C_1$*. By using* (3.3.6) *and Lemma 3.3.2, we also get*

$$||\nabla v||_{L^\infty([0,T_{\max})\times\Omega)} \leqslant c_1.$$

**Remark 3.3.3.** *By using* (3.3.8)*, the positivity of* $\gamma$*, the assumption on* $n_0$*, Lemma 3.3.2, and Remark 3.3.2, there exist constants* $C_2, c_2 > 0$ *such that* $||n||_{L^\infty([0,T_{\max})\times\Omega)} \leqslant C_2$*. Using* (3.3.8)*, Lemma 3.3.2, and Remark 3.3.2, we also get*

$$||\nabla n||_{L^\infty([0,T_{\max})\times\Omega)} \leqslant c_2.$$

**Lemma 3.3.3.** *Let **(A1)** be satisfied. Then for any $p > 1$, there exists $C > 0$ such that for $t \in (0, T_{\max})$, we have*

$$||u(t)||_{L^p(\Omega)} \leqslant C.$$

*Proof.* Let $pu^{p-1}$ be a test function for the first equation of system (3.3.2). Then integrating over $\Omega$, using the no flux boundary conditions of the system and Young's inequality, and denoting $||\mathbb{D}_u||_{L^\infty(\Omega)} := D_0$, we have

$$\begin{aligned}
\frac{d}{dt}\int_\Omega u^p =& -\frac{4(p-1)}{p}\int_\Omega (\nabla u^{\frac{p}{2}})^\top \mathbb{D}_u(x)\nabla u^{\frac{p}{2}} + (p-1)\int_\Omega (\nabla u^p)^\top a(v,n)\mathbb{D}_u(x)(\gamma_1\nabla n + \gamma_2\nabla v)\\
&+ \int_\Omega p\frac{n}{n+1}u^p(1-u-v-n)\\
\leqslant& -\frac{4(p-1)\Lambda}{p}\int_\Omega |\nabla u^{\frac{p}{2}}|^2 + \frac{4(p-1)\Lambda}{p}\int_\Omega |\nabla u^{\frac{p}{2}}|^2 + \tilde{C}\int_\Omega u^p + p\int_\Omega u^p,\\
\leqslant& (\tilde{C}+p)\int_\Omega u^p,
\end{aligned}$$

where

$$\tilde{C} = \frac{(p-1)p}{4\Lambda}D_0^2(\gamma_1||\nabla n||_{L^\infty} + \gamma_2||\nabla v||_{L^\infty})^2,$$

By Gronwall's inequality, we obtain

$$\int_\Omega u^p \leqslant \exp(t(\tilde{C}+p))\int_\Omega u_0^p.$$

Thus, we get the desired result

$$||u(t)||_{L^p(\Omega)} \leqslant C(p, T_{max}, ||u_0||_{L^p(\Omega)}). \tag{3.3.12}$$

□

**Remark 3.3.4.** *By the usual Moser iteration process as in [62], we can prove that there exists $\tilde{C}_1(T_{max}) > 0$ such that*

$$||u(t)||_{L^\infty(\Omega)} \leqslant \tilde{C}_1 \quad \text{for all } t \in (0, T_{max})$$

**Theorem 3.3.1.** *Under the assumptions of Lemma 3.3.1, system* (3.3.2) *has a non-negative classical solution $(u, v, n, m)$ which is global in time.*

*Proof.* This is now an immediate consequence of the previous results. □

## 3.4 Numerical simulations

In this section, the macroscopic model (3.3.2) of Buruli ulcer is numerically simulated. The finite difference method (FDM) is used to discretise the model. The diffusion terms are discretised by using the standard central difference scheme. For the taxis terms a first-order upwind discretisation is used. For the time derivatives an implicit-explicit (IMEX) scheme is used, thereby treating the diffusion parts implicitly and discretising the taxis

and source terms with an explicit Euler method.

In order to conduct simulations of the model, a set of realistic parameters was required. To establish an estimated range for these parameters, we consulted several relevant studies in the literature [3, 14, 53, 60, 64, 88–90]. The simulations are performed obtaining the non dimensionalised parameters using the following dimensional parameter set:

| | | |
|---|---|---|
| $D_u$ | $10^{-4}\ mm^2/h$ | [60] |
| $D_m$ | $0.086\ mm^2/h$ | [3] |
| $\delta$ | $1/h$ | [3] |
| $\lambda$ | $0.1/h$ | [3] |
| $\beta_1$ | $0.3/h$ | [53, 64, 90], This work |
| $\beta_2$ | $0.3/h$ | [53, 64, 90], This work |
| $\gamma$ | $3 * 10^{-4}/h$ | This work |
| $\alpha_u$ | $.005/h$ | [88], This work |
| $\gamma_1$ | $10^{-5} - 10^{-3}h$ | This work |
| $\gamma_2$ | $10^{-5} - 10^{-3}h$ | This work |
| $\gamma_3$ | $10^{-4}h$ | This work |
| $\eta_0$ | $10/h$ | This work |
| $K_U$ | $10^4\ cells\ mm^{-2}$ | [88], This work |
| $K_M$ | $10^4\ mol/L$ | This work |
| $K_V$ | $10^4\ cells\ mm^{-2}$ | This work |
| $K_N$ | $10^4\ cells\ mm^{-2}$ | This work |

A variety of scenarios is considered, where $\gamma_1$ and $\gamma_2$ take different values. Furthermore, we simulate a model in which bacteria perform chemotaxis towards mycolactone, as well as another model in which the initial condition of normal tissue is lower.

**Scenario 1:** $\gamma_1 = \gamma_2 = 10^{-5}h$

**Scenario 2:** $\gamma_1 = 10^{-3}h > \gamma_2 = 10^{-5}h$

**Scenario 3:** $\gamma_1 = 10^{-5}h < \gamma_2 = 10^{-3}h$

**Scenario 4:** Bacteria additionally perform a linear chemotaxis towards mycolactone. We consider the macroscopic equation of bacteria as

$$\partial_t u = \nabla \cdot (\mathbb{D}_u(x)\nabla u) - \nabla \cdot (a(v,n)u(\gamma_1 \nabla n + \gamma_2 \nabla v)) - \nabla \cdot (\gamma_3 u \nabla m) + \frac{n}{n+1} u\,(1-u-v-n)$$

where $\gamma_3 = 10^{-4} mm^2/h$.

We consider the non-dimensionalised initial conditions as

$$\begin{aligned} u(0,x,y) &= 0.95\exp(-\frac{(x-0.5)^2+(y-0.5)^2}{.01}), \qquad x,y\in[0,1],\\ m(0,x,y) &= 0.001\exp(-\frac{(x-0.5)^2+(y-0.5)^2}{.01}), \qquad x,y\in[0,1],\\ v(0,x,y) &= \mathcal{U},\\ n(0,x,y) &= 0.0001\exp(-\frac{(x-0.5)^2+(y-0.5)^2}{.01}), \qquad x,y\in[0,1], \end{aligned} \tag{3.4.1}$$

where $\mathcal{U}$ is uniformly distributed in $(0,1)$. They are illustrated in Figure 3.1.

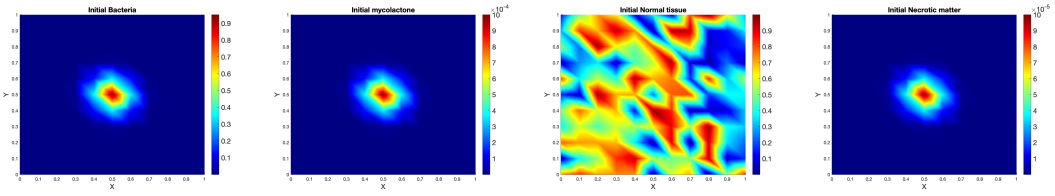


(a) Bacteria (b) Mycolactone (c) Normal tissue (d) Necrotic matter

Figure 3.1: Initial conditions for bacteria, mycolactone, normal tissue, and necrotic matter.

Also we apply the no-flux boundary conditions in (3.2.15) on the boundary of $\Omega = (0,1)\times(0,1)$. According to the initial conditions, the space is predominantly occupied with normal tissue and bacteria are provided at the centre of the domain (assumed site of insect bite), from where they spread into the tissue. As a consequence, toxin and necrotic matter are initially rather concentrated as well.

In Figure 3.2, we observe the dynamics of bacteria, mycolactone, normal tissue, and necrotic matter for Scenario 1 when $\gamma_1 = \gamma_2$. While the progression patterns are similar across all cases, they exhibit varying densities. The simulation shows an intriguing biphasic progression of the disease. Initially, over approximately 100 hours (about 4 days), there's a decrease in bacteria, mycolactone, and necrotic tissue. This early decline likely stems from a combination of factors: the initial lack of necrotic tissue to support bacterial growth, the host's immune response, and localised depletion of nutrients. Crucially, the absence of sufficient necrotic matter in early stages limits bacterial proliferation, as bacteria thrives in necrotic environments. However, after this period, all three components increase, marking a turning point in infection progression. This second phase probably represents the establishment of a favorable environment for bacteria: accumulated necrotic tissue enhances bacterial growth, increased mycolactone levels suppress the local immune response, and bacteria potentially spread to unaffected areas with fresh resources. A positive feedback loop ensues, where bacterial growth leads to more mycolactone production, causing more tissue necrosis, which further promotes bacterial proliferation. This pattern underscores the critical role of necrotic tissue in disease progression - initially as a growth-limiting factor, later as a growth-promoter. It also suggests a crucial early window for therapeutic intervention, before the infection becomes self-sustaining. The model's

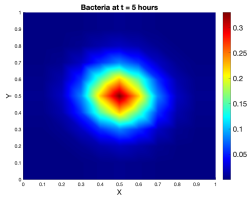


(a) Bacteria at $t = 5$

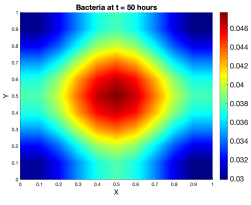


(b) Bacteria at $t = 50$

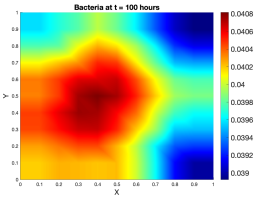


(c) Bacteria at $t = 100$

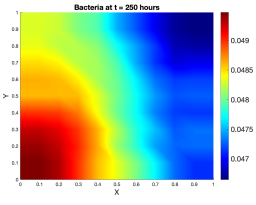


(d) Bacteria at $t = 250$

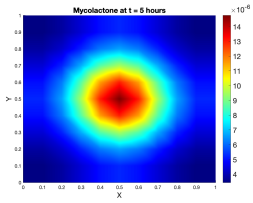


(e) Mycolactone at $t = 5$

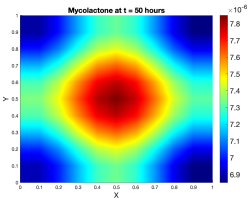


(f) Mycolactone at $t = 50$

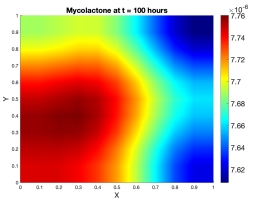


(g) Mycolactone at $t = 100$

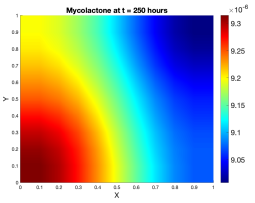


(h) Mycolactone at $t = 250$

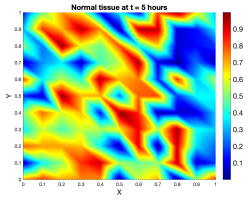


(i) Normal tissue at $t = 5$

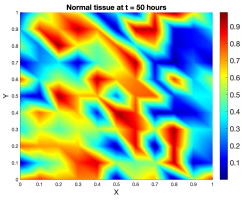


(j) Normal tissue at $t = 50$

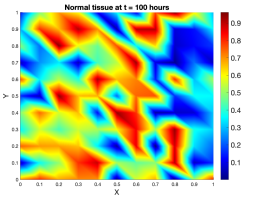


(k) Normal tissue at $t = 100$

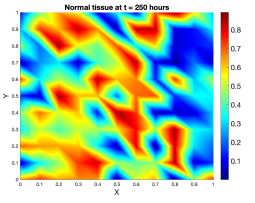


(l) Normal tissue at $t = 250$

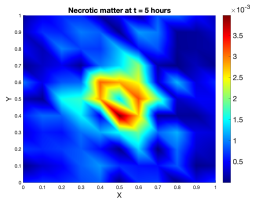


(m) Necrotic matter at $t = 5$

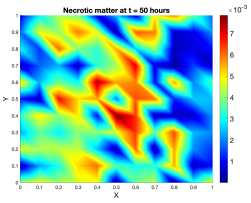


(n) Necrotic matter at $t = 50$

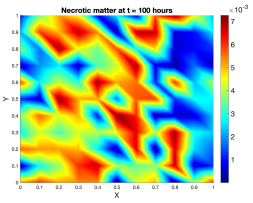


(o) Necrotic matter at $t = 100$

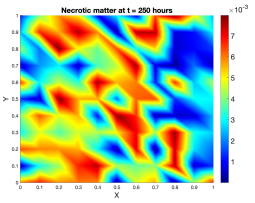


(p) Necrotic matter at $t = 250$

Figure 3.2: Scenario 1: Bacteria, mycolactone, normal tissue, and necrotic matter at different times for $\gamma_1 = \gamma_2$.

insights highlight potential treatment strategies, including preventing tissue necrosis, inhibiting mycolactone production, and emphasising early-stage treatments to disrupt the establishment of a expanding infection.

We add the comparison of Scenario 2 to Scenario 3 in Figure 3.3, and Scenario 1 to Scenario 4 in Figure 3.4 in order to identify significant differences in the dynamics of each solution component.

When comparing Scenario 2 ($\gamma_1 > \gamma_2$) and Scenario 3 ($\gamma_2 > \gamma_1$) (i.e., Scenario 3- Scenario 2), the bacterial density difference is rather small at early times. The absolute difference gets larger with advancing time. This is the case for all solution components, however for some of them (normal tissue, necrotic matter and bacteria) being more substantial within the simulated time span. Consequently, necrotisation is stronger and faster when $\gamma_2 > \gamma_1$: the cells follow existing tissue rather than necrotic matter, which is slowly built.

When comparing Scenario 1 (without chemotaxis) to Scenario 4 (with chemotaxis towards mycolactone) in fact we perform Scenario 4 - Scenario 1, several key differences emerge in the dynamics of bacterial proliferation, mycolactone concentration, normal tissue, and necrotic matter. The bacterial density difference increases from $t = 5$ to $t = 50$, decreases slightly between $t = 50$ and $t = 100$, and then rises again by $t = 250$, suggesting a fluctuating but overall enhanced bacterial proliferation in Scenario 4. This is driven by chemotaxis, where bacteria actively migrate towards regions with higher mycolactone concentrations, thus amplifying their spread. Mycolactone and necrotic matter differences exhibit a similar behaviour. Tissue degradation is more localised around areas with high bacterial concentrations. Notably, there are negative differences in normal tissue density where bacterial concentrations are higher, indicating that in Scenario 4, necrotisation is more severe in regions of bacterial accumulation, or at least there are some higher cell aggregates - probably due to the cells being attracted to the sites with higher mycolactone concentration. Bacteria accumulates in areas with high toxin concentration and express even more mycolactone which in turn leads to enhanced tissue degradation. Overall, however, the differences are so small, that one could give up chemotaxis towards mycolactone, in order to not complicate unncecessarily the model.

We also consider a special **Scenario 5**, where the initial density of normal tissue is much lower. Here we take $\gamma_1$ and $\gamma_2$ equal. The initial conditions in this scenario are given as follows:

$$\begin{aligned} u(0,x,y) &= 0.95\exp(-\frac{(x-0.5)^2+(y-0.5)^2}{.01}), \qquad x,y\in[0,1],\\ m(0,x,y) &= 0.001\exp(-\frac{(x-0.5)^2+(y-0.5)^2}{.01}), \qquad x,y\in[0,1],\\ v(0,x,y) &= 0.0001*\mathcal{U},\\ n(0,x,y) &= 0.0001\exp(-\frac{(x-0.5)^2+(y-0.5)^2}{.01}), \quad x,y\in[0,1], \end{aligned} \tag{3.4.2}$$

where $\mathcal{U}$ represents a uniform distribution in $(0,1)$. They are illustrated in Figure 3.5.

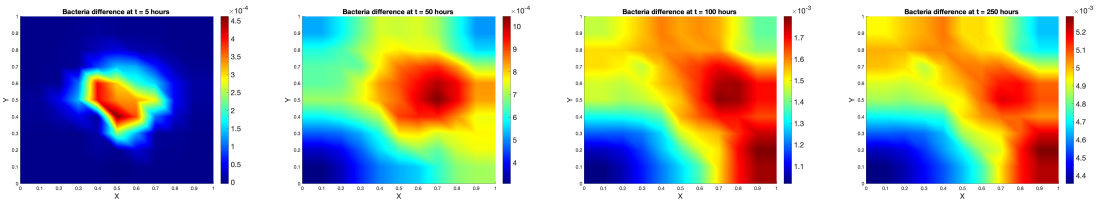


(a) Bacteria at $t = 5$ (b) Bacteria at $t = 50$ (c) Bacteria at $t = 100$ (d) Bacteria at $t = 250$

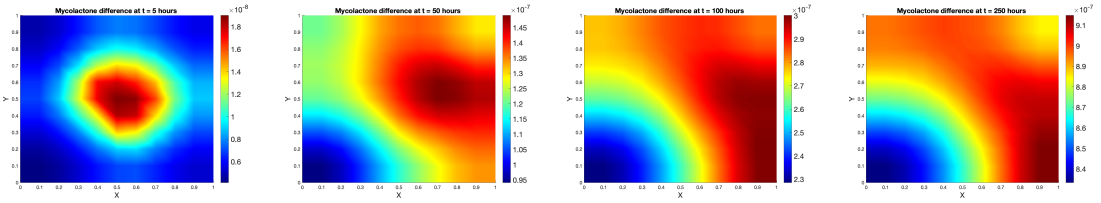


(e) Mycolactone at $t = 5$ (f) Mycolactone at $t = 50$ (g) Mycolactone at $t = 100$ (h) Mycolactone at $t = 250$

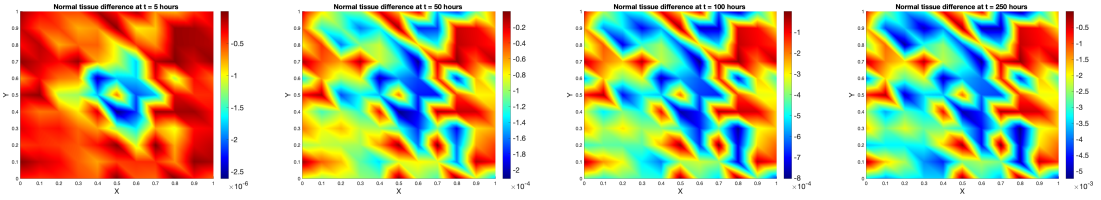


(i) Normal tissue at $t = 5$ (j) Normal tissue at $t = 50$ (k) Normal tissue at $t = 100$ (l) Normal tissue at $t = 250$

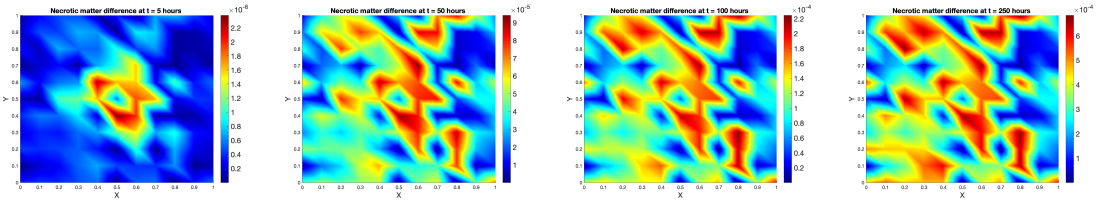


(m) Necrotic matter at $t = 5$ (n) Necrotic matter at $t = 50$ (o) Necrotic matter at $t = 100$ (p) Necrotic matter at $t = 250$

Figure 3.3: Difference between densities of bacteria, mycolactone, normal tissue, and necrotic matter at different times for Scenario 2 and Scenario 3 (Scenario 3 - Scenario 2).

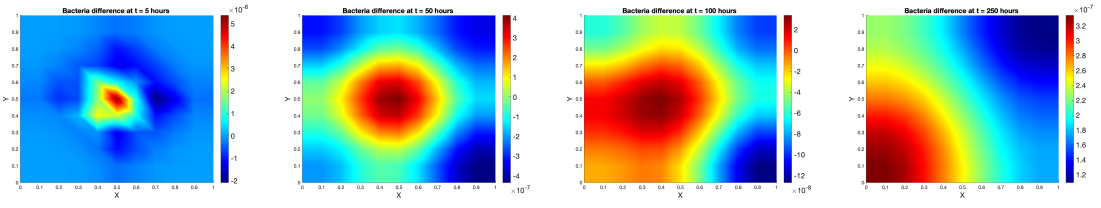


(a) Bacteria at $t = 5$ (b) Bacteria at $t = 50$ (c) Bacteria at $t = 100$ (d) Bacteria at $t = 250$

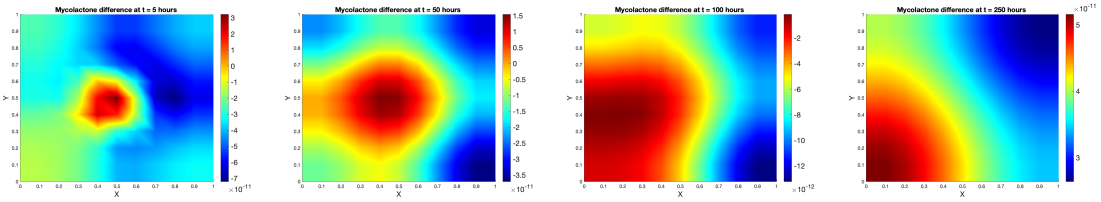


(e) Mycolactone at $t = 5$ (f) Mycolactone at $t = 50$ (g) Mycolactone at $t = 100$ (h) Mycolactone at $t = 250$

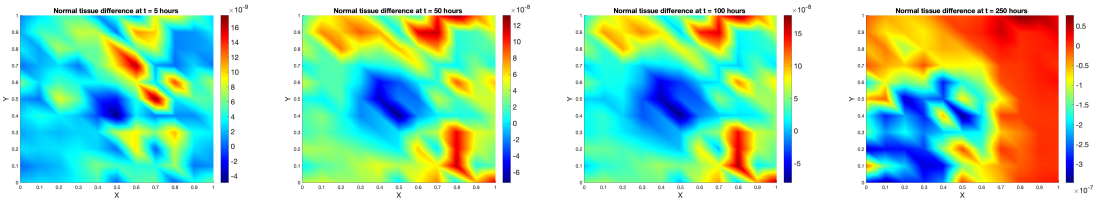


(i) Normal tissue at $t = 5$ (j) Normal tissue at $t = 50$ (k) Normal tissue at $t = 100$ (l) Normal tissue at $t = 250$

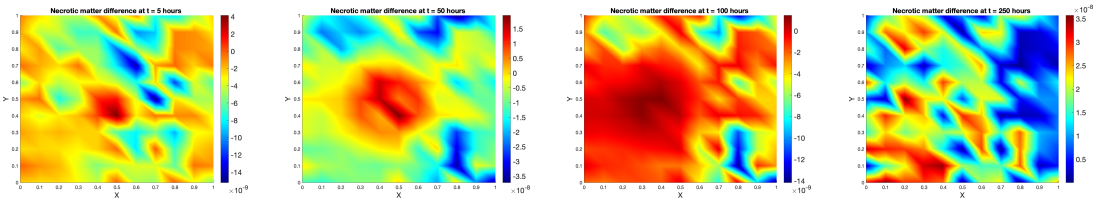


(m) Necrotic matter at $t = 5$ (n) Necrotic matter at $t = 50$ (o) Necrotic matter at $t = 100$ (p) Necrotic matter at $t = 250$

Figure 3.4: Difference between densities of bacteria, mycolactone, normal tissue, and necrotic matter at different times for Scenario 4 and Scenario 1 (Scenario 4 - Scenario 1).

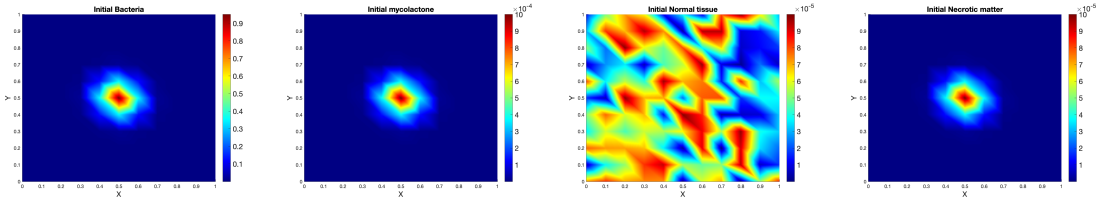


(a) Bacteria (b) Mycolactone (c) Normal tissue (d) Necrotic matter

Figure 3.5: Initial conditions for bacteria, mycolactone, normal tissue, and necrotic matter in Scenario 5

In contrast to Scenarios 1-4, where ample normal tissue fosters bacterial proliferation, an intriguing pattern emerges when initial normal tissue levels are insufficient. Instead of growth, bacteria undergo degradation over time, accompanied by increased diffusion. This decline in bacteria shows the importance of sufficiently available normal tissue at the beginning of the process. In Scenario 5 where normal tissue is lacking, bacterial proliferation is hindered, leading to a gradual reduction in bacterial density over time. While proliferation is subdued for bacteria, diffusion becomes pronounced due to the absence of adequate normal tissue or necrotic matter to stimulate taxis.

The diminished population of bacteria results in a corresponding decrease in mycolactone levels. Nevertheless, the ongoing necrotisation of normal tissue continues unchanged over time but rather at a slower pace compared to scenarios with sufficient initial tissue levels. This observation highlights the close interrelation between dynamics of bacteria, normal tissue, and mycolactone production.

We also provide the comparison of Scenario 1 to Scenario 5 in Figure 3.8. The difference in the initial density of normal tissue is given in Figure 3.7.

In the comparison between Scenario 5 and Scenario 1, all entities (bacteria, mycolactone, normal tissue, and necrotic tissue) exhibit positive differences in regions of higher concentrations. This results from starting with a lower initial amount of normal tissue in Scenario 5, leading to reduced growth of all other entities compared to Scenario 1, which begins with an adequate amount of normal tissue. This highlights the significant impact of initial conditions on the progression and dynamics of bacterial infection and tissue response.

From the scenarios discussed above, it becomes evident that the taxis rate of bacteria towards normal tissue, along with the initial density of normal tissue, significantly influences the progression of bacterial colonisation and the development of Buruli ulcer. When the taxis rate of bacteria towards normal tissue is lower (as in the case of $\gamma_1 > \gamma_2$), the production and spread of bacteria, as well as other associated entities, are diminished compared to scenarios where the taxis rate $\gamma_2$ is higher. This difference underscores the pivotal role of bacterial motility in dictating the extent of bacterial colonisation and subsequent tissue damage.

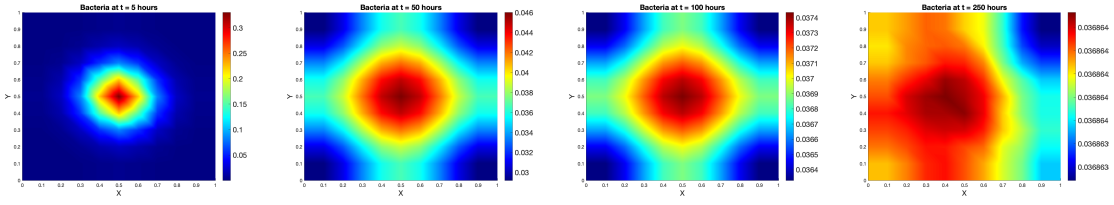


(a) Bacteria at $t = 5$ (b) Bacteria at $t = 50$ (c) Bacteria at $t = 100$ (d) Bacteria at $t = 250$

(e) Mycolactone at $t = 5$ (f) Mycolactone at $t = 50$ (g) Mycolactone at $t = 100$ (h) Mycolactone at $t = 250$

(i) Normal tissue at $t = 5$ (j) Normal tissue at $t = 50$ (k) Normal tissue at $t = 100$ (l) Normal tissue at $t = 250$

(m) Necrotic matter at $t = 5$ (n) Necrotic matter at $t = 50$ (o) Necrotic matter at $t = 100$ (p) Necrotic matter at $t = 250$

Figure 3.6: Scenario 5: Bacteria, mycolactone, normal tissue, and necrotic matter at different times for a lower initial density for normal tissue.

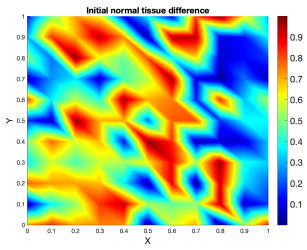


Figure 3.7: Difference between the initial conditions for normal tissue, in Scenarios 1 and 5.

Similarly, a lower initial density of normal tissue leads to a distinct outcome: bacterial degradation over time rather than proliferation. This observation highlights the critical importance of a smaller quantity of normal tissue in slowing bacterial growth and tissue degradation.

Considering the body's natural ability to produce normal tissue, it is conceivable that in scenarios with lower initial normal tissue density, the body's regenerative capacity may contribute to the replenishment of normal tissue rather than its necrotisation. This suggests a potential avenue for intervention, wherein strategies aimed at making the normal tissue unfavourable e.g., by heating the affected areas could mitigate the progression of Buruli ulcer in cases of depleted initial normal tissue density.

Overall, these observations underscore the connection between bacterial dynamics, tissue health, and the body's regenerative capacity in the pathogenesis of Buruli ulcer. Further research into these mechanisms could inform the development of novel therapeutic approaches for managing this debilitating disease.

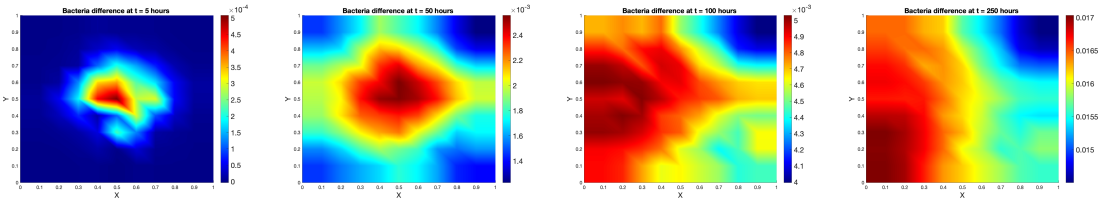


(a) Bacteria at $t = 5$ (b) Bacteria at $t = 50$ (c) Bacteria at $t = 100$ (d) Bacteria at $t = 250$

(e) Mycolactone at $t = 5$ (f) Mycolactone at $t = 50$ (g) Mycolactone at $t = 100$ (h) Mycolactone at $t = 250$

(i) Normal tissue at $t = 5$ (j) Normal tissue at $t = 50$ (k) Normal tissue at $t = 100$ (l) Normal tissue at $t = 250$

(m) Necrotic matter at $t = 5$ (n) Necrotic matter at $t = 50$ (o) Necrotic matter at $t = 100$ (p) Necrotic matter at $t = 250$

Figure 3.8: Difference between densities of bacteria, mycolactone, normal tissue, and necrotic matter at different times for Scenario 1 and Scenario 5 (Scenario 1 - Scenario 5).

Chapter 4

# Mathematical model for Buruli ulcer wound using random jump approach

## 4.1 Introduction

In this chapter, we consider the microscopic properties of Buruli ulcer progression, aiming to enhance our understanding by incorporating individual bacterial interactions and their effects on tissue dynamics. The linear diffusion model previously employed in Chapter 3 provided valuable insights into the overall dynamics of Buruli ulcer progression. However, they often lacked the details necessary to include the complex interactions occurring at the cellular level. To address this limitation, we turn our attention to modelling upon starting from a microscopic level, which allows us to delve deeper into the mechanisms governing bacterial proliferation, tissue necrosis, and mycolactone production.

An approach known as the random walk method described in [78, 91] is adopted in our quest to develop a better model. The random walk approach simulates bacterial cell movement stochastically within their environment as opposed to traditional transport equations that describe the movement of entities in a continuous medium. This approach allows for the simulation of complex biological systems by discretising space into a lattice and describing the movement and interactions of particles (representing bacteria, toxins, etc.) according to probabilistic rules. By tracking the trajectories of these cells and their interactions with surrounding tissue, we can informally derive a nonlinear reaction-diffusion-taxis equation that accounts for both diffusion and directed movement towards or away from specific targets.

When applied to the study of Buruli ulcer, this approach involves defining probabilities of the transition of bacteria between lattice sites based on local information about bacteria density, normal tissue, and necrotic matter densities. By analysing the behaviour of particles on the lattice, one can derive a macroscopic equation that describes the evolution of bacteria ($u$). The resulting macroscopic system typically consists of coupled partial differential equations (PDEs) for the density of bacteria ($u$) and mycolactone concentration

($m$), along with ordinary differential equations (ODEs) for normal tissue ($v$), and necrotic matter ($n$).

## 4.2 Mathematical modelling

Assume that a random walk is being carried out by an individual bacterium in a 1D lattice with nodes $x_i$. We can imagine it jumping from one point to another on the lattice and also remaining stationary. We are interested in $u_i(t)$, the probability of finding a bacterial cell at $x_i$ at time $t$. Let $h$ and $\Delta t$ denote the lengths of the space and time intervals, respectively. Let $T_i^{\pm}$ denote the probabilities of jumping to the right (+) or to the left (-), respectively. Then we have

$$u_i(t+\Delta t) = \Big(T_{i-1}^{+}u_{i-1}(t) + T_{i+1}^{-}u_{i+1}(t)\Big)\Delta t + \Big(1 - \Delta t(T_i^{+} + T_i^{-})\Big)u_i(t). \tag{4.2.1}$$

When bacteria make a move, they 'test' their environment and decide whether to move according to the density of haptoattractants (normal tissue, and necrotic matter) at its current location, and its next location. Therefore, the probability for the bacteria per unit time to jump to right or left or stay in its place typically depends on the amount of necrotic matter and normal tissue and bacteria itself. Thus we define $T_i^{\pm}$ as:

$$T_i^{\pm}(u,v,n) := \lambda\Big(a(u_i,v_i) + \kappa(u_i,n_i)(\tau(n_{i\pm1}) - \tau(n_i))\Big),$$

where $v_i,\ n_i$ represent the probabilities of normal tissue and necrotic matter at a node $x_i$ at time $t$, respectively. Define $\kappa(u_i,n_i)$ as

$$\kappa(u_i,n_i) = \frac{K_uK_n}{K_uK_n + u_in_i}. \tag{4.2.2}$$

The choice of $\kappa$ as inversely proportional to the binding of bacteria $u$ and necrotic matter $n$ is motivated by the fact that increased binding between these entities reduces the tendency of bacteria $u$ to migrate towards regions with higher necrotic matter density. This formulation ensures that as the product of $u$ and $n$ increases (indicating stronger binding), $\kappa$ decreases, effectively reducing the probability of bacterial migration towards necrotic regions. Conversely, when the product of $u$ and $n$ decreases (indicating weaker binding), $\kappa$ increases, allowing for greater bacterial mobility towards areas with lower necrotic matter density.

In order to obtain the master equation we divide (4.2.1) by $\Delta t$ and pass to the limit for $\Delta t \to 0$

$$\frac{\partial u_i}{\partial t} = T_{i-1}^{+}u_{i-1} + T_{i+1}^{-}u_{i+1} - (T_i^{+} + T_i^{-})u_i.$$

By applying Taylor expansion (for the simplification of the notation we take $T_i := T(u_i, v_i, n_i)$):

$$T^-_{i+1}u_{i+1} = T^-_i u_i + h\frac{\partial}{\partial x}(T^-_i u_i) + \frac{h^2}{2}\frac{\partial^2}{\partial x^2}(T^-_i u_i) + \frac{h^3}{3!}\frac{\partial^3}{\partial x^3}(T^-_i u_i) + O(h^4)$$
$$T^+_{i-1}u_{i-1} = T^+_i u_i - h\frac{\partial}{\partial x}(T^+_i u_i) + \frac{h^2}{2}\frac{\partial^2}{\partial x^2}(T^+_i u_i) - \frac{h^3}{3!}\frac{\partial^3}{\partial x^3}(T^+_i u_i) + O(h^4).$$

Hence,

$$\begin{aligned}\frac{\partial u_i}{\partial t} =& T^+_i u_i - h\frac{\partial}{\partial x}(T^+_i u_i) + \frac{h^2}{2}\frac{\partial^2}{\partial x^2}(T^+_i u_i) - \frac{h^3}{3!}\frac{\partial^3}{\partial x^3}(T^+_i u_i)\\ &+ T^-_i u_i + h\frac{\partial}{\partial x}(T^-_i u_i) + \frac{h^2}{2}\frac{\partial^2}{\partial x^2}(T^-_i u_i) + \frac{h^3}{3!}\frac{\partial^3}{\partial x^3}(T^-_i u_i)\\ &- (T^+_i + T^-_i)u_i + O(h^4),\end{aligned}$$

is obtained.

$$\begin{aligned}\frac{\partial u_i}{\partial t} &= h\frac{\partial}{\partial x}\big((T^-_i - T^+_i)u_i\big) + \frac{h^2}{2}\frac{\partial}{\partial x^2}\big((T^+_i + T^-_i)u_i\big) + O(h^3)\\ &= \lambda\bigg( - h\frac{\partial}{\partial x}\big(\kappa(u_i, n_i)(\tau(n_{i+1}) - \tau(n_{i-1}))u_i\big)\\ &\quad + \frac{h^2}{2}\frac{\partial}{\partial x^2}\big(2a(u_i, v_i) + \kappa(u_i, n_i)(\tau(n_{i+1}) + \tau(n_{i-1}) - 2\tau(n_i))u_i\big)\bigg) + O(h^3)\\ &= \lambda\bigg( - 2h^2\frac{\partial}{\partial x}\big(\kappa(u_i, n_i)\frac{(\tau(n_{i+1}) - \tau(n_{i-1}))}{2h}u_i\big)\\ &\quad + \frac{h^2}{2}\frac{\partial}{\partial x^2}\big(2a(u_i, v_i)u_i\big) + \quad \frac{h^4}{2}\frac{\partial}{\partial x^2}\big(\kappa(u_i, n_i)\frac{(\tau(n_{i+1}) + \tau(n_{i-1}) - 2\tau(n_i))}{h^2}u_i\big)\bigg) + O(h^3)\\ &= \lambda\bigg( - 2h^2\frac{\partial}{\partial x}\big(\kappa(u_i, n_i)\frac{(\tau(n_{i+1}) - \tau(n_{i-1}))}{2h}u_i\big) + \frac{h^2}{2}\frac{\partial}{\partial x^2}\big(2a(u_i, v_i)u_i\big)\bigg) + O(h^3).\end{aligned}$$

Taking limit as $h \to 0$ with $2\lambda h^2 \to D$, and identifying the variables $u_i,\ n_i,\ v_i$ as continuous variables $u(x,t),\ n(x,t)$ and $v(x,t)$ respectively, we get

$$\frac{\partial u}{\partial t} = \frac{D}{2}(a(u,v)u)_{xx} - D(\kappa(u,n)u\tau'(n)n_x)_x.$$

We can obtain its generalisation to the higher dimensions as follows:

$$\partial_t u = D\nabla.\left(\frac{1}{2}\left(a(u,v) + \frac{\partial a}{\partial u}u\right)\nabla u + \frac{1}{2}\frac{\partial a}{\partial v}u\nabla v - \kappa u\frac{d\tau}{dn}\nabla n\right).$$

To show the interaction of bacteria with the normal tissue, we take $a(u,v) = \frac{K_u K_v}{K_u K_v + uv}$. This is a choice similar to that of $\kappa(u,n)$, which depends on the binding of bacteria to normal tissue. Therefore, we have

$$\frac{D}{2}\left(a(u,v) + \frac{\partial a}{\partial u}u\right)\nabla u + \frac{D}{2}\frac{\partial a}{\partial v}u\nabla v = \frac{DK_u^2K_v^2}{2(K_uK_v + uv)^2}\nabla u - \frac{DK_uK_vu^2}{2(K_uK_v + uv)^2}\nabla v.$$

To find the chemotactic sensitivity function $\tau(n)$, we use the receptor binding kinetics of bacteria to necrotic matter. To make this description, we use the studies [51, 52]. Thus, we

take $R$ as the receptors on bacteria which are free, $R_0$ as the receptors occupied by $n$, and let $R_T$ be the total amount of receptors on bacteria, which is conserved. Let $R_T = R + R_0$ be a constant.

Using simple mass action kinetics for the receptor binding we get

$$R + \frac{n}{K_n} \underset{k-}{\overset{k^+}{\rightleftharpoons}} R_0.$$

Thus, we obtain an ODE for the dynamics of occupied receptors :

$$\frac{dR_0}{dt} = k^+ \frac{n}{K_n} R - k^- R_0, \tag{4.2.3}$$

Since this binding reaction is very fast, we assume it attains equilibrium fast. Thus the steady state of (4.2.3) is

$$R_0{}^* = \frac{K R_T \frac{n}{K_n}}{1 + K \frac{n}{K_n}},$$

where $K = \frac{k^+}{k^-}$.

If we consider $\tau(n)$ to be a chemical mechanism to measure the concentration of chemoattractant $n$, we could assume $\tau(n)$ to be proportional to the amount of receptors occupied by $n$, that is

$$\tau(n) = bR_0{}^*,$$

where $b$ is a positive constant. Hence

$$D\kappa(u,n)u\frac{d\tau}{dn}\nabla n = \frac{D\kappa(u,n)b\frac{K}{K_n}R_T u}{(1 + K\frac{n}{K_n})^2}\nabla n,$$

is obtained.

Assuming the attachment rate $k^+$ and the detachment rate $k^-$ of bacteria to the necrotic matter to be almost the same, we get $K \approx 1$ and let $K_1 := DbKR_T$, and using (4.2.2) we have

$$D\kappa(u,n)u\frac{d\tau}{dn}\nabla n = \frac{K_1 K_u u}{(1 + \frac{n}{K_n})^2(K_u K_n + un)}\nabla n.$$

The macroscopic description of the quantities $u, n, v, m$ will be obtained from the microscopic lattice-based characterisation as follows:

$$\begin{aligned}
\partial_t u &= \nabla \cdot (D_u(u,v)\nabla u) - \nabla \cdot (\chi_1(u,v)u\nabla v) - \nabla \cdot (\chi_2(n,u)u\nabla n) \\
&\quad + \alpha \frac{n}{K_n + n} u(1 - \frac{u}{K_u} - \frac{v}{K_v} - \frac{n}{K_n}), \qquad t > 0,\ x \in \Omega, \\
\partial_t m &= D_m \Delta m + \delta \frac{u}{K_u + u} - \lambda m, \qquad t > 0,\ x \in \Omega, \\
\partial_t v &= -\beta_1 v \frac{m}{K_m}, \qquad t > 0,\ x \in \Omega, \\
\partial_t n &= \beta_2 \frac{v}{K_v}\frac{m}{K_m} - \gamma n, \qquad t > 0,\ x \in \Omega,
\end{aligned} \tag{4.2.4}$$

where

$$D_u(u,v)=\frac{DK_u^2K_v^2}{2(K_uK_v+uv)^2},\ \chi_1(u,v)=\frac{DK_uK_vu}{2(K_uK_v+uv)^2},\ \chi_2(n,u)=\frac{K_1K_u}{(1+\frac{n}{K_n})^2(K_uK_n+un)}.$$

We consider the no-flux boundary conditions

$$(D_u(u,v)\nabla u-\chi_1(u,v)\nabla v-\chi_2(n)u\nabla n)\cdot\nu=0,\ \nabla m\cdot\nu=0 \qquad t>0,\ x\in\partial\Omega, \quad (4.2.5)$$

where $\nu$ represents the outer unit normal vector and $\Omega$ is a domain in $\mathbb{R}^d$ which is bounded and has smooth enough boundary.
The initial conditions are

$$u(0,x)=u_0,\ v(0,x)=v_0,\ n(0,x)=n_0,\ m(0,x)=m_0 \qquad x\in\Omega. \quad (4.2.6)$$

The macroscopic equations of mycolactone, necrotic matter, and normal tissue are considered similar to those in Chapter 3.

## 4.3 Mathematical analysis

### 4.3.1 Local existence of a solution

The following result provides the local existence of solutions to (4.2.4). The proof is similar to that in Chapter 3.

**Lemma 4.3.1.** *Let $\Omega\subset\mathbb{R}^d$ $(d\geqslant 1)$ be a bounded domain with a smooth boundary. Also, suppose that $u_0\in W^{1,\infty}(\Omega)$; $m_0,\ v_0,\ n_0\in W^{2,\infty}(\Omega)$ satisfying compatibility condition on boundary with $u_0,\ m_0$ non negative and $v_0,\ n_0>0$. Then there exists $T_{max}>0$ and a quadruple of non-negative functions $(u,m,v,n)\in C^0([0,T_{\max})\times\bar{\Omega})\cap C^{2,1}((0,T_{\max})\times\Omega)$ which solve system (4.2.4) classically in $(0,T_{\max})\times\Omega$ and satisfy the dichotomy*

$$\begin{aligned}&\text{either } T_{max}=\infty \text{ or}\\ &\limsup_{t\nearrow T_{\max}}(||u(t)||_{L^\infty(\Omega)}+||m(t)||_{W^{1,\infty}(\Omega)}+||v(t)||_{W^{1,\infty}(\Omega)}+||n(t)||_{W^{1,\infty}(\Omega)})=\infty.\end{aligned} \quad (4.3.1)$$

*Proof.* We define the following closed, bounded, and convex set

$$Q:=\{\bar{u}\in L^\infty((0,T)\times\Omega):0\leqslant\bar{u}\leqslant||u_0||_{L^\infty(\Omega)}+1 \text{ a.e in } (0,T)\times\Omega\}$$

with $T>0$ small, to be fixed below. Let $A=||u_0||_{L^\infty(\Omega)}$. For $\bar{u}\in Q$, let $\phi(\bar{u})\equiv u$ denote the first component of the solution of the following system for $x\in\Omega,\ t\in(0,T)$:

$$\begin{aligned}\partial_t u&=\nabla\cdot(D_u(\bar{u},v)\nabla u)-\nabla\cdot(\chi_1(\bar{u},v))u\nabla v)-\nabla\cdot(\chi_2(n,\bar{u})u\nabla n)\\&\quad+uf(\bar{u},v,n)\\ \partial_t m&=D_m\Delta m+\delta\frac{\bar{u}}{K_u+\bar{u}}-\lambda m\\ \partial_t v&=-\beta_1 vm\\ \partial_t n&=\beta_2 vm-\gamma n\end{aligned} \quad (4.3.2)$$

with boundary conditions

$$\Big(D_u(\bar{u},v)\nabla u - \chi_1(\bar{u},v))\nabla v - \chi_2(\bar{u},n)\nabla n\Big)\cdot\nu = 0, \quad \nabla m\cdot\nu = 0 \quad t>0,\ x\in\partial\Omega,$$

and initial conditions

$$u(0,x)=u_0(x),\ m(0,x)=m_0(x),\ v(0,x)=v_0(x),\ n(0,x)=n_0(x), \quad x\in\Omega.$$

For any $q > \frac{d+2}{2}$, by using Theorem A.1 in [39], there exists a weak solution $m(t,x)$ in $W_q^{2,1}(\Omega_T)$ such that

$$||\nabla m||_{L^q((0,T)\times\Omega)} \leqslant \tilde{c_1}, \tag{4.3.3}$$

where $\tilde{c_1}$ is a positive constant which depends on $||m_0||_{W^{1,\infty}(\Omega)}$. Similarly as in Chapter 3, we also get:

$$||\nabla v||_{L^q((0,T)\times\Omega)} \leqslant \tilde{c_2}, \tag{4.3.4}$$

$$||\nabla n||_{L^q((0,T)\times\Omega)} \leqslant \tilde{c_3}. \tag{4.3.5}$$

Hence, we can rewrite the first equation in system (4.2.4) as

$$\partial_t u = \nabla\cdot(D_u(u,v)\nabla u - F(t,x)u) + f(\bar{u})u, \qquad x\in\Omega,\ t>0$$

where $||F||_{L^q((0,T)\times\Omega)} \leqslant c_4$ for some $c_4>0$. Using the parabolic theory(Thm V.2.1 and V.1.1 from [57]) and an idea in [95] which considers the results for Neumann boundary conditions instead of Dirichlet boundary conditions, $||u||_{L^\infty((0,T)\times\Omega)} \leqslant c_5$ and we get $c_6$ such that $||u||_{C^{\beta,\frac{\beta}{2}}((0,T)\times\Omega)} \leqslant c_6$ for some $\beta>0$. Hence $||u||_{L^\infty((0,T)\times\Omega)} \leqslant ||u_0||_{L^\infty(\Omega)} + c_7 T^{\frac{\beta}{2}}$ for some $T<1$ such that $c_7 T^{\frac{\beta}{2}} < 1$.

Consider the fixed point problem $\phi(\bar{u}) \equiv u$. By using the above, we have $\phi(Q)\subset Q$. Since $\phi$ is continuous and $\overline{\phi(Q)}$ is a compact subset in $L^\infty((0,T)\times\Omega)$, by applying Schauders's fixed point theorem we have that there exists at least one fixed point $u\in Q$. By using standard parabolic regularity $(u,m,v,n)$ is obtained as the classical solution of system (4.2.4) in $C^0([0,T)\times\bar{\Omega})\cap C^{2,1}((0,T)\times\Omega)$. By the comparison principle we get the non-negativity of solution components.

Next, to prove the existence of dichotomy 4.3.1 we can adopt the same steps as in Chapter 3. □

### 4.3.2 Boundedness of the solution components

In this section, we prove estimates for the solution components of ((4.2.4)).

**Remark 4.3.1.** *While the boundedness of solution components is independent of local existence, we use the same maximal time $T_{max}$ from the local existence proof in the boundedness proof.*

**Lemma 4.3.2.** *There exists $C_m > 0$ such that*

$$||m(t)||_{L^\infty([0,T_{\max})\times\Omega)} \leqslant ||m_0||_{L^\infty(\Omega)} + \frac{\delta}{\lambda}$$
$$||\nabla m||_{L^\infty([0,T_{\max})\times\Omega)} \leqslant C_m(||\nabla m_0||_{L^\infty(\Omega)} + 1),$$

*Proof.* This proof is same as in Chapter 3 of this thesis.
By the PDE comparison principle Theorem A.3 in [59]), we get

$$0 \leqslant m \leqslant A := \max\left\{K_m, \frac{\delta}{\lambda}\right\}.$$

□

**Remark 4.3.2.** *By solving the third equation in (4.2.4), we obtain*

$$v(t,x) = v_0(x)\exp\left(-\frac{\beta_1}{K_m}\int_0^t m(s,x)ds\right), \quad t \in [0,T_{max}),\ x \in \Omega. \tag{4.3.6}$$

*By using the non-negativity of $m$, the assumption on $v_0$, in 4.3.1,* (4.3.6)*, and the ODE comparison principle we can conclude that there exist $K_v^- > 0$*

$$K_v^- < v(t,x) \leqslant K_v, \quad t \in [0,T_{max}),\ x \in \Omega. \tag{4.3.7}$$

*By using Lemma 4.3.2, we also get*

$$||v||_{L^\infty([0,T_{\max})\times\Omega)} \leqslant C_1,$$
$$||\nabla v||_{L^\infty([0,T_{\max})\times\Omega)} \leqslant c_1.$$

**Remark 4.3.3.** *If we consider the fourth equation of system* (4.2.4) *and using the variation of constants formula, we obtain the following representation:*

$$n(t,x) = e^{-\gamma t}n_0(x) + \frac{\beta_2}{K_m K_v}\int_0^t m(s,x)v(s,x)e^{-\gamma(t-s)}ds. \quad t \in [0,T_{max}),\ x \in \Omega. \tag{4.3.8}$$

*By using the non-negativity of $\gamma$, the assumption on $n_0$ in 4.3.1,* (4.3.8)*, and the ODE comparison principle, there exist $K_n^- > 0$*

$$K_n^- < n(t,x) \leqslant B, \quad t \in [0,T_{max}),\ x \in \bar{\Omega},$$

*where $B = \max\left\{K_n, \frac{\beta_2}{\gamma}\right\}$. Using* (4.3.8)*, Lemma 4.3.2, and Remark 4.3.2, we also get*

$$||n||_{L^\infty([0,T_{\max})\times\Omega)} \leqslant C_2,$$

*and*

$$||\nabla n||_{L^\infty([0,T_{\max})\times\Omega)} \leqslant c_2.$$

**Lemma 4.3.3.** *We have the following estimate*

$$\int_\Omega u(t,x)dx \leqslant C := max\left\{\int_\Omega u_0(x)dx, 1\right\}, \quad t \in [0,T_{max}),\ x \in \bar{\Omega}. \tag{4.3.9}$$

*Proof.* By integrating the first equation of (4.2.4) and using Remark 4.3.2, 4.3.3, the non negativity of $u$, the no flux boundary condition and the Cauchy-Schwarz inequality, we have

$$\frac{d}{dt}\int_\Omega u \leqslant \alpha\int_\Omega u - \alpha\int_\Omega u^2 \leqslant \alpha\int_\Omega u - \alpha\Big(\int_\Omega u\Big)^2. \tag{4.3.10}$$

Then the estimate is an immediate result using the comparison principle for ODEs. □

**Lemma 4.3.4.** *For any $p \in [2,\infty)$ there exists $C_p(T_{max}) > 0$ such that*

$$||u(t)||_{L^p(\Omega)} \leqslant C_p(T_{max}), \quad t \in (0, T_{max}).$$

*Proof.* In virtue of the estimates in Remark 4.3.2 and Remark 4.3.3, there exist some $D_1, D_2 > 0$ such that the diffusion coefficient satisfies the following inequality

$$\frac{D_1}{(1+u)^2} \leqslant \frac{DK_u^2K_v^2}{2(K_uK_v+uv)^2} \leqslant D_2, \tag{4.3.11}$$

and the taxis coefficients satisfy

$$\frac{DK_uK_vu^2}{2(K_uK_v+uv)^2} \leqslant D_3, \tag{4.3.12}$$

$$\frac{K_1K_uu}{(K_n+n)^2(K_uK_n+nu)} \leqslant D_4, \tag{4.3.13}$$

for some constants $D_3, D_4 > 0$. Testing the first equation in the system with $(1+u)^{p-1}$ and using Young's inequality, we get

$$\begin{aligned}
\frac{1}{p}\int_\Omega \partial_t(1+u)^p &= \int_\Omega (1+u)^{p-1}\partial_t u \\
&= \int_\Omega (1+u)^{p-1}\Big(\nabla\cdot\big(D_u(u,v)\nabla u\big) - \nabla\cdot\big(\chi_1(u,v)u\nabla v\big) - \nabla\cdot\big(\chi_2(u,n)u\nabla n\big) \\
&\qquad + \alpha u\frac{n}{1+n}\big(1-\frac{u}{K_u}-\frac{v}{K_v}-\frac{n}{K_n}\big)\Big) \\
&\leqslant -(p-1)\int_\Omega D_1(1+u)^{p-4}|\nabla u|^2 + \int_\Omega (p-1)\chi_1(u,v)u(1+u)^{p-2}\nabla v\cdot\nabla u \\
&\qquad + \int_\Omega (p-1)\chi_2(u,n)u(1+u)^{p-2}\nabla n\cdot\nabla u \\
&\qquad + \int_\Omega \alpha u(1+u)^p\frac{n}{1+n}\left(1-\frac{u}{K_u}-\frac{v}{K_v}-\frac{n}{K_n}\right), \\
&\leqslant -\frac{4(p-1)}{(p-2)^2}\int_\Omega D_1|\nabla(1+u)^{\frac{p-2}{2}}|^2 + \frac{4(p-1)}{(p-2)^2}\int_\Omega D_1|\nabla(1+u)^{\frac{p-2}{2}}|^2 \\
&\qquad + \frac{(p-1)D_3^2}{2D_1}\int_\Omega |\nabla v|^2(1+u)^p + \frac{(p-1)D_4^2}{2D_1}\int_\Omega |\nabla n|^2(1+u)^p \\
&\qquad + \int_\Omega \alpha u(1+u)^{p-1} - \int_\Omega \alpha_1\frac{u^2(1+u)^{p-1}}{K_u} \\
&\leqslant \left(\frac{(p-1)}{2D_1}(D_3^2||\nabla v||_{L^\infty}^2 + D_4^2||\nabla n||_{L^\infty}^2) + \alpha\right)\int_\Omega (1+u)^p.
\end{aligned}$$

Now by applying Gronwall's inequality, we get the desired result. □

**Theorem 4.3.1.** *For any $T_{max} > 0$, there exists $C_\infty(T_{max}) > 0$ such that*

$$0 \leqslant ||u||_{L^\infty((0,T_{max})\times\Omega)} \leqslant C_\infty(T_{max}) \tag{4.3.14}$$

*Proof.* This is an immediate result of Remark 3.7 in [92] with $m_1 = 0$ and $m_2 = 2$. □

**Theorem 4.3.2.** *Under the assumptions of Lemma 4.3.1, system* (4.2.4) *has a non-negative classical solution $(u, v, n, m)$ which is global in time.*

*Proof.* This is now an immediate consequence of (4.3.1), Lemma 4.3.2, remarks 4.3.2, 4.3.3, and Theorem 4.3.1. □

## 4.4 Numerical simulations

#### 4.4.0.1 Nondimensionalisation

Before performing the numerical simulation, we nondimensionalise our system(4.2.4). Therefore, we take

$$\bar{u} = \frac{u}{K_u},\ \tilde{v} = \frac{v}{K_v},\ \tilde{n} = \frac{n}{K_n},\ \tilde{m} = \frac{m}{K_m},\ \tilde{x} = x\sqrt{\frac{\alpha_u}{D_m}},\ \tilde{t} = t\alpha_u. \tag{4.4.1}$$

By using the transformations in (4.4.1), our system (4.2.4) becomes

$$\begin{aligned}
\bar{u}_{\tilde{t}} &= \nabla\cdot\left(\frac{\tilde{D}}{(1+\bar{u}\tilde{v})^2}\nabla\bar{u}\right) - \nabla\cdot\left(\frac{\tilde{D}\bar{u}^2}{(1+\bar{u}\tilde{v})^2}\nabla\tilde{v}\right) - \nabla\cdot\left(\frac{\tilde{\chi}_n\bar{u}}{(1+\tilde{n})^2(1+un)}\nabla\tilde{n}\right)\\
&\quad + \frac{\tilde{n}}{1+\tilde{n}}\bar{u}\left(1-\bar{u}-\tilde{v}-\tilde{n}\right),\\
\tilde{m}_{\tilde{t}} &= \Delta\tilde{m} + \frac{\tilde{\delta}\bar{u}}{1+\bar{u}} - \tilde{\lambda}\tilde{m},\\
\tilde{v}_{\tilde{t}} &= -\tilde{\beta}_1\tilde{m}\tilde{v},\\
\tilde{n}_{\tilde{t}} &= \tilde{\beta}_2\tilde{m}\tilde{v} - \tilde{\gamma}\tilde{n},
\end{aligned} \tag{4.4.2}$$

where

$$\tilde{D} = \frac{D}{2 * D_m},\quad \tilde{\chi}_n = \frac{K_1}{D_m},\quad \tilde{\beta}_1 = \frac{\beta_1}{\alpha_u},$$

$$\tilde{\beta}_2 = \frac{\beta_2}{\alpha_u K_N},\quad \tilde{\gamma} = \frac{\gamma}{\alpha_u},\quad \tilde{\delta} = \frac{\delta}{K_m\alpha_u},\quad \tilde{\lambda} = \frac{\lambda}{\alpha_u}$$

To simplify the system, we omit all tildes and bars in system (4.4.2) and continue with this system.

### 4.4.1 Numerical results

This section explores the numerical solutions of the macroscopic system (4.4.2) in a two-dimensional (2D) setting. Building upon the methodologies outlined in the preceeding chapters, we employ the finite difference method (FDM) to discretise the model in space. No-flux boundary conditions are imposed for the variables $u$ and $m$. The spatial domain is confined to the unit square $[0,1] \times [0,1]$.

In discretising the $m-$equation, we adopt a forward difference scheme for the time derivatives and a central difference scheme for the spatial derivatives. Similarly, for the equations governing $n$ and $v$, we employ a forward finite difference method for the time derivatives. For the equation characterising $u$ we use a nonstandard finite difference discretisation technique inspired by previous works [8, 28, 65]. Specifically, we discretise the diffusion terms explicitly, while treating the reaction terms implicitly, ensuring numerical stability and accuracy. The discretisation of diffusion and taxis terms as follows:

$$\begin{aligned}
\nabla(D_u(u,v)\nabla u)|_{x_i,y_j} =& \frac{1}{2(\Delta x)^2}\sum_{l\in M_i}\Big(D_u(u^k_{l,j},v^{k+1}_{l,j})+D_u(u^k_{i,j},v^{k+1}_{i,j})\Big)(u^{k+1}_{l,j}-u^{k+1}_{i,j})\\
&+\frac{1}{2(\Delta y)^2}\sum_{r\in N_i}\Big(D_u(u^k_{i,r},v^{k+1}_{i,r})+D_u(u^k_{i,j},v^{k+1}_{i,j})\Big)(u^{k+1}_{i,r}-u^{k+1}_{i,j}),\\
\nabla(\chi_1(u,v)\nabla v)|_{x_i,y_j} =& \frac{1}{2(\Delta x)^2}\sum_{l\in M_i}\Big(\chi_1(u^k_{l,j},v^{k+1}_{l,j})u^k_{l,j}+\chi_1(u^k_{i,j},v^{k+1}_{i,j})u^k_{i,j}\Big)(v^{k+1}_{l,j}-v^{k+1}_{i,j})\\
&+\frac{1}{2(\Delta y)^2}\sum_{r\in N_i}\Big(\chi_1(u^k_{i,r},v^{k+1}_{i,r})u^k_{i,r}+\chi_1(u^k_{i,j},v^{k+1}_{i,j})u^k_{i,j}\Big)(v^{k+1}_{i,r}-v^{k+1}_{i,j}),\\
\nabla(\chi_2(n,u)\nabla n)|_{x_i,y_j} =& \frac{1}{2(\Delta x)^2}\sum_{l\in M_i}\Big(\chi_2(u^k_{l,j},n^{k+1}_{l,j})u^k_{l,j}+\chi_2(u^k_{i,j},n^{k+1}_{i,j})u^k_{i,j}\Big)(n^{k+1}_{l,j}-n^{k+1}_{i,j})\\
&+\frac{1}{2(\Delta y)^2}\sum_{r\in N_i}\Big(\chi_2(u^k_{i,r},n^{k+1}_{i,r})u^k_{i,r}+\chi_2(u^k_{i,j},n^{k+1}_{i,j})u^k_{i,j}\Big)(n^{k+1}_{i,r}-n^{k+1}_{i,j}),
\end{aligned} \tag{4.4.3}$$

where $M_i = \{i-1, i+1\}$ and $N_i = \{j-1, j+1\}$, are indexed according to the neighbourhood of $x_i, y_j$.

Throughout the numerical simulations, we apply the no-flux boundary conditions in (4.2.5) on the boundary of $\Omega = (0,1) \times (0,1)$ for 2D. For the simulations, we obtain the non dimensionalised parameter values using the same dimesional parameter values and initial condition (3.4.1) as in Chapter 3, along with non dimensionalised value $\chi_n = .001$. The results at $t = 100,\ t = 150,\ t = 200,\ t = 250$ hours are shown in Fig 4.1. These observations align well with the predictions of the model, providing insights into the expected behaviour of the described biological phenomena.

We also include Fig 4.2 comparing the densities of bacteria, mycolactone concentration, normal tissue, and necrotic matter at various time points. Initially, differences between models show a peak of around 0.03 at early time points (t=50 to t=100), which reduces

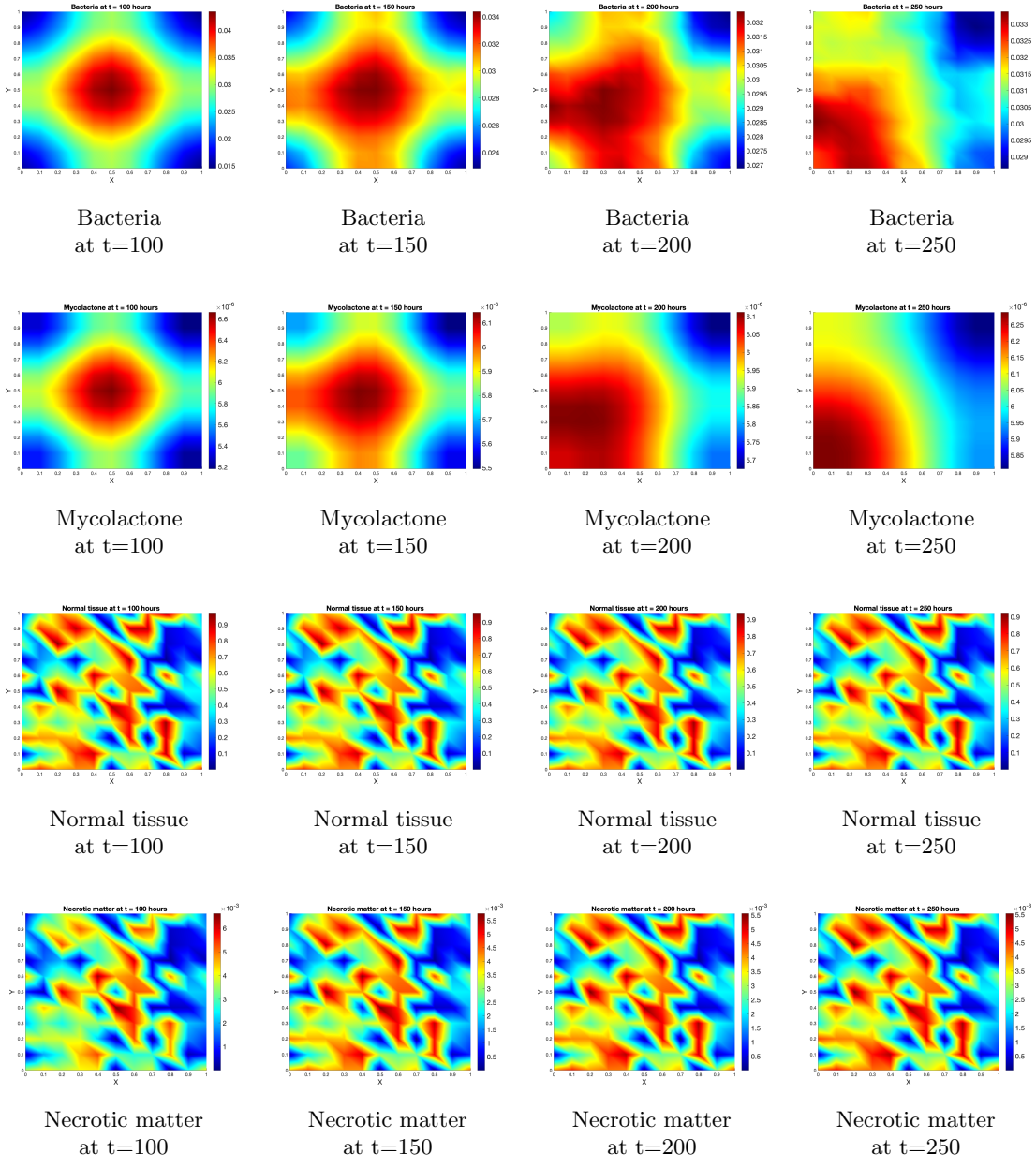


Bacteria at t=100 | Bacteria at t=150 | Bacteria at t=200 | Bacteria at t=250

Mycolactone at t=100 | Mycolactone at t=150 | Mycolactone at t=200 | Mycolactone at t=250

Normal tissue at t=100 | Normal tissue at t=150 | Normal tissue at t=200 | Normal tissue at t=250

Necrotic matter at t=100 | Necrotic matter at t=150 | Necrotic matter at t=200 | Necrotic matter at t=250

Figure 4.1: Bacteria, mycolactone, normal tissue and necrotic matter at different times

to 0.0225 by t=250, suggesting that bacterial growth and spread decelerates over time in Chapter 4. This phenomenon may be attributed to the diffusion coefficient in (4.4.2) being dependent on both bacterial and normal tissue concentrations, potentially retarding the initial spread of bacteria at such high densities. Similarly, the taxis coefficients could alter bacterial movement patterns and reduce their accumulation in favourable areas. These more sophisticated representations of bacterial movement and spread in this model likely contribute to a more gradual disease progression by introducing additional limiting factors on bacterial proliferation and distribution. Mycolactone concentration differences mirror bacterial growth patterns, as mycolactone production is biologically linked to bacterial activity.

A key observation is the positive difference in normal tissue, which suggests that the model (4.4.2) predicts either slower tissue damage or more preservation of healthy tissue compared to Chapter 3. By t=250, differences reach 0.035, indicating that tissue damage is either mitigated or delayed in certain regions. This might be due to the non linear diffusion and taxis coefficients.

In conclusion, the diffusion and haptotaxis coefficients in model (4.4.2) result in reduced bacterial spread, more preservation of normal tissue, and less necrosis. This outcome may be attributed to decreased tactic sensitivity towards necrotic matter and normal tissue, and reduced diffusion. These findings suggest that the models presented in Chapter 3 are preferable to the one developed in this chapter, as they necessitate fewer ad-hoc assumptions regarding bacterial responses to signals in adjacent locations. Furthermore, they can incorporate more detailed information about the spatial distribution of tissue, thus allowing for more realistic descriptions than the uniform distribution considered in this work. Moreover, the model in Chapter 4 likely underestimates wound spread. Consequently, the model presented in Chapter 3 should be favoured.

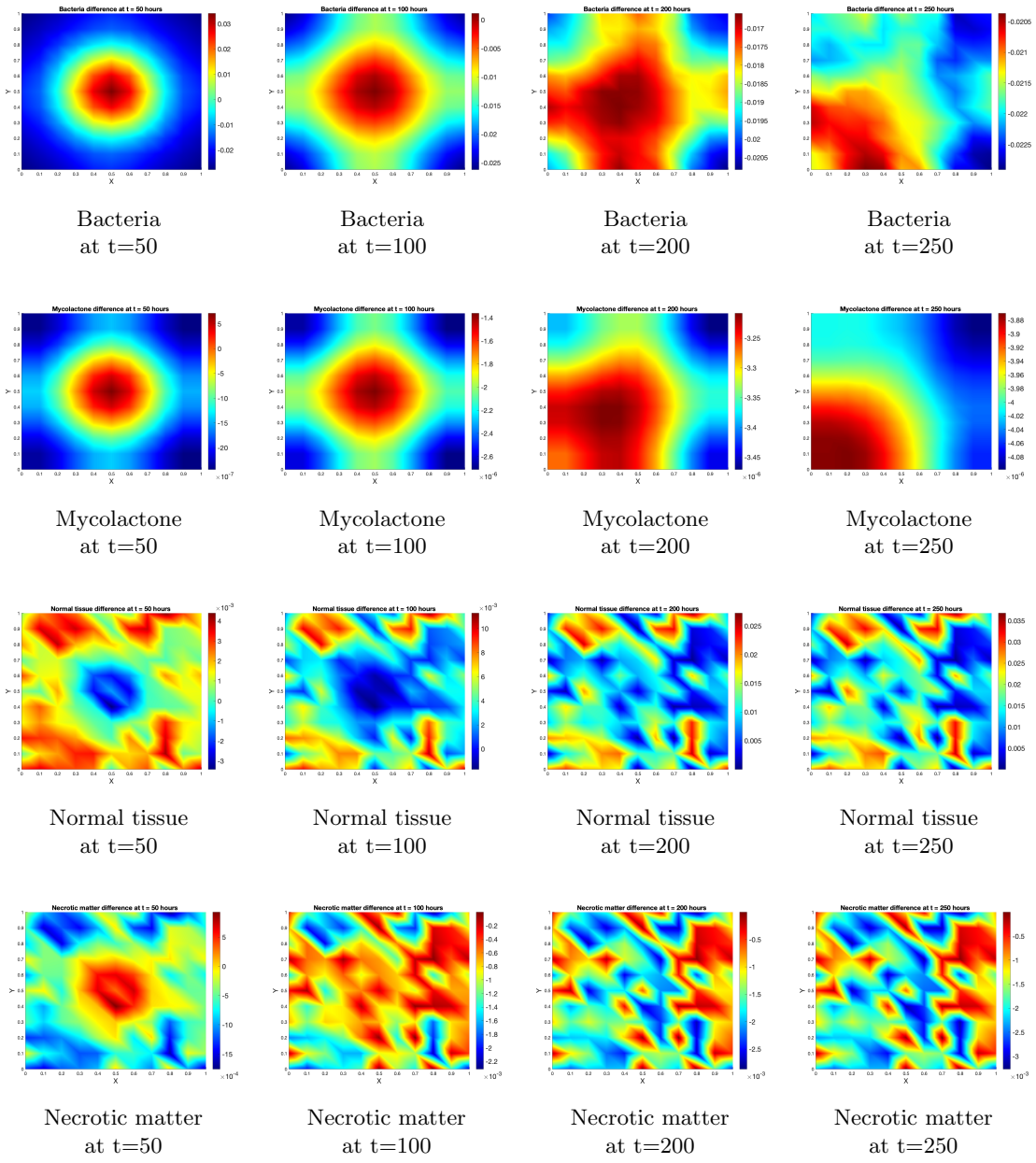


Figure 4.2: Difference in density of bacteria, mycolactone concentration, normal tissue and necrotic matter at different times for the models obtained in Chapters 3 and 4 (Chapter 4 - Chapter 3: Scenario 1)

Chapter 5

# Conclusion

Mathematical modelling has long been a cornerstone in the biomedical field, playing a crucial role in developing treatment methods and understanding complex biological processes. Over the past few decades, tissue regeneration and wound formation have been two significant areas where mathematical models have been applied, yet effective models for cell movement in meniscus tissue and Buruli ulcers remain underdeveloped. In this thesis, we have developed, analysed, and numerically simulated mathematical models that describe cell movement, specifically focusing on meniscus tissue regeneration and the progression of Buruli ulcers.

In the second chapter, we introduced a comprehensive macroscale model for stem cells, chondrocytes, and hyaluron. This model was developed by upscaling the microscale description of cells to the mesoscale and then to the macroscale. The resulting system is a coupled set of reaction-diffusion-transport equations (RDTEs) and ordinary differential equations (ODEs).

We performed a stability analysis of a simplified version of the model to ensure its robustness and reliability. This helped us understand the conditions under which the model remains stable and the potential scenarios that could lead to instability. Following this, we conducted numerical simulations to study the patterns formed under various initial conditions. These simulations provided valuable insights into the dynamic behaviour of the system, revealing significant impacts of tissue topography on cell behaviour. The findings demonstrated how different initial distributions and densities of cells and hyaluron components could influence the overall tissue regeneration process.

In the third chapter, we developed a model for the migration of Buruli ulcer-causing bacteria, influenced by haptotaxis, using multiscale modelling. Unlike the meniscus tissue model, we began at the mesoscale and proceeded from there. This model interconnects bacteria, mycolactone, necrotic matter, and normal tissue, forming a system of four equations.

We compared different scenarios based on the haptotaxis sensitivity of bacteria towards

normal and necrotic matter. Numerical simulations indicated that the dynamics of bacteria, mycolactone, and necrotic matter is interconnected and they spread in the same direction. A notable finding was that a lower initial density of normal tissue significantly reduces the spread and growth of bacteria and mycolactone. This suggests that the availability of normal tissue at the beginning of the infection is a crucial factor in wound progression. This finding supports the practice of early intervention, such as overheating the infected site, to control disease progression. The simulations provided a clear visualisation of how the disease spreads and how different intervention strategies can alter this progression.

In the fourth chapter, we sought to incorporate more detailed modelling at the single cell level using a random jump approach. This model considers the interactions of bacteria with various stimuli like normal tissue and necrotic matter, utilising mass action kinetics for receptor bindings on bacteria. We derived parameters describing the tactic behaviour and non-linear diffusion of bacteria, resulting in a non-linear diffusion equation.

This RDTE was coupled with the reaction-diffusion equation (RDE) for mycolactone and ODEs describing the dynamics of normal and necrotic matter. We proved the existence of a global classical solution for this system. Subsequently, we conducted numerical simulations that aligned with expected behaviours, demonstrating the model's validity. These simulations offered insights into the micro-level interactions and movements of bacteria, contributing to a deeper understanding of disease progression at a cellular level. The results also were in agreement with the expected behaviour of the entities.

## 5.1 Outlook

**Enhancing meniscus regeneration models**
Future research on meniscus regeneration could focus on understanding the impact of different environmental conditions on tissue regeneration. Factors such as oxygen levels, nutrient availability, and mechanical stresses could be integrated into the model to study their effects on cell proliferation and differentiation. By doing so, the optimal conditions for tissue regeneration and develop strategies to enhance the healing process can be identified.

**Advancing Buruli ulcer modelling**
For Buruli ulcer modelling, a model using kinetic transport equations to better capture cell dynamics at the micro-level can be developed. Incorporating more detailed bacterial behaviour by starting at a lower level could enhance the model's accuracy. The effectiveness of treatment methods within the model can also be considered. For instance, incorporating treatment strategies such as initial heating of the wound area could help control the spread of the infection. By introducing coefficients that account for temperature variations, we could simulate the effects of this treatment more accurately. This could lead to the conceptual development of new therapeutic approaches and improve existing ones.

Additionally, the potential of combining multiple treatment methods to achieve better outcomes can be explored. For example, combining antibiotics with thermal therapy could be modelled to study their combined effects on bacteria eradication and wound healing. This approach could provide insights into the most effective treatment combinations and optimise therapy protocols.

**Refining random jump models**

The inclusion of additional biological factors and interactions in the model as mentioned in the previous section can be explored. Additionally, the impact of immune response, the presence of other microbial species, and the role of the extracellular matrix in bacterial movement could be integrated into the model. By doing so, a more comprehensive and accurate representation of the biological system could be reached.

**Integration of multiscale modelling approaches**

In future works, further exploration of the integration of different modelling approaches to capture the complexity of biological systems more effectively can be done. Combining continuous and discrete modelling techniques maximises the strengths of each approach and overcomes its limitations. This hybrid modelling approach can provide a more detailed and accurate representation of biological processes.

Furthermore, it is possible to explore the potential of personalised medicine by developing patient-specific models. Individual patient data can be incorporated into the models in order to tailor treatment strategies to each patient's unique characteristics, making treatment more effective and targeted.

In conclusion, while this thesis has proposed some steps towards developing mathematical models for cell movement in tissue regeneration and wound formation, there remains substantial scope for further research. Adding more detailed biological data to our models and exploring new modelling techniques can improve the understanding of the relevant biomedical processes and contribute to the development of better treatment methods.

# Appendix

**Theorem 5.1.1** (Theorem V.1.1 in [57]). *Consider the parabolic equation:*

$$\frac{\partial u}{\partial t} = \sum_{i=1}^{n} \frac{\partial}{\partial x_i}(a_i(x,t,u,\nabla u)) + a(x,t,u,\nabla u) \tag{5.1.1}$$

*in $Q_T = (0,T) \times \Omega$, where $\Omega$ is a bounded domain in $\mathbb{R}^n$.*
*Assume the following conditions:*

1. ***Condition 1:*** *$a_i(x,t,u,p)$ and $a(x,t,u,p)$ are continuous functions of their arguments.*

2. ***Condition 2:*** *There exist positive constants $\nu$, $\mu$, and nonnegative functions $\phi_0(x,t)$, $\phi_1(x,t)$ such that for all $(x,t) \in Q_T$, $u \in \mathbb{R}$, and $p \in \mathbb{R}^n$:*

$$a_i(x,t,u,p)p_i \geqslant \nu(|u|)|p|^2 - \phi_0(x,t) \tag{5.1.2}$$
$$|a_i(x,t,u,p)| \leqslant \mu(|u|)|p| + \phi_1(x,t) \quad \text{for } i = 1,\ldots,n \tag{5.1.3}$$
$$|a(x,t,u,p)| \leqslant \mu_1(|u|)p^2 + \phi_2(x,t) \tag{5.1.4}$$

   *in which $\nu(\psi)$ and the $\mu_i(\psi)$ are, as elsewhere, positive continuous functions of $\psi \geqslant 0$ with $\nu(\psi)$ monotonically decreasing, the $\mu_i(\psi)$ monotonically increasing and the functions $\varphi_i(x,t)$ non negative and having the finite norms*

$$\|\phi_0\|_{L^q(Q_T)}, \|\phi_2\|_{L^q(Q_T)}, \|\phi_1\|_{L^q(Q_T)} \leqslant M \tag{5.1.5}$$

   *for some constant $M > 0$ and $q \geqslant 1$.*

3. ***Condition 3:*** *$u$ is a weak solution of the equation with $u \in L^\infty(Q_T)$.*

*Then for any $Q' \subset Q_T$ we have $u \in C^{\alpha,\alpha/2}(Q_T)$ for some $\alpha > 0$ and there exists a constant $C$ such that: $||u||_{C^{\alpha,\alpha/2}(Q')} \leqslant C$. The constants $C$ and $\alpha$ depend only on $n$, $\nu$, $\mu$, $\mu_1$, $M$, $q$, and $dist(Q', Q_T)$.*

**Theorem 5.1.2** (Theorem V.2.1 in [57]). *Consider the quasilinear parabolic equation:*

$$u_t = \frac{\partial}{\partial x_i}[a_i(x,t,u,\nabla u)] + a(x,t,u,\nabla u) \tag{5.1.6}$$

*in $Q_T = (0,T) \times \Omega$, where $\Omega$ is a bounded domain in $\mathbb{R}^d$.*
*Assume the following conditions on $a_i$ and $a$:*

1. ***Condition 1:*** *$a_i$ and $a$ are continuous in $u$ and $\nabla u$.*
2. ***Condition 2:*** *There exists a positive constant $c$ such that*

$$|a_i(x,t,u,p)| \leqslant c|p| + c|u|^\alpha + \phi_1(x,t) \tag{5.1.7}$$
$$|a(x,t,u,p)| \leqslant c|u|^\gamma + \phi_2(x,t) \tag{5.1.8}$$

   *where:*
   - $0 \leqslant \alpha \leqslant 1 + \frac{2}{n}$
   - $0 \leqslant \gamma \leqslant 1 + \frac{4}{n}$
   - $\phi_1 \in L^2(Q_T)$, $\phi_2 \in L^q(Q_T)$ *for some* $q \geqslant 1$

3. ***Condition 3:***

$$a_i(x,t,u,p)p_i \geqslant \nu|p|^2 - \mu|u|^\delta - u^2\phi(x,t), \quad \nu > 0 \tag{5.1.9}$$
$$-a(x,t,u,p)u \leqslant \mu_0|p|^2 + \mu|u|^\delta + u^2\phi(x,t) \tag{5.1.10}$$

   *where:*
   - $\phi \in L^q(Q_T)$ *for some* $q \geqslant 1$
   - $\delta > 2$
   - $\mu_0 < \nu$

*Then any generalised solution $u \in V_2^{1,0}(Q_T)$ satisfies the following condition:*

$$\|u\|_{L^\infty((0,T)\times\Omega)} \leqslant c_5 \tag{5.1.11}$$

*where $c_5$ depends only on $\lambda$, $c$, $\|\phi\|_{L^q(Q_T)}$, $T$, $|\Omega|$, $n$ (the dimension), and $||u||_{L^{q_1,r_1}(Q_T)}$ for any positive numbers $q_1$ and $r_1$.*

# Bibliography


[1] P. Agbenorku. "Buruli Ulcer Disability in Ghana: The Problems and Solutions". In: *Journal of Advances in Medicine and Medical Research* 4.6 (2013), 1355–1365. DOI: 10.9734/BJMMR/2014/6245.

[2] P. Agbenorku and P. Saunderson. "Mycobacterium ulcerans Disease of the Face: The Fate of the Victims". In: *Mycobacterial Diseases* 3 (Dec. 2013), 4 pages. DOI: 10.4172/2161-1068.1000133.

[3] N. Alghamdi, M. Horsburgh, and B. Vasiev. *A Combined Experimental and Mathematical Study of The Evolution of Microbial Community Composed of Interacting Staphylococcus Strains*. 2024. DOI: 10.48550/arXiv.2402.04939.

[4] G. H. Altman, R. L. Horan, I. Martin, J. Farhadi, P. R. Stark, V. Volloch, J. C. Richmond, G. Vunjak-Novakovic, and D. L. Kaplan. "Cell differentiation by mechanical stress". In: *The FASEB Journal* 16.2 (2002), pp. 1–13. DOI: 10.1096/fj.01-0656fje.

[5] H. Amann. "Hopf bifurcation in quasilinear reaction-diffusion systems". In: *Delay Differential Equations and Dynamical Systems*. Ed. by S. Busenberg and M. Martelli. Berlin, Heidelberg: Springer Berlin Heidelberg, 1991, pp. 53–63. DOI: 10.1007/BFb0083479.

[6] G. Amofah, F. Bonsu, C. Tetteh, J. Okrah, K. Asamoa, K. Asiedu, and J. Addy. "Buruli ulcer in Ghana: results of a national case search". In: *Emerging infectious diseases* 8.2 (2002), p. 167. DOI: 10.3201/eid0802.010119.

[7] A Andreykiv, F Van Keulen, and P. Prendergast. "Simulation of fracture healing incorporating mechanoregulation of tissue differentiation and dispersal/proliferation of cells". In: *Biomechanics and modeling in mechanobiology* 7 (2008), pp. 443–461. DOI: 10.1007/s10237-007-0108-8.

[8] R. Anguelov and J. Lubuma. "Contributions to the mathematics of the nonstandard finite difference method and applications". In: *Numerical Methods for Partial Differential Equations* 17 (Sept. 2001), pp. 518 –543. DOI: 10.1002/num.1025.

[9] U. M. Ascher, S. J. Ruuth, and B. T. R. Wetton. "Implicit-Explicit Methods for Time-Dependent Partial Differential Equations". In: *SIAM Journal on Numerical Analysis* 32.3 (1995), pp. 797–823. DOI: 10.1137/0732037.

[10] K. Asiedu and S. Etuaful. "Socioeconomic implications of *Buruli ulcer* in Ghana: a three-year review". In: *Transactions of the Royal Society of Tropical Medicine and Hygiene* 92.6 (1998), pp. 1015–1022. DOI: 10.4269/ajtmh.1998.59.1015.

[11] K. A. Athanasiou and J. Sanchez-Adams. *Engineering the Knee Meniscus*. Springer International Publishing, 2009. DOI: 10.1007/978-3-031-02576-1.

[12] A. C. AufderHeide and K. A. Athanasiou. "Mechanical stimulation toward tissue engineering of the knee meniscus". In: *Annals of biomedical engineering* 32 (2004), pp. 1163–1176. DOI: 10.1114/b:abme.0000036652.31658.f3.

[13] A. Bailón-Plaza and M. C. Van der Meulen. "A Mathematical Framework to Study the Effects of Growth Factor Influences on Fracture Healing". In: *Journal of Theoretical Biology* 212.2 (2001), pp. 191–209. DOI: 10.1006/jtbi.2001.2372.

[14] J. Barber, M. Tronzo, C. H. Horvat, G. Clermont, J. Upperman, Y. Vodovotz, and I. Yotov. "A three-dimensional mathematical and computational model of necrotizing enterocolitis". In: *Journal of Theoretical Biology* 322 (2013), pp. 17–32. DOI: 10.1016/j.jtbi.2012.11.018.

[15] D. Barker. "Epidemiology of *Mycobacterium ulcerans* infection". In: *Transactions of the Royal Society of Tropical Medicine and Hygiene* 67 (1973), pp. 43–7. DOI: 10.1016/0035-9203(73)90317-9.

[16] N. Bellomo, A. Bellouquid, L. Gibelli, and N. Outada. *A quest towards a mathematical theory of living systems*. Springer, 2017. DOI: 10.1007/978-3-319-57436-3.

[17] N. Bellomo, A. Bellouquid, Y. Tao, and M. Winkler. "Toward a mathematical theory of Keller–Segel models of pattern formation in biological tissues". In: *Mathematical Models and Methods in Applied Sciences* 25.09 (2015), pp. 1663–1763. DOI: 10.1142/S021820251550044X.

[18] E. Borgiani, G. N. Duda, and S. Checa. "Multiscale Modeling of Bone Healing: Toward a Systems Biology Approach". In: *Frontiers in Physiology* 8 (2017). DOI: 10.3389/fphys.2017.00287.

[19] K. Campbell, S. Naire, and J. H. Kuiper. "A mathematical model of cartilage regeneration after chondrocyte and stem cell implantation -II: the effects of co-implantation". In: *Journal of Tissue Engineering* 10 (2019), p. 204173141982779. DOI: 10.1177/2041731419827792.

[20] K. Campbell, S. Naire, and J. H. Kuiper. "A mathematical model of cartilage regeneration after chondrocyte and stem cell implantation-I: the effects of growth factors". In: *Journal of Tissue Engineering* 10 (2019), p. 204173141982779. DOI: 10.1177/2041731419827791.

[21] S. Chettiparambil Mohanan, N. Mohan, and C. Surulescu. *On a mathematical model for tissue regeneration*. 2024. DOI: 10.48550/arXiv.2403.04516.

[22] E. A. Codling, M. J. Plank, and S. Benhamou. "Random walk models in biology". In: *Journal of The Royal Society Interface* 5.25 (2008), pp. 813–834. DOI: 10.1098/rsif.2008.0014.

[23] M. Conte, Y. Dzierma, S. Knobe, and C. Surulescu. "Mathematical modeling of glioma invasion and therapy approaches via kinetic theory of active particles". In: *Mathematical Models and Methods in Applied Sciences* 33.05 (2023), pp. 1009–1051. DOI: 10.1142/S0218202523500227.

[24] M. Conte and C. Surulescu. "Mathematical modeling of glioma invasion: acid-and vasculature mediated go-or-grow dichotomy and the influence of tissue anisotropy". In: *Applied Mathematics and Computation* 407 (2021), p. 126305. DOI: 10.1016/j.amc.2021.126305.

[25] G. Corbin, A. Klar, C. Surulescu, C. Engwer, M. Wenske, J. Nieto, and J. Soler. "Modeling glioma invasion with anisotropy-and hypoxia-triggered motility enhancement: From subcellular dynamics to macroscopic PDEs with multiple taxis". In: *Mathematical Models and Methods in Applied Sciences* 31.01 (2021), pp. 177–222. DOI: 10.1142/S0218202521500056.

[26] A. Dietrich, N. Kolbe, N. Sfakianakis, and C. Surulescu. "Multiscale modeling of glioma invasion: from receptor binding to flux-limited macroscopic PDEs". In: *Multiscale Modeling & Simulation* 20.2 (2022), pp. 685–713. DOI: 10.1137/21M1412104.

[27] G. Drosos and J. Pozo. "The causes and mechanisms of meniscal injuries in the sporting and non-sporting environment in an unselected population". In: *The Knee* 11.2 (2004), pp. 143–149. DOI: 10.1016/S0968-0160(03)00105-4.

[28] H. J. Eberl and L. Demaret. "A finite Difference Scheme for a degenerated diffusion equation arising in microbial ecology". In: *Electronic Journal of Differential Equations Conference* CS15 (2007), pp. 333–357.

[29] M. Eckardt, K. J. Painter, C. Surulescu, and A. Zhigun. "Nonlocal and local models for taxis in cell migration: a rigorous limit procedure". In: *Journal of Mathematical Biology* 81 (2020), pp. 1251–1298. DOI: 10.1007/s00285-020-01536-4.

[30] C. Edholm, B. Levy, A. Abebe, T. Marijani, S. Le Fevre, S. Lenhart, A.-A. Yakubu, and F. Nyabadza. "A Risk-Structured Mathematical Model of Buruli Ulcer Disease in Ghana". In: *Mathematics of Planet Earth: Protecting Our Planet, Learning from the Past, Safeguarding for the Future*. Cham: Springer International Publishing, 2019, pp. 109–128. DOI: 10.1007/978-3-030-22044-0_5.

[31] M. Englund and L. S. Lohmander. "Meniscectomy and osteoarthritis: what is the cause and what is the effect?" In: *International Journal of Clinical Rheumatology* 1.2 (2006), p. 207. DOI: 10.2217/17460816.1.2.207.

[32] C. Engwer, T. Hillen, M. Knappitsch, and C. Surulescu. "Glioma follow white matter tracts: a multiscale DTI-based model". In: *Journal of Mathematical Biology* 71 (2015), pp. 551–582. DOI: 10.1007/s00285-014-0822-7.

[33] C. Engwer, A. Hunt, and C. Surulescu. "Effective equations for anisotropic glioma spread with proliferation: a multiscale approach and comparisons with previous settings". In: *Mathematical medicine and biology: a journal of the IMA* 33.4 (2016), pp. 435–459. DOI: 10.1093/imammb/dqv030.

[34] S. Etuaful, B. Carbonnelle, J. Grosset, S. Lucas, C. Horsfield, R. Phillips, M. Evans, D. Ofori-Adjei, E. Klustse, J. Owusu-Boateng, G. Amedofu, P. Awuah, E. Ampadu, A. George, K. Asiedu, and M. Wansbrough-Jones. "Efficacy of the Combination Rifampin-Streptomycin in Preventing Growth of Mycobacterium ulcerans in Early Lesions of Buruli Ulcer in Humans". In: *Antimicrobial agents and chemotherapy* 49 (Jan. 2005), pp. 3182–6. DOI: 10.1128/AAC.49.8.3182-3186.2005.

[35] N. Fahy, M. Alini, and M. J. Stoddart. "Mechanical stimulation of mesenchymal stem cells: Implications for cartilage tissue engineering". In: *Journal of Orthopaedic Research* 36.1 (2018), pp. 52–63. DOI: 10.1002/jor.23670.

[36] U. Freymann, M. Endres, U. Goldmann, M. Sittinger, and C. Kaps. "Toward scaffold-based meniscus repair: effect of human serum, hyaluronic acid and TGF-ß3 on cell recruitment and re-differentiation". In: *Osteoarthritis and Cartilage* 21.5 (2013), pp. 773–781. DOI: 10.1016/j.joca.2013.02.655.

[37] L. Geris, A. Gerisch, J. Vander Sloten, R. Weiner, and H. Van Oosterwyck. "Angiogenesis in bone fracture healing: a bioregulatory model". In: *Journal of theoretical biology* 251.1 (2008), pp. 137–158. DOI: 10.1016/j.jtbi.2007.11.008.

[38] L. Ghasemi-Mobarakeh, M. P. Prabhakaran, L. Tian, E. Shamirzaei-Jeshvaghani, L. Dehghani, and S. Ramakrishna. "Structural properties of scaffolds: crucial parameters towards stem cells differentiation". In: *World journal of stem cells* 7.4 (2015), p. 728. DOI: 10.4252/wjsc.v7.i4.728.

[39] J. Giesselmann, N. Kolbe, Lukáčová-MedvidováMária, and N. Sfakianakis. "Existence and uniqueness of global classical solutions to a two dimensional two species cancer invasion haptotaxis model". In: *Discrete and Continuous Dynamical Systems - B* 23.10 (2018), pp. 4397–4431. DOI: 10.3934/dcdsb.2018169.

[40] M. Gómez-Benito, J. García-Aznar, J. Kuiper, and M. Dobláré. "Influence of fracture gap size on the pattern of long bone healing: a computational study". In: *Journal of Theoretical Biology* 235.1 (2005), pp. 105–119. DOI: 10.1016/j.jtbi.2004.12.023.

[41] E. Grosjean, A. Keilmann, H. Jäger, S. Mohanan, C. Redenbach, B. Simeon, C. Surulescu, L. de Roy, A. Seitz, G. Teixeira, M. Dauner, C. Linti, and G. Schmidt. *An in-silico approach to meniscus tissue regeneration: Modeling, numerical simulation, and experimental analysis*. 2024. DOI: 10.48550/arXiv.2403.05909.

[42] J. Guarner. "Buruli Ulcer: Review of a Neglected Skin Mycobacterial Disease". In: *Journal of Clinical Microbiology* 56.4 (2018). DOI: 10.1128/jcm.01507-17.

[43] W. Guo, S. Liu, Y. Zhu, C. Yu, S. Lu, M. Yuan, Y. Gao, J. Huang, Z. Yuan, J. Peng, A. Wang, Y. Wang, J. Chen, L. Zhang, X. Sui, W. Xu, and Q. Guo. "Advances and Prospects in Tissue-Engineered Meniscal Scaffolds for Meniscus Regeneration". In: *Stem Cells International* 2015 (2015), pp. 1–13. DOI: 10.1155/2015/517520.

[44] J. W. Hanneken and D. R. Franceschetti. "Exact Distribution Function for Discrete Time Correlated Random Walks in One Dimension". In: *Journal of Chemical Physics* 109.15 (1998), pp. 6533–6539. DOI: 10.1063/1.477304.

[45] N. A. Hill and D. P. Häder. "A Biased Random Walk Model for the Trajectories of Swimming Micro-organisms". In: *Journal of Theoretical Biology* 186 (1997), pp. 503–526. DOI: 10.1006/jtbi.1997.0421.

[46] T. Hillen and K. J. Painter. "A user's guide to PDE models for chemotaxis". In: *Journal of mathematical biology* 58.1 (2009), pp. 183–217.

[47] S. Hiremath and C. Surulescu. "A stochastic multiscale model for acid mediated cancer invasion". In: *Nonlinear Analysis: Real World Applications* 22 (2015), pp. 176–205. DOI: 10.1016/j.nonrwa.2014.08.008.

[48] R. Huiskes, W. V. Driel, P. J. Prendergast, K. Søballe, et al. "A biomechanical regulatory model for periprosthetic fibrous-tissue differentiation". In: *Journal of materials science: Materials in medicine* 8.12 (1997), pp. 785–788. DOI: 10.1023/a:1018520914512.

[49] P. A. Janmey and C. A. McCulloch. "Cell mechanics: integrating cell responses to mechanical stimuli". In: *Annu. Rev. Biomed. Eng.* 9 (2007), pp. 1–34. DOI: 10.1146/annurev.bioeng.9.060906.151927.

[50] P. D. R. Johnson, T. Stinear, P. L. C. Small, G. Pluschke, R. W. Merritt, F. Portaels, K. Huygen, J. A. Hayman, and K. Asiedu. "Buruli ulcer (M. ulcerans infection): new insights, new hope for disease control". In: *PLoS medicine* 2.4 (2005), e108. DOI: 10.1371/journal.pmed.0020108.

[51] J. Kelkel and C. Surulescu. "A multiscale approach to cell migration in tissue networks". In: *Mathematical Models and Methods in Applied Sciences* 22.03 (2012), p. 1150017. DOI: 10.1142/S0218202511500175.

[52] J. Kelkel and C. Surulescu. "On some models for cancer cell migration through tissue networks". In: *Mathematical Biosciences and Engineering* 8.2 (2011), pp. 575–589. DOI: 10.3934/mbe.2011.8.575.

[53] J. R. King, A. J. Koerber, J. M. Croft, J. P. Ward, P. Williams, and R. E. Sockett. "Modelling host tissue degradation by extracellular bacterial pathogens". In: *Mathematical Medicine and Biology: A Journal of the IMA* 20.3 (2003), pp. 227–260. DOI: 10.1093/imammb/20.3.227.

[54] N. Kolbe, N. Sfakianakis, C. Stinner, C. Surulescu, and J. Lenz. "Modeling multiple taxis: tumor invasion with phenotypic heterogeneity, haptotaxis, and unilateral interspecies repellence". In: *Discr. Cont. Dyn. Syst. B* 26 (2021), pp. 443–481. DOI: 10.3934/dcdsb.2020284.

[55] P. Kumar, J. Li, and C. Surulescu. "Multiscale modeling of glioma pseudopalisades: contributions from the tumor microenvironment". In: *Journal of Mathematical Biology* 82 (2021), pp. 1–45. DOI: 10.1007/s00285-021-01599-x.

[56] P. Kumar and C. Surulescu. "A Flux-Limited Model for Glioma Patterning with Hypoxia-Induced Angiogenesis". In: *Symmetry* 12.11 (2020). DOI: 10.3390/sym12111870.

[57] O. A. Ladyzenskaja, V. A. Solonnikov, and N. N. Ural'ceva. *Linear and Quasi-linear Equations of Parabolic Type*. Vol. 23. Providence, RI: American Mathematical Society Translations, 1968.

[58] C Lee, S Grad, M Wimmer, M Alini, et al. "The influence of mechanical stimuli on articular cartilage tissue engineering". In: *Topics in tissue engineering* 2.2 (2006).

[59] J. Lenz. "Global Existence for a Tumor Invasion Model with Repellent Taxis and Therapy". en. MA thesis. Darmstadt: Technische Universität Darmstadt, 2020. DOI: 10.25534/TUPRINTS-00011578.

[60] N. A. Licata, B. Mohari, C. Fuqua, and S. Setayeshgar. "Diffusion of Bacterial Cells in Porous Media". In: *Biophysical Journal* 110.1 (2016), pp. 247–257. DOI: 10.1016/j.bpj.2015.09.035.

[61] P. Liu, J. Shi, and Z.-A. Wang. "Pattern formation of the attraction-repulsion Keller-Segel system". In: *Discrete & Continuous Dynamical Systems-B* 18.10 (2013), pp. 2597–2625. DOI: 10.3934/dcdsb.2013.18.2597.

[62] G. Marino and P. Winkert. "Moser iteration applied to elliptic equations with critical growth on the boundary". In: *Nonlinear Analysis* 180 (2019), pp. 154–169. DOI: 10.1016/j.na.2018.10.002.

[63] R. L. Mauck, G. J. Martinez-Diaz, X. Yuan, and R. S. Tuan. "Regional multilineage differentiation potential of meniscal fibrochondrocytes: implications for meniscus repair". In: *The Anatomical Record* 290.1 (2007), pp. 48–58. DOI: 10.1002/ar.20419.

[64] H. McGann, P. Stragier, F. Portaels, D. Gascoyne Binzi, T. Collyns, S. Lucas, and D. Mawer. "Buruli ulcer in United Kingdom tourist returning from Latin America". In: *Emerging Infectious Diseases* 15.11 (2009), pp. 1827–1829. DOI: 10.3201/eid1511.090460.

[65] G. Meral and C. Surulescu. "Mathematical modelling, analysis and numerical simulations for the influence of heat shock proteins on tumour invasion". In: *Journal of Mathematical Analysis and Applications* 408 (Dec. 2013), pp. 597–614. DOI: 10.1016/j.jmaa.2013.06.017.

[66] Y. Mishima and M. Lotz. "Chemotaxis of human articular chondrocytes and mesenchymal stem cells". In: *Journal of Orthopaedic Research* 26.10 (2008), pp. 1407–1412. DOI: 10.1002/jor.20668.

[67] P. Mishra and D. Wrzosek. "Indirect taxis drives spatio-temporal patterns in an extended Schoener's intraguild predator–prey model". In: *Applied Mathematics Letters* 125 (2022), p. 107745. DOI: 10.1016/j.aml.2021.107745.

[68] P. Mishra and D. Wrzosek. "Repulsive chemotaxis and predator evasion in predator–prey models with diffusion and prey-taxis". In: *Mathematical Models and Methods in Applied Sciences* 32.01 (2022), pp. 1–42. DOI: 10.1142/S0218202522500014.

[69] A. A. Momoh, H. M. Abdullahi, N. G. Abimbola, and A. I. Michael. "Modeling, optimal control of intervention strategies and cost effectiveness analysis for buruli ulcer model". In: *Alexandria Engineering Journal* 60.2 (2021), pp. 2245–2264. DOI: 10.1016/j.aej.2020.12.042.

[70] S. J. Mousavi and M. Hamdy Doweidar. "Role of mechanical cues in cell differentiation and proliferation: a 3D numerical model". In: *PloS one* 10.5 (2015), e0124529. DOI: 10.1371/journal.pone.0124529.

[71] K. Muelder and A. Nourou. "Buruli ulcer in Benin". In: *Lancet* 336 (1990), pp. 1109–1111. DOI: 10.1016/0140-6736(90)92581-2.

[72] F. Nyabadza and E. Bonyah. "On the transmission dynamics of Buruli ulcer in Ghana: Insights through a mathematical model". In: *BMC Research Notes* 8 (2015). DOI: 10.1186/s13104-015-1619-5.

[73] M. S Oliveira and et al. "Infection with Mycobacterium ulcerans induces persistent inflammatory responses in mice". In: *Infection and Immunity* 73.10 (2005), pp. 6299–6310. DOI: 10.1128/IAI.73.10.6299-6310.2005.

[74] G. Orlando, K. J. Wood, P. De Coppi, P. M. Baptista, K. W. Binder, K. N. Bitar, C. Breuer, L. Burnett, G. Christ, A. Farney, M. Figliuzzi, J. H. Holmes, K. Koch, P. Macchiarini, S.-H. M. Sani, E. Opara, A. Remuzzi, J. Rogers, J. M. Saul, D. Seliktar, K. Shapira-Schweitzer, T. Smith, D. Solomon, M. Van Dyke, J. J. Yoo, Y. Zhang, A. Atala, R. J. Stratta, and S. Soker. "Regenerative Medicine as Applied to General Surgery". In: *Annals of Surgery* 255.5 (2012), pp. 867–880. DOI: 10.1097/sla.0b013e318243a4db.

[75] H. G. Othmer and T. Hillen. "The Diffusion Limit of Transport Equations Derived from Velocity-Jump Processes". In: *SIAM Journal on Applied Mathematics* 61.3 (2000), pp. 751–775. DOI: 10.1137/S0036139999358167.

[76] H. G. Othmer and T. Hillen. "The diffusion limit of transport equations II: Chemotaxis equations". In: *SIAM Journal on Applied Mathematics* 62.4 (2002), pp. 1222–1250. DOI: 10.1137/S0036139900382772.

[77] K. Painter and T. Hillen. "Mathematical modelling of glioma growth: The use of Diffusion Tensor Imaging (DTI) data to predict the anisotropic pathways of cancer invasion". In: *Journal of Theoretical Biology* 323 (2013), pp. 25–39. DOI: 10.1016/j.jtbi.2013.01.014.

[78] K. Painter and T. Hillen. "Volume-filling and quorum-sensing in models for chemosensitive movement". In: *Can. Appl. Math. Q.* 10 (Jan. 2002), pp. 501–543.

[79] J. Palomino, A. Obiang, L Realini, W. Meyers, and F Portaels. "Effect of oxygen on growth of Mycobacterium ulcerans in the BACTEC system". In: *Journal of clinical microbiology* 36.11 (1998), pp. 3420–3422. DOI: 10.1128/jcm.36.11.3420-3422.1998.

[80] J.-H. Park, T. Ushida, and T. Akimoto. "Control of cell differentiation by mechanical stress". In: *The journal of physical fitness and sports medicine* 2.1 (2013), pp. 49–62. DOI: 10.7600/jpfsm.2.49.

[81] C. A. Petty and J. H. Lubowitz. "Does arthroscopic partial meniscectomy result in knee osteoarthritis? A systematic review with a minimum of 8 years' follow-up". In: *Arthroscopy: The Journal of Arthroscopic & Related Surgery* 27.3 (2011), pp. 419–424. DOI: 10.1016/j.arthro.2010.08.016.

[82] M. M. Pillai, J. Gopinathan, R. Selvakumar, and A. Bhattacharyya. "Human Knee Meniscus Regeneration Strategies: a Review on Recent Advances". In: *Current Osteoporosis Reports* 16.3 (2018), pp. 224–235. DOI: 10.1007/s11914-018-0436-x.

[83] R. G. Plaza. "Derivation of a bacterial nutrient-taxis system with doubly degenerate cross-diffusion as the parabolic limit of a velocity-jump process". In: *Journal of Mathematical Biology* 78.6 (2019), pp. 1681–1711. DOI: 10.1007/s00285-018-1323-x.

[84] F. Portaels, W. M. Meyers, A. Ablordey, A. G. Castro, K. Chemlal, P. de Rijk, P. Elsen, K. Fissette, A. G. Fraga, R. Lee, et al. "First cultivation and characterization of Mycobacterium ulcerans from the environment". In: *PLoS neglected tropical diseases* 2.3 (2008), e178. DOI: 10.1371/journal.pntd.0000178.

[85] P. Prendergast, R. Huiskes, and K. Søballe. "Biophysical stimuli on cells during tissue differentiation at implant interfaces". In: *Journal of Biomechanics* 30.6 (1997), pp. 539–548. DOI: 10.1016/s0021-9290(96)00140-6.

[86] M. H. Protter and H. F. Weinberger. *Maximum principles in differential equations*. Springer Science & Business Media, 2012. DOI: 10.1007/978-1-4612-5282-5.

[87] F. O. Ribeiro, M. J. Gómez-Benito, J. Folgado, P. R. Fernandes, and J. M. García-Aznar. "In silico mechano-chemical model of bone healing for the regeneration of critical defects: the effect of BMP-2". In: *PloS one* 10.6 (2015), e0127722. DOI: 10.1371/journal.pone.0127722.

[88] P. A. Roberts, R. M. Huebinger, E. Keen, A.-M. Krachler, and S. Jabbari. "Mathematical model predicts anti-adhesion-antibiotic-debridement combination therapies can clear an antibiotic resistant infection". In: *PLoS Comput Biol* 15.7 (2019), e1007211. DOI: 10.1371/journal.pcbi.1007211.

[89] M. D. Rolfe, C. J. Rice, S. Lucchini, C. Pin, A. Thompson, A. D. S. Cameron, M. Alston, M. F. Stringer, R. P. Betts, J. Baranyi, M. W. Peck, and J. C. D. Hinton. "Lag Phase Is a Distinct Growth Phase That Prepares Bacteria for Exponential Growth and Involves Transient Metal Accumulation". In: *Journal of Bacteriology* 194.3 (2012), pp. 686–701. DOI: 10.1128/jb.06112-11.

[90] Z. Shi, C.-H. J. Wu, D. Ben-Arieh, and S. Q. Simpson. "Mathematical Model of Innate and Adaptive Immunity of Sepsis: A Modeling and Simulation Study of Infectious Disease". In: *Computational and Mathematical Methods in Medicine* 2016 (2016), pp. 1–10. DOI: 10.1155/2015/504259.

[91] A. Stevens and H. G. Othmer. "Aggregation, Blowup, and Collapse: The ABC's of Taxis in Reinforced Random Walks". In: *SIAM Journal on Applied Mathematics* 57.4 (1997), pp. 1044–1081. DOI: 10.1137/S0036139995288976.

[92] C. Stinner, C. Surulescu, and G. Meral. "A multiscale model for pH-tactic invasion with time-varying carrying capacities". In: *IMA Journal of Applied Mathematics* 80.5 (Nov. 2014), pp. 1300–1321. DOI: 10.1093/imamat/hxu055.

[93] C. Stinner, C. Surulescu, and A. Uatay. "Global existence for a go-or-grow multiscale model for tumor invasion with therapy". In: *Mathematical Models and Methods in Applied Sciences* 26.11 (2016), pp. 2163–2201. DOI: 10.1142/S021820251640011X.

[94] C. Stinner, C. Surulescu, and M. Winkler. "Global Weak Solutions in a PDE-ODE System Modeling Multiscale Cancer Cell Invasion". In: *SIAM Journal on Mathematical Analysis* 46.3 (2014), pp. 1969–2007. DOI: 10.1137/13094058X.

[95] Y. Tao and M. Winkler. "A Chemotaxis-Haptotaxis Model: The Roles of Nonlinear Diffusion and Logistic Source". In: *SIAM Journal on Mathematical Analysis* 43.2 (2011), pp. 685–704. DOI: 10.1137/100802943.

[96] C. C. Ude, S. B. Sulaiman, N. Min-Hwei, C. Hui-Cheng, J. Ahmad, N. M. Yahaya, A. B. Saim, and R. B. Idrus. "Cartilage Regeneration by Chondrogenic Induced Adult Stem Cells in Osteoarthritic Sheep Model". In: *PLoS One* 9.6 (2014), e98770. DOI: 10.1371/journal.pone.0098770.

[97] D. S. Walsh, F. Portaels, and W. M. Meyers. "Buruli ulcer (Mycobacterium ulcerans infection)". In: *Transactions of The Royal Society of Tropical Medicine and Hygiene* 102.10 (2008), pp. 969–978. DOI: 10.1016/j.trstmh.2008.06.006.

[98] Q. Wang, J. Yang, and L. Zhang. "Time-periodic and stable patterns of a two-competing-species Keller-Segel chemotaxis model: Effect of cellular growth". In: *Discrete and Continuous Dynamical Systems - B* 22.9 (2017), pp. 3547–3574. DOI: 10.3934/dcdsb.2017179.

[99] M. Wansbrough-Jones and R. Phillips. "Buruli ulcer: emerging from obscurity". In: *The Lancet* 367.9525 (2006), pp. 1849–1858. DOI: 10.1016/S0140-6736(06)68807-7.

[100] S. L. Waters, L. J. Schumacher, and A. J. El Haj. "Regenerative medicine meets mathematical modelling: developing symbiotic relationships". In: *npj Regenerative Medicine* 6.1 (2021). DOI: 10.1038/s41536-021-00134-2.

[101] M. Winkler. "Aggregation vs. global diffusive behavior in the higher-dimensional Keller–Segel model". In: *Journal of Differential Equations* 248.12 (2010), pp. 2889–2905. DOI: 10.1016/j.jde.2010.02.008.

[102] World Health Organization. *Provisional guidance on the role of specific antibiotics in the management of Mycobacterium ulcerans disease (Buruli ulcer)*. http://www.who.int/gtb-buruli/publications/PDF/ProvisionalguidanceWeb.pdf. Geneva: World Health Organization. 2004.

[103] H. Yu, A. B. Adesida, and N. M. Jomha. "Meniscus repair using mesenchymal stem cells – a comprehensive review". In: *Stem Cell Research & Therapy* 6.1 (2015). DOI: 10.1186/s13287-015-0077-2.

[104] J.-Q. Zhao, E. Bonyah, B. Yan, M. A. Khan, K. Okosun, M. Y. Alshahrani, and T. Muhammad. "A mathematical model for the coinfection of buruli ulcer and cholera". In: *Results in Physics* 29 (2021), p. 104746. DOI: 10.1016/j.rinp.2021.104746.

[105] A. Zhigun and C. Surulescu. "A Novel Derivation of Rigorous Macroscopic Limits from a Micro-Meso Description of Signal-Triggered Cell Migration in Fibrous Environments". In: *SIAM Journal on Applied Mathematics* 82.1 (2022), pp. 142–167. DOI: 10.1137/20M1365442.

[106] A. Zhigun, C. Surulescu, and A. Hunt. "A strongly degenerate diffusion-haptotaxis model of tumour invasion under the go-or-grow dichotomy hypothesis". In: *Mathematical Methods in the Applied Sciences* 41.6 (2018), pp. 2403–2428. DOI: 10.1002/mma.4749.

[107] A. Zhigun, C. Surulescu, and A. Uatay. "Global existence for a degenerate haptotaxis model of cancer invasion". In: *Zeitschrift für angewandte Mathematik und Physik* 67 (2016), pp. 1–29. DOI: 10.1007/s00033-016-0741-0.

[108] H. Zreiqat, C. R. Dunstan, and V. e. Rosen. *A Tissue Regeneration Approach to Bone and Cartilage Repair*. Springer International Publishing, 2015. DOI: 10.1007/978-3-319-13266-2.

## Academic curriculum vitae

| | |
|---|---|
| *October 2019 - February 2025* | ***Ph.D. Mathematics***<br>*RPTU Kaiserslautern - Landau*<br>*Kaiserslautern, Germany* |
| *October 2018 - September 2019* | ***Master's Student***<br>*Technical University of Kaiserslautern*<br>*Kaiserslautern, Germany* |
| *May 2018 - September 2018* | ***Contact Student***<br>*Technical University of Kaiserslautern*<br>*Kaiserslautern, Germany* |
| *July 2013 - April 2015* | ***Master of Science, Mathematics***<br>*Cochin University of Science & Technology*<br>*Kerala, India* |
| *June 2010 - May 2013* | ***Bachelor of Science, Mathematics***<br>*Sacred Heart College, MG University*<br>*Ernakulam, Kerala, India* |

# Akademischer Lebenslauf

| | |
|---|---|
| *Oktober 2019 - Februar 2025* | ***Promotion in Mathematik***<br>*RPTU Kaiserslautern - Landau*<br>*Kaiserslautern, Deutschland* |
| *Oktober 2018 - September 2019* | ***Masterstudentin***<br>*Technische Universität Kaiserslautern*<br>*Kaiserslautern, Germany* |
| *Mai 2018 - September 2018* | ***Kontactstudentin***<br>*Technische Universität Kaiserslautern*<br>*Kaiserslautern, Germany* |
| *Juli 2013 - April 2015* | ***Master of Science, Mathematik***<br>*Cochin University of Science & Technology*<br>*Kerala, Indien* |
| *Juni 2010 - Mai 2013* | ***Bachelor of Science, Mathematik***<br>*Sacred Heart College, MG University*<br>*Ernakulam, Kerala, Indien* |